Remote Sensing of Environment 334 (2026) 115158

Contents lists available at ScienceDirect

Remote Sensing of Environment

journal homepage: www.elsevier.com/locate/rse

Review

A review of forward modelling and retrieval approaches for forest soil moisture and vegetation optical depth using L-band radiometry

Andreas Colliander [a,i,*], Mike Schwank [b,c], Yiwen Zhou [b], Mehmet Kurum [d], Cristina Vittucci [e], Leung Tsang [f], Alex Roy [g], Aaron Berg [h]

[a] Jet Propulsion Laboratory, California Institute of Technology, Pasadena, CA, USA
[b] Swiss Federal Institute for Forest, Snow and Landscape Research WSL, Birmensdorf, Switzerland
[c] GAMMA Remote Sensing Research and Consulting AG, Gümligen, Switzerland
[d] University of Georgia, Athens, GA, USA
[e] University of Rome Tor Vergata, Rome, Italy
[f] University of Michigan, Ann Arbor, MI, USA
[g] Université du Québec à Trois-Rivières, Québec, Canada
[h] University of Guelph, Guelph, ON, Canada
[i] Finnish Meteorological Institute, Helsinki, Finland

ARTICLE INFO

Editor: Jing M. Chen

Keywords:
Soil moisture
Vegetation optical depth
Microwave radiometry
L-band
Forests

ABSTRACT

Forests are a critical component of the Earth system, accounting for approximately one-third of global photosynthetic activity and carbon storage. They also provide essential habitats for countless species and vital resources for human activities. Low-frequency (L-band; 1–2 GHz) microwave radiometry enables the measurement of forest soil moisture (SM) and L-band vegetation optical depth (L-VOD), offering valuable insights into processes such as tree growth, water infiltration, soil fertility, fuel moisture, carbon stocks, wildfire vulnerability, and biodiversity dynamics. These measurements also support the study of carbon and water fluxes, tree responses to hydrological stress (e.g., drought), and fuel moisture estimation. However, existing algorithms for retrieving SM and L-VOD were primarily developed for low-biomass vegetation types (e.g., grasslands and croplands), differing structurally from forests. This motivates the present review to evaluate the current retrieval approaches, their performance assessment methods, and available validation resources. The review found that systematic uncertainties persist in forest retrievals, despite the demonstrated sensitivity of L-band brightness temperature (TB) to forest SM and L-VOD. Moreover, the focus on non-forest ecosystems has led to a lack of suitable ground truth and reference data for validating forest SM and L-VOD products, and current validation techniques remain underdeveloped. To fully harness the potential of L-band radiometry in forest monitoring, new retrieval algorithms that account for the unique structural and compositional characteristics of forests are required. Additionally, validation efforts must be enhanced both quantitatively and qualitatively—particularly for L-VOD—to improve confidence in these remote sensing products.

1. Introduction

1.1. Background and motivation

Forests cover over 30 % of the land surface and constitute a vital component of the Earth system. They account for ~30 % of the total global photosynthetic activity, store ~30 % of the total carbon, and provide a habitat for countless species. At the same time, they offer critical resources to anthropogenic activities, such as timber, firewood, fiber, and food (e.g., Bonan, 2008; Lutz et al., 2018; Powell et al., 2020; FAO, 2020). However, monitoring the growth and disturbance processes of forests is challenging because instrumenting forests is logistically tricky or even prohibitive (e.g., Robinson et al., 2008). Remote sensing offers an invaluable tool for effectively providing information on large and remote areas.

Soil moisture (SM) [m^3/m^3], above-ground biomass (AGB) [kg/ha], and vegetation water column (VWC) [kg/m^2] (see Table 1) of trees are some of the most critical parameters describing forests and their various

* Corresponding author.
E-mail address: andreas.colliander@fmi.fi (A. Colliander).

https://doi.org/10.1016/j.rse.2025.115158
Received 25 July 2025; Received in revised form 12 November 2025; Accepted 22 November 2025
Available online 15 December 2025

Table 1
Variables used in this paper.

Variable	Unit	Comment
α	–	Absorption coefficient
AGB	kg/ha	Above-ground biomass
b	1/(kg/m^2)	A coefficient relating VWC to VOD
C	–	Parameter determining the weight between $T_{G,surf}$ and $T_{G,deep}$ for the computation of T_{eff}
ε_G	–	Ground permittivity
$e_{sp}^{(N)}$	–	Nth-order RT solution of p-polarised emission
$E^{ex,q}$	V/m	Exciting electric field of the q^{th} tree, after multiple scattering as governed by Foldy-Lax equations
E^{inc}	V/m	Incident electric field on the forest
ϕ	deg	Azimuth angle
f	Hz	Frequency
F	–	Scattering amplitude
G	–	Green's function
HR	–	Roughness parameter
I		Intensity
κ_e		Attenuation rate in forest due to summation of scattering and absorption (extinction)
λ	m	Wavelength
l	m	Length
LAI	–	Leaf Area Index
lc	m	Correlation length
MD		Mean difference
$n_{[H/V]}$, NRV, NRH	–	Exponential parameter for the incidence angle dependency of the HQN roughness correction
ω_{eff}	–	Effective scattering albedo
$\Omega_p^{(n)}$		n^{th}-order multiple-scattering contribution to the zero-order solution
P		Phase matrix of bistatic scattering of intensities
θ	deg	Incidence angle (off-nadir)
Q	–	Polarisation mixing parameter for the HQN roughness correction
ρ_{soil}	g/cm^3	Soil bulk density
r	m	Radius
R	–	Pearson correlation
RMSD		Root-mean-square difference
σ	m	Root-mean-square height variation
SM	m^3/m^3	Volumetric soil moisture
τ_{eff}	–	Vegetation optical depth
T		T-matrix of bistatic scattering of complex electric field
TB	K	Brightness temperature
T_{eff}	K	Effective ground temperature
$T_{G,[surf/deep]}$	K	Ground temperature: surface or deep layer
ubRMSD		Unbiased root-mean-square difference
VOD	–	Vegetation optical depth
VWC	kg/m^2	Vegetation water column
VWD	m^3/m^3	Vegetation water density

interactions with the atmosphere and the ground. SM has a vital role in controlling processes such as the growth of trees, water infiltration into the ground, soil fertility evolution, and fuel moisture (e.g., Robinson et al., 2008; Oren et al., 1999; Rakhmatulina et al., 2021). Monitoring AGB serves, for example, quantifying carbon stock and wood fuel, assessing wildfire vulnerability, and tracking the evolution of biodiversity (e.g., Malhi and Phillips, 2004; FAO, 2020; Bunker et al., 2005). VWC of forests is needed for understanding carbon and water fluxes, observing trees' response to the soil's and atmosphere's hydrologic state (e.g., droughts and vapor pressure deficit (VPD)), and estimating fuel moisture for wildfire management (Bohrer et al., 2005; Anderegg et al., 2018; Nelson, 2001). SM and AGB are identified as Essential Climate Variables (ECVs) by the World Meteorological Organization (WMO) because of their vital roles in improving the monitoring and understanding of the climate system (WMO, 2022; Zhou et al., 2025).

Detecting SM in forested environments requires a detectable signal from the soil to penetrate the vegetation canopy, such as brightness temperature (TB) in the case of microwave radiometry (e.g., Ulaby and Long, 2014). Low-frequency microwave radiation features this property while being sensitive to ground permittivity and L-band Vegetation Optical Depth (L-VOD) (e.g., Njoku and Entekhabi, 1996), which is defined as the attenuation of electromagnetic (EM) waves propagating through vegetation canopies at L-band. The former can be translated into SM and the latter into, e.g., AGB and VWC when combined with the physical properties (e.g., effective temperatures, composition, and structure) of ground and vegetation (e.g., Ulaby et al., 1986; Wigneron et al., 2024). Using radiometry in the protected band (1.400–1.427 GHz) within the L-band (1–2 GHz) to retrieve SM dates back to the 1970s (Schmugge et al., 1974); VOD can be retrieved simultaneously with SM from the vertically and horizontally polarised TB (Njoku and Li, 1999; Yueh et al., 2008). Compared to higher microwave frequencies, the L-band exhibits superior SM retrieval performance as it has a larger sensing depth and is less susceptible to surface roughness and vegetation effects (e.g., Schmugge et al., 1986; Gao et al., 2022). The spaceborne L-band radiometers enabled the global measurements of forest SM and VOD. In 2009, ESA (European Space Agency) launched the SMOS (Soil Moisture Ocean Salinity) mission (Kerr et al., 2010); in 2011, NASA (National Aeronautics and Space Administration) launched the Aquarius mission (Le Vine et al., 2010), and in 2015, NASA launched the SMAP (Soil Moisture Active Passive) mission (Entekhabi et al., 2014).

This article aims to review the current state of L-band radiometry–based SM and L-VOD retrieval methodologies and their validation for forest environments. Given the high importance of these parameters and the potential benefits of further algorithm development, we were motivated to conduct this review. We focus on L-band radiometry because of its demonstrated capability to measure both SM and L-VOD in forests, with sensitivity to AGB and VWC. Although active L-band measurements (radar) have also shown promise for SM and AGB retrieval, this article is limited to passive radiometry to maintain a focused scope. Review papers exist on SM and VOD retrievals (e.g., Babaeian et al., 2019; Frappart et al., 2020; Li et al., 2021a; b; Wigneron et al., 2017, 2024), but apart from Wigneron et al. (2024), they do not focus on forests, and none of them address the unique challenges of forested regions in the context of improving the reliability and scientific impact of these parameters. Here, we aim to fill that gap and support the community in advancing scientifically robust SM, AGB, and VWC retrievals for forests.

The well-established, straightforward interactions between thermal L-band emission and short vegetation, e.g., grass and crops (e.g., Jackson and Schmugge, 1991; Jackson et al., 1995; Wigneron et al., 1995, 2007; Kerr et al., 2012; Chan et al., 2016), do not apply to forests. For example, Ferrazzoli and Guerriero (1996) proposed a microwave emission model (MEM) to consider multiple scattering effects in the vegetation, which are much more important for forests than for low vegetation. In addition, the microwave propagation through forests is complex, as they are neither homogeneous nor isotropic masses of vegetation but highly heterogeneous constructs of varying densities of stems, branches, and leaves. The attenuation of L-band waves when they pass through the forest canopy is influenced by multiple and variable scattering processes that depend on the density, orientation, and dimensions of the leaves, branches, and stems, together with the macro parameters such as the canopy heights and gaps (e.g., Jeong et al., 2023b; Zhou et al., 2024). Furthermore, TB measurements are spatial averages, with a footprint including a range of these conditions, so the eventual effective emission and penetration represent an aggregate of the different conditions. This means that the penetration of upwelling L-band emission from the forest ground does occur mostly through various less woody parts (leaves) and gaps in the canopy, rather than through the stems and branches. Thus, despite the potentially substantial water amounts in forest vegetation, several studies point to the fact that L-band satellite radiometry is sensitive to SM under forests along with L-VOD (e.g., Guglielmetti et al., 2008; Rahmoune et al., 2014; Colliander et al., 2020; Ayres et al., 2021). The gaps and the less-dense parts of the vegetation canopy undoubtedly play a role in this; therefore, this paper reviews EM modelling approaches that attempt to account for these

effects and the multiple scattering effects by stems and branches. The main categories are (i) MEMs that adapt the assumption of the statistical homogeneity within RT approaches (Section 3.2) and (ii) MEMs that explicitly model the EM interactions in the canopy based on the actual forest geometry (Section 3.3).

The relatively sparse occurrence of field experiments (see Section 4) targeting these questions culminated recently in field experiments executed at an unprecedented scale in the northeastern US and the southern boreal zone in Canada by the SMAP mission and its partners (Colliander et al., 2025; Berg et al., 2025). The L-band community needed this data to improve and validate the forest SM and L-VOD retrievals, which is also one of the focus areas of SMAP's extended mission. The experiments provide reference data to answer these questions for temperate and boreal zone forest types. While the retrieval of forest SM and L-VOD has received less attention, there were some focused studies already before the era of spaceborne low-frequency radiometry. For instance, Mätzler (1994) investigated and posed research questions that are very similar to what is currently still being asked when analysing the now available satellite data. These questions concern how to parameterise the vegetation in the SM retrieval, how to translate L-VOD into vegetation parameters, such as AGB and VWC, and how to develop MEM to represent thermal L-band radiation emitted by forested grounds realistically.

The main challenges in retrieving SM and L-VOD for forests are: i) significant spatial heterogeneity of SM and vegetation at the satellite footprint-scale, ii) parameterization of ground roughness (ground surface scattering and impedance matching), iii) effects of organic cover layers (litter, moss, lichen), iv) parameterization of vegetation volume scattering (scattering albedo), v) seasonality of tree phenology, vi) snow in canopy and on ground, vii) freezing and thawing of the soil and vegetation, and viii) the small-scale vegetation heterogeneities (e.g., variations in stem density, crown depth, branch orientations, gaps in the canopy). This paper aims to review the status of the research dedicated to forest SM and L-VOD, the retrieval algorithms, and the data products to support the continued development of forest SM and L-VOD retrievals.

1.2. Forest soil and vegetation parameters

1.2.1. Soil

SM [m^3/m^3], also known as soil volumetric water content in soil sciences, represents the volume of water within a given volume of soil. Its evolution is driven by wetting and drying processes, where precipitation or irrigation typically causes wetting, while infiltration, evaporation, and transpiration govern drying (e.g., Hillel, 1998).

SM influences soil permittivity, which in turn determines soil emissivity, enabling SM measurement using L-band radiometers (e.g., Schmugge et al., 1986). Due to wetting and drying dynamics, SM is distributed unevenly throughout the soil column (e.g., Hillel, 1998). L-band radiometer measurements are governed by the profiles of soil permittivity and temperature, with the received emission originating from the surface to a depth that varies according to the permittivity profile (e.g., Njoku et al., 1977). However, the near-surface SM dictates the emissivity because of the significant permittivity gradient at the air-ground interface, compared to variations within the soil column (e.g., Shellito et al., 2016; Colliander et al., 2017).

The permittivity of the soil-water-air mixture is influenced not only by water content but also by factors such as how water interacts with soil particles (e.g., free or bound water), soil texture (sand, silt, clay), organic matter content, soil structure (bulk density, porosity), and freezing status (e.g., Topp et al., 1980; Seyfried and Murdock, 2004; Mavrovic et al., 2021). Converting the permittivity retrieved from L-band radiometer measurements to SM requires accounting for these additional parameters, making it a complex process (e.g., Dobson et al., 1985; Hallikainen et al., 1985; Schwank and Mätzler, 2006; Mironov et al., 2009, 2019; Park et al., 2019). This paper will discuss these issues from the viewpoint of forest SM retrieval, needing to account for extremely complex textural and structural composition, organic matter variability, and temperature distribution.

1.2.2. Vegetation

AGB [kg/ha] refers to the total mass of living plant material (without water), including stems, leaves, and branches, found above the ground surface (CEOS, 2025). The vegetation interacts with microwaves through the permittivity of its components, determined by the plant tissue-water-air mixture (El-rayes and Ulaby, 1987; Ulaby and El-rayes, 1987). At L-band, the dry plant tissue has a relatively low permittivity compared to that of water, causing changes in the water content of the plants to have a notable impact on the propagation of L-band emission in forests (e.g., Ulaby and El-rayes, 1987).

The relationship between AGB and the L-band propagation parameters (attenuation and scattering) in the forest is complex because the size, distribution, and orientation of the canopy constituents (stems, branches, leaves/needles) affect the propagation partly independently from the AGB (e.g., Ferrazzoli and Guerriero, 1996). In general, forest AGB is slowly varying, apart from disturbances, which would lend itself well to a reliable AGB retrieval, given enough information about the structure is available. However, because the vegetation effect on L-band propagation also depends on the permittivity, which is dominated by the water content, L-VOD is a function of structure and water content, making retrieving these quantities challenging.

Often, dynamics in L-VOD retrieval is attributed to changes in VWC [kg/m^2], assuming a constant AGB (e.g., Konings et al., 2021). However, the propagation of the microwave signals does not only depend on the amount of water in the path, but how it is distributed (for example, in extreme cases, the same amount of water could be in a continuous slab of liquid water or droplets of water spread out in a large volume, with a very different result (e.g., Ulaby et al., 1986). Therefore, a quantity of vegetation water density (VWD) [m^3/m^3], for example, could be defined in relation to L-VOD. Both VWC and VWD account for the total volume occupied by the vegetation, while for many ecohydrological applications, it is their relationship to the water content of vegetation constituent pieces (stem, branches, leaves/needles) that is critical. This paper will discuss the reported L-VOD, AGB, and VWC retrievals, the challenges, and how to potentially overcome them with state-of-the-art vegetation emission modelling.

2. L-band emission of forest ground

To retrieve forest parameters from TB, a forward operator (incorporating a MEM as the central component) is needed to relate the measured TB to parameters such as SM and L-VOD. The essential components of a forest are: (i) the forest ground, defined as a layered system of soil, cover layer (litter, moss, etc.), and possibly snow (Fig. 1) and (ii) wooden tree components (branches and trunks) and leaves or needles, depending on the tree type (Section 3). The forest ground is defined as soil with a rough surface overlaid with an organic cover layer because the decomposing dead organic material (litter) gradually becomes the upper soil horizon, resulting in no clear boundary between the upper soil horizon and the organic cover layer that has not yet decomposed. At L-band, and especially when the cover layer is dry, TB upwelling from the forest ground is affected by the thermal emission of the soil below the cover. Soil emission is determined by its effective temperature and emissivity, when Local Thermal Equilibrium (LTE) is assumed (Sections 2.1 and 2.2). The influence of the cover layer on thermal L-band emission has been less investigated compared to an exposed soil. However, experimental evidence shows that moist leaf litter can dominate forest ground emission, and methods for modelling the TB of litter-covered soils have been proposed (Section 2.3).

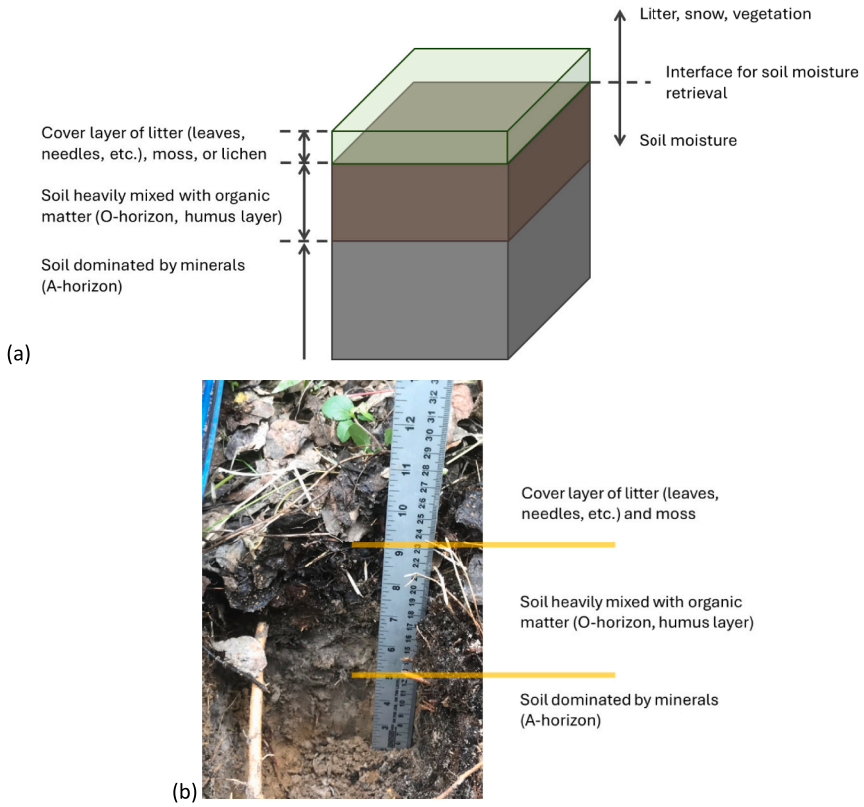

Fig. 1. (a) Schematic diagram of the vertical composition of a forest ground and its interpretation in SM retrieval. (b) Example photo of the vertical composition of a boreal forest ground.

2.1. *Effective ground temperature of forests*

The effective ground temperature T_{eff} is computed by integrating the ground temperature profile $T(z)$ over depth z considering the microwave absorption coefficient $\alpha(\varepsilon_{\mathrm{G}}(z))$ defined by the profile $\varepsilon_{\mathrm{G}}(z)$ of complex ground permittivity (Wilheit, 1978; Ulaby and Long, 2014). In practice, this integral (eq. 3 in Schneeberger et al., 2004) cannot be calculated because usually neither the temperature nor the absorption profile of the ground is known. As a way out, Choudhury et al. (1982) developed an empirical approach to estimate T_{eff} from a near-surface temperature ($T_{\mathrm{G,surf}}$) and a deep-ground temperature ($T_{\mathrm{G,deep}}$), which typically represent ground temperatures at depths 0 cm to 5 cm and 50 cm to 100 cm, respectively. An empirical parameter C determines how close T_{eff} is to either $T_{\mathrm{G,surf}}$ or $T_{\mathrm{G,deep}}$, depending on the integrated losses and emission above the deep ground layer. Accordingly, C is a function of frequency f and the depth profile of ε_{G}, because α depends on f and ε_{G}. To take into account the sensitivity of C on ε_{G}, Wigneron et al. (2001) proposed an L-band specific parametrization by expressing C as a function of surface SM, making C lower for dryer ground and resulting in T_{eff} closer to $T_{\mathrm{G,deep}}$ and vice versa. Holmes et al. (2006) proposed the parameterization according to the complex permittivity of the ground surface. Because the absorption coefficient α is in proportion to the relation of the imaginary and real part of the ground permittivity (Chanzy et al., 1997), this parameterization has a better physical base and is shown to be more robust compared to the parameterization proposed by Wigneron et al. (2001). Lv et al. (2014, 2016) presented two-layer and multi-layer models using the ground complex permittivity to compute the scaling coefficients without fitting parameters.

However, none of the approaches mentioned for estimating T_{eff} have been specifically calibrated for forest ground covered by litter or moss, meaning that simulated forest T_{eff} are subject to additional uncertainties. In general, the assumption is that the T_{eff} impact on the modelled TB is small because of its small relative uncertainty (in units of Kelvin), which is crucial for successful retrievals over the globe. Most L-band retrieval algorithms use land surface models as the source of ground temperatures in absence of simultaneous optical or higher microwave frequency measurements available with SMAP and SMOS (e.g., Chaubell et al., 2022; Kerr et al., 2016). The modelling of the ground temperature in the forests is particularly challenging because of the difficulty modelling the thermal effect of forest canopy on the forest ground (e.g., Paul et al., 2004).

2.2. *Ground emissivity of forests*

Traditionally, ground emissivity is simulated in three steps: i) the ground effective permittivity is calculated using dielectric mixing models; ii) specular surface reflectivity is computed from the effective permittivity with the Fresnel equations; iii) specular reflectivity is adjusted to represent the more realistic non-specular (partially diffuse-scattering) reflectivity of the air-to-surface interface, commonly referred to as a rough surface (e.g., Njoku and Entekhabi, 1996; Schwank and Mätzler, 2006). The radiometer measurements are affected by the rough surface reflectivity, after the temperature compensation, and forward operators with various parameters and inputs are needed to retrieve SM.

2.2.1. *Dielectric mixing models*

A straightforward empirical approach to express the real part of the complex soil permittivity by means of volumetric soil moisture (SM) was developed by Topp et al. (1980). The advantage of this purely empirical model is that it does not need any information on soil texture and temperature. It performs well for coarse-textured soils with a maximum specific matrix surface of $<100\ \mathrm{m^2 g^{-1}}$ and bulk densities in the range of $1.35\ \mathrm{g/cm^3} \lesssim \rho_{\mathrm{soil}} \lesssim 1.50\ \mathrm{g/cm^3}$. However, soils are complex porous multi-phase media consisting of several dielectric phases such as air, free- and bound water, mineral and organic components of different dimensions,

and possibly ice. A large number of physics-based dielectric mixing models (Sihvola, 1999) are available and used in microwave remote sensing (e.g., Chapter 4 in Mätzler, 2006; Wang and Schmugge, 1980; Dobson et al., 1985; Mironov et al., 2004) to relate soil permittivity to SM, whereas the more complex the model, the more soil parameters are needed.

In the context of L-band radiometry applied to forested areas, it is essential to recognise that forest ground typically has high amounts of organic matter due to slowly decomposing litter, consisting of plant debris, moss, or lichen. Organic-rich soils have small bulk densities, high porosities, and large specific surface areas compared to mineral soils. This leads to extremely high water holding capacities of up to 0.8 to 0.9 m^3/m^3 compared to the typical 0.4 to 0.6 m^3/m^3 of mineral soils (Kellner and Lundin, 2001; Li et al., 2004), as well as to higher fractions of bound water (de Loor, 1983; Santamarina et al., 2001; Bircher et al., 2016).

Fig. 2 (a) shows an example of the permittivity as a function of SM for a ground dominated by mineral and organic matter, demonstrating the large range of the real part of the ground permittivity (RDC) for the same SM value. A mixing model specifically developed for organic-rich soils in thawed and freezing conditions was developed by Mironov et al. (2010). SMOS has been using Mironov et al. (2013) after a series of model improvements, simplifications regarding the parameterisation, and making it specific for L-band. The model attempts to strike a balance between requiring very few input parameters: SM, soil temperature, and clay content, rather than including a large number of difficult-to-measure and potentially erroneous input parameters, which is important for practical retrieval approaches.

2.2.2. Flat surface (specular) reflectivity

The reflectivity at the boundary between two dielectric media, which are homogeneous, isotropic, and non-scattering and whose interface is flat and smooth, can be computed from the media's complex permittivities using the Fresnel equation (Ulaby et al., 1982). Fig. 2 (b) shows the reflectivity as a function of VSM. The reflectivity is computed from the ground complex permittivity ($\varepsilon_G = \varepsilon'_G + i \cdot \varepsilon''_G$; note that the sign of the imaginary part is convention-based) based on Mironov models for mineral (Mironov et al., 2009) and organic (Mironov et al., 2019) soils using VSM and 40° off-nadir angle. The reflectivity is also computed using similar values but with $\varepsilon''_G = 0$. The plot shows that ε''_G has very little effect on reflectivity, meaning that ε'_G can be solved reliably from reflectivity by considering the imaginary part zero, simplifying the inversion considerably. However, as explained in Section 2.1, ε''_G is still relevant for determining the effective ground temperature (or in multilayer soil emission modelling).

As ε'_G can be retrieved from radiometer measurements, a dielectric mixing model (Section 2.2.1) can be applied separately. This is particularly beneficial for forested cases, for which the ground composition is complex and poorly known globally, and the dielectric mixing models for such grounds have substantial uncertainties, allowing the investigation and potential validation of ε'_G independently from applying the dielectric mixing model (e.g., Colliander et al., 2020, 2025; Mavrovic et al., 2021).

2.2.3. Air-surface interface correction

The forest ground surface is not flat and smooth, and the ground is neither homogeneous nor isotropic; therefore, it cannot be treated as non-scattering, making it necessary to correct the Fresnel specular reflectivity to account for these factors, which are further compounded by the varying effect of different spatial scales of the surface roughness (e.g., Neelam et al., 2020; Schwank et al., 2010a). Optical or mechanical assessments of the surface roughness (e.g., needle boards or a laser profilometers, see de Rosnay et al. (2006)) cannot directly translate to microwave reflection due to L-band's emission depth (a few cm in moist soils, tens of cm in dry soils; Jackson et al., 1996) and its inability to distinguish topographic features from dielectric heterogeneities (Schwank and Mätzler, 2006). Semi-empirical correction of specular surface reflectivity (e.g., Shi et al., 2002; Schwank et al. 2010a), or even EM modelling (e.g., Fung, 1994; Chen et al., 2003) is needed to simulate microwave rough ground reflectivity.

Fung (1994) and Tsang et al. (1994; 2000; 2001) provide exhaustive reviews of surface emission and scattering models, but these require extensive computational effort and detailed ground data (e.g., correlation length and autocorrelation function type), hampering their practical use in traditional retrieval algorithms. Shi's fast-model (Shi et al., 2002), derived from the Integral Equation Model (IEM) (Fung, 1994), computes L-band reflectivities at horizontal and vertical polarisation across incidence angles, root mean square (rms) height variations (σ), correlation lengths (lc), and permittivities. However, quantifying σ and lc globally at the spatial scales of spaceborne L-band radiometers remains a significant challenge.

The HQN model, developed by Wang and Choudhury (1981), is a semi-empirical ground roughness model widely used in SMOS and SMAP SM and L-VOD retrieval algorithms to simulate rough ground

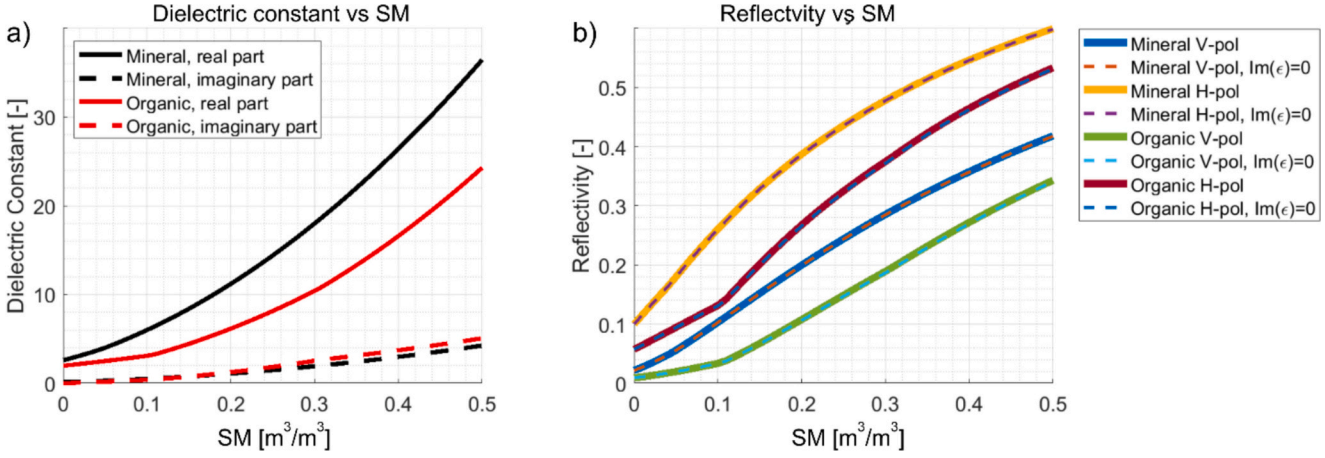

Fig. 2. (a) Soil permittivity, computed using the Mironov soil dielectric models for mineral (Mironov et al., 2009) and organic (Mironov et al., 2019) soils (35 % organic content), as a function of volumetric soil moisture (SM). (b) Reflectivity as a function of SM. The reflectivity is computed using the Fresnel equation in two cases for the mineral and organic cases: 1) the complex permittivity with the actual computed imaginary part, and 2) the complex permittivity with the imaginary part set to zero, as a function of VSM.

reflectivities. While the four parameters (*HR*, *Q*, n_H, n_V) are interdependent, their main impacts are distinct: *HR* reduces Fresnel reflectivity equally for horizontal (H) and vertical (V) polarisation by accounting for small-scale surface undulations (Wigneron et al., 2011), *Q* decreases polarisation differences by increasing polarisation mixing, and n_H and n_V reflect the incidence angle-dependent effects of roughness. HQN parameters have not been validated globally and they are not likely to exist; parameters for operational data products are therefore determined empirically to align retrieved SM with corresponding in situ measurements. Consequently, developing new data products (e.g., forest SM, L-VOD, or snow properties) requires reviewing roughness parameterisation.

Ground surface roughness can also be viewed as "small-scale" dielectric heterogeneities, or "dielectric roughness" (Wigneron et al., 2017). The Air-to-Soil (A2S) transition model (Schneeberger et al., 2004; Mätzler, 2006; Schwank et al. 2010a) describes the soil-air boundary as a gradual transition zone influenced by surface undulations (Fig. 3(a)). Apart from the "small-scale" topography, this zone can also account for a range of non-scattering dielectric heterogeneities, such as moisture variations (e.g., local ponding), soil structure (e.g., stones), and overlaying materials (e.g., litter, sparse vegetation, or light snow). The dielectric transition (Fig. 3 (d)) is represented by a dielectric mixing model that considers the increasing volume fraction (Fig. 3 (c)) of bulk soil with depth. Rough ground reflectivities are calculated using a coherent radiative transfer model (Bass et al., 1995). A fast-model detailed in Chapter 4.7.5 of Mätzler (2006) computes rough-soil reflectivity relative to the specular Fresnel reflectivity, with relative roughness defined by the ratio between standard deviation of surface height and observation wavelength. This fast model is adaptable for different wavelengths by considering the Bragg limit for small-scale undulations. Its form is similar to the HQN model and other semi-empirical roughness models (e.g., Wegmüller and Mätzler, 1999; Mo and Schmugge, 1987).

The forest ground surface layer is typically mixed with significant amounts of organic matter (O-horizon), compounding the problem of defining the surface roughness, including the dielectric roughness, because of organic matter's low bulk density and its variability (e.g., Colliander et al., 2025; Berg et al., 2025). This amplifies the problem of transforming the Fresnel reflectivity of an idealised specular surface to the actual reflectivity with ad hoc parameters. At the same time, high-fidelity EM modelling is difficult because of the complexity of parameterising the volume with physically based descriptors, and finding those descriptors globally for retrieval algorithms is challenging.

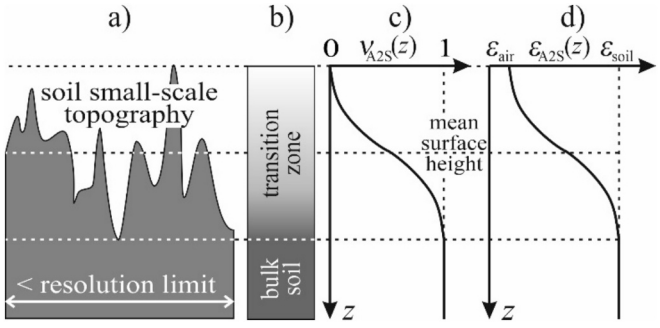

Fig. 3. *Sketch of the concept used in the Air-to-Soil (A2S) transition model to represent impacts of surface roughness on ground reflectivity. a) The cross section of the soil "small-scale" topography of dimensions smaller than the resolution limit; b) the postulated A2S transition zone; c) the profile of the volumetric soil fraction ($v_{A2S}(z)$) used in the simulation; d) the permittivity profile ($\varepsilon_{A2S}(z)$) finally used to compute reflectivities.*

2.3. Ground cover layer in forests

The forest ground is typically covered with decomposing leaves or needles deposited by the trees or a living layer of moss or lichen. The type and thickness of this cover layer vary based on multiple factors, including forest type, soil type, climatology, growth stage of the forest, etc. Over time, this cover layer contributes to the formation of the humus layer (e.g., Berg and McClaugherty, 2008) (Fig. 1). The effect of the cover layer on microwave emission has not been investigated extensively, but there are a few studies that have attempted to quantify this effect; in each case, the forest floor composition was different.

Schwank et al. (2008) used the Forest Soil Moisture Experiments (FOSMEX) at the Research Centre Jülich (Germany) to investigate SM detectability under a deciduous forest using L-band radiometry. They retrieved forest ground information and L-VOD from L-band TB, noting minimal differences between foliated- and defoliated states. An aluminium foil isolated ground effects, while irrigation showed that TB responded only for a few hours as the water drained through the cover (litter) layer into the soil, which remained wet for days. This suggested that L-band radiometry over forests is influenced mainly by the moisture in the cover layer, complicating SM inference (Fig. 1). Measurements with ~1.2 kg/m^2 leaf litter showed that the ~2 cm litter layer was nearly "invisible" when dry but significantly affected TB when wet. An empirical model simulating TB over time, assuming an exponential decay of litter moisture, closely matched the measured TB.

Kurum et al. (2012b) used a ground-based microwave active/passive instrument to study a Virginia Pine forest, collecting data on tree biophysical parameters and forest ground characteristics. The site had medium-sized evergreen conifers (12 m tall) and a forest ground with loose debris, needles, and an organic transition layer above mineral soil (Fig. 1). To assess the impact of surface litter, half the site was cleared under wet soil conditions. Removing the cover (litter) layer led to a detectable decrease in emissivity for both polarizations. A first-order radiative transfer model, incorporating the multilayer forest floor and ground truth data, accurately reproduced experimental results, showing that the cover (litter) layer increases TB while masking soil emissions.

Seppänen et al. (2016) conducted airborne TB measurements to study the microwave emissivity of a boreal coniferous forest under varying moisture conditions, alongside ground observations of SM and vegetation. The L-band Microwave Emission of the Biosphere (L-MEB) model (Wigneron et al., 2007), used in the SMOS SM algorithm (Section 4.1.1.1) was applied to simulate forest emissions, incorporating a moss and organic matter cover layer. With proper parameterization, the model accurately simulated forest and soil-cover emissions, achieving a correlation of 0.75 and a root-mean-square difference of 4.4 K. The study highlighted that while the humus layer complicates SM retrieval, optimising its parameterization could improve moisture estimates in SMOS observations.

Despite the successful demonstrations, modelling thermal L-band emissions from covered forest ground is still in its early stages, and further research is needed to reliably quantify SM in forests using L-band radiometry.

2.4. Snow on forest ground

Considering the effect of snow is relevant for SM and L-VOD retrievals because it is possible that the soils remain thawed under snow (e.g., Kumawat et al., 2022), and even if the soils were frozen, retrieving L-VOD is desirable in these cases. While research on how snow on forest grounds affects L-band TB is limited, microwave radiative transfer in snow and ice has been extensively studied, resulting in models (Royer et al., 2017) like MEMLS (Mätzler, 1998; Wiesmann and Mätzler, 1999), HUT-nlayers (Lemmetyinen et al., 2010), DMRT-QMS (Chang et al., 2014), DMRT-ML (Picard et al., 2013), and WALOMIS (Leduc-Leballeur et al., 2015). These MEMs vary in how they represent the snow microstructure, which is less critical at L-band due to insignificant volume

scattering (Schwank et al., 2014; 2015). Current knowledge suggests several effects of snow on L-band TB and SM retrievals.

First, while dry snow is mostly transparent at L-band (e.g., Fig. 2 in Mätzler, 2001), it influences TB through impedance matching between air and ground permittivities and through reflection and refraction at both sides of the snowpack (Schwank et al., 2014; Lemmetyinen et al., 2016). At horizontal polarisation, refraction reduces TB across all incidence angles (θ). At vertical polarisation, TB decreases for θ smaller than the Brewster angle (typically $\theta \lesssim 50^{\circ}$) but increases at larger angles (Fig. 5 in Lemmetyinen et al., 2016). Moreover, if the snow is even slightly moist, both the real and imaginary parts of its permittivity increase significantly (Mätzler et al., 1984). This increases the reflectivity of the snow surface as well as the snow layers' absorption, and thus its thermal L-band emission. The reflectivity of the underlying ground determines whether wet snow will increase or decrease L-band TB (Fig. 10 in Naderpour et al., 2017).

Second, in addition to the impacts of snow on the L-band microwave radiation transfer, it also affects the physical temperatures of the forest ground (and T_{eff}). As demonstrated in Fig. 4(c) in Naderpour et al. (2017), snow has a strong thermal insulating effect, which can lead to delayed adjustment of ground temperatures to ambient temperatures well below 0 °C for months. Conversely, during melt periods, ground temperatures show the characteristic "0 °C curtain" associated with the thermal inertia of melting snow of ~0 °C (Prince et al., 2019).

Third, the snow cover affects the surface roughness effect on radiative transfer by reducing the actual roughness and making the roughness effect larger through shortened wavelengths. The physical impact of snowpack on the ground may be particularly significant for forest grounds because of their soft organic cover layer. However, there are currently no systematic studies exploring these effects.

3. Microwave emission modelling of vegetation

A critical part of the TB forward operator is modelling the EM interaction with complex forest structures. The primary challenges concern the understanding of forest structure and its representation in a MEM. While Maxwell's equations (Maxwell, 1865) can precisely describe EM interaction, computational feasibility and adequate parametrisation of the problem are challenging. To address the trade-off between the high complexity of forest structures on the one hand and the limitation of required descriptive data on the other, radiative transfer (RT) theory is often used with statistically homogeneous assumptions. Recent advances, however, have enabled the use of exact solutions through the Multiple Scattering Theory of Foldy-Lax (MST-FL). RT equations can be derived in two ways: i) heuristically, based on physical intuition (Chandrasekhar, 1960; Section 6 of Ulaby and Long, 2014), or ii) rigorously from MST-FL using effective field and ladder approximations of Dyson's and Bethe-Salpeter equations (Frisch, 1968; Furutsu, 1975; Tsang et al., 1985).

Approximations are inherent in the RT equations (RTE), while MST-FL equations are exact solutions of Maxwell's equations for each realization of the random medium. RTE involves incoherent superpositions of intensities, while MST-FL equations use complex electric fields. Because RTE averages are pre-calculated, the computed propagation parameters are correspondingly defined by those averages. In contrast, MST-FL solves individual scatterer realisations, with results averaged afterwards. Ensemble-averaged fields and intensities are not Maxwell equation solutions, whereas MST-FL solutions for each realization are exact.

Table 2 summarizes the key differences between RT and MST-FL formulations. Typically, 20 to 30 realisations are used to obtain averaged results. RTE assumes a constant density, independent of horizontal coordinates, while MST-FL does not. Foldy-Lax equations account for structured scatterer arrangements like tree trunks and branches, while RTE averages attenuation due to the effective field approximation. In MST-FL, the attenuation is derived numerically through transmissivity averages, rather than imposed as in RTE.

Understanding how MST-FL differs from RTE, commonly used in SM and VOD retrieval algorithms (Section 4), is crucial for the forest applications due to MST-FL's potential to enhance retrieval methods (Section 3.3). Foldy-Lax equations, derived from Maxwell's equations via integral equations, T-matrices, and the extinction theorem (Foldy, 1945; Lax, 1951; Peterson and Strom, 1973; Tsang et al., 1985), essentially solve Maxwell's equations. Here, we will separately focus on these two categories, i) statistical approximation with RTE (Section 3.2) and ii) exact solution with MST-FL (Section 3.3), for forest emission modelling, as they both have and will play a role in developing forward operators.

3.1. Effective temperature of vegetation

The physical temperature of the forest canopy generally has a significant effect on the total forest TB because the emission of the vegetation is proportional to VOD as the amount absorbed is also emitted based on Kirchoff's law in LTE (e.g., Ulaby and Long, 2014). Fig. 4(a) shows simulated vertically polarised L-band TB at 40° incidence angle as a function of VOD for vegetation temperatures of 10 °C and 30 °C using the τ-ω (tau-omega) MEM (Section 3.4) with zero ω, as it mainly acts as an offset (the simulation computes the soil emission using the Mironov et al. (2009) dielectric model with SM of 0.25 m^3/m^3 and clay fraction of

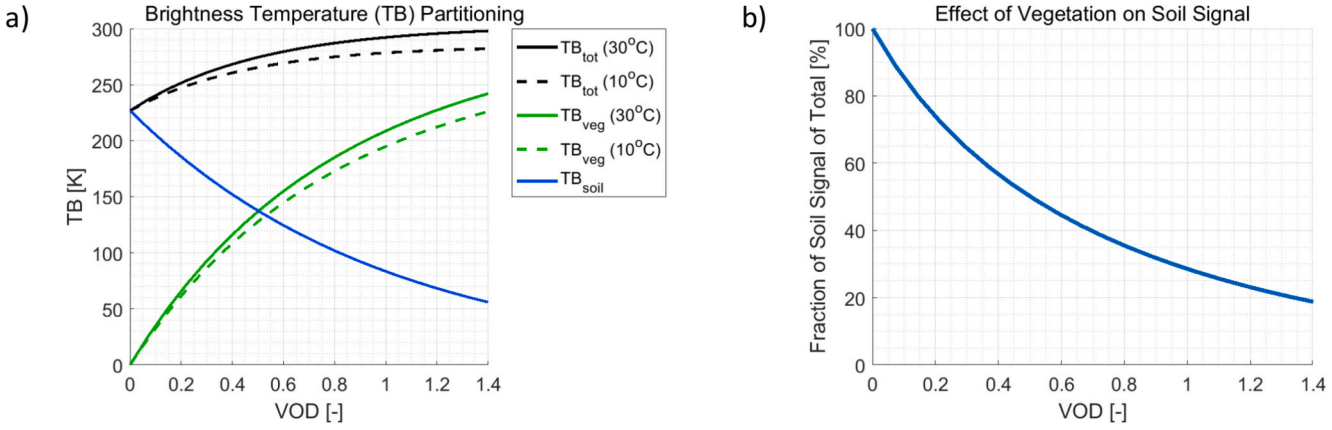

Fig. 4. (a) Simulated vertically polarised L-band brightness temperature (TB) at 40° incidence angle as a function of VOD for vegetation temperatures of 10 °C and 30 °C. The simulation computes the soil emission using Mironov et al. (2009) dielectric model with soil moisture of 0.25 m^3/m^3 and clay fraction of 5 %. The plot shows the total TB, the vegetation part of the total TB, and the soil TB transmitted through the forest. No scattering was assumed in the vegetation. (b) The fraction of the soil TB transmitted through the vegetation of the total TB.

Table 2
Relationships and similarities between the radiative transfer equation (RTE) and the multiple scattering theory Foldy-Lax (MST-FL) equation.

	RT Equation	MST-FL Equation	Key Point in Comparison
Multiple Scattering Effects	Yes	Yes	RTE includes multiple scattering of intensities. FL considers multiple scattering using complex electric fields.
Governing equation	$\frac{dI(\theta,\phi,z)}{dz} = -\kappa_e I(\theta,\phi,z) + n_0 \int_0^{\pi} d\theta' \sin\theta' \int_0^{2\pi} d\phi' \times P(\theta,\phi;\theta',\phi') I(\theta',\phi',z)$ (1,2)	$E_q^{ex} = E^{inc} + \sum_{p=1,p\neq q}^{N} G T_p E_p^{ex}, q = 1,2,\ldots,N$ (3,4,5)	RT is heuristically based using energy balance and incoherent addition of intensities s. FT is equivalent to Maxwell's equations as they are derived exactly from them. FL considers multiple scattering of trees. Trees are labelled with index p,q = 1,2,3, …,N up to N trees. E_q^{ex} is the final exciting/incident field on tree q
Directions	θ inclination angle, discretized ϕ azimuthal angle cosϕ and sinϕ harmonic expansions	$k_z = k\cos\theta$, discretized $k = 2\pi/\lambda$ θ inclination angle ϕ azimuthal angle cosϕ and sinϕ harmonic expansions	In RT, propagation of intensity is in direction of Inclinations angles and azimuthal angles. In FL, propagation of electric fields is decomposed also into Inclinations angles and azimuthal angles
Relation to scattering amplitudes $f(\theta,\phi;\theta',\phi')$	$P(\theta,\phi;\theta',\phi') = \lvert f(\theta,\phi;\theta',\phi')\rvert^2$ (1,2)	$T(\theta,\phi;\theta',\phi') = 4\pi f(\theta,\phi;\theta',\phi')$ (1,2)	RT phase matrix uses absolute value of scattering amplitude of cylinders and disks. FL T-matrix uses complex amplitude from an entire tree.
Derivations of RT and FL	using effective field approximation and ladder approximation	FL derived From Maxwell equations using integral equations, T matrices, and extinction theorem	RT originates from FL as it is derived from FL, using approximations. MST-FL just solve FL numerically without approximations
Solution of Maxwell's equation	Approximate	Exact solution of Maxwell equation for each realization of random medium	RT results cannot be validated from numerical electromagnetic software. Numerical results of FL have been validated from commercial software.
Intensity vs complex electric field	Intensities are real	Complex electric field with amplitude and phase	Maxwell's equations consist of complex electric fields.
Averaging	Phase matrices averaged quantities and then substituted in RT equations	Electric field solutions of FL are computed for each realization. Results are subsequently averaged over realisations	Averaging order differs: RT first averages single-object bistatic cross sections into phase matrices and then solves the RT equations; FL first solves full-wave Maxwell for whole-tree forests and only then averages the numerical results.
Distribution of forest components	Constant, independent of horizontal coordinates	Scatterers attached in structural manner in trees with clusters and gaps	RT assumes uniform-density cylinders/disks filling the forest (no gaps)—ok for trunks, not branches/leaves. FL computes whole-tree T-matrices directly, avoiding such assumptions.
κ_e Attenuation coefficient	Explicit attenuation κ_e in RTE equation	Attenuation obtained from averaged transmissivity that gives effective attenuation	In RT, attenuation rate is assumed to exist. In FL, no such assumption is made. In electromagnetics, bistatic scattering and transmissions are calculated for an entire forest

1. Tsang et al., 1985; 2. Tsang et al., 2000; 3. Tsang et al., 2001; 4. Tsang et al., 2022; 5. Jeong et al., 2025

5 %). The plot shows the total TB, the vegetation part of the total TB, and the soil TB transmitted through the forest. Fig. 4(b) shows the fraction of the soil TB transmitted through the vegetation of the total TB.

The plots highlight the high vegetation TB (>100 K) and the low fraction of soil TB transmitted through vegetation (<50 %) for VOD values above 0.5, typical of forests (e.g., Chaubell et al., 2022). Accurately estimating vegetation TB requires its correct physical temperature. As VOD increases, the importance of vegetation TB grows, especially as the contribution of soil TB diminishes.

Retrieving SM and VOD requires correctly estimating the different TB components in the measured TB. Traditionally, retrievals for low VOD areas assume soil and vegetation share the same physical temperature. However, in forests, vegetation temperature can differ significantly from soil temperature (e.g., Colliander et al., 2020), amplifying the challenge. Additionally, the vegetation temperature used in retrievals must effectively represent the forest components that absorb and emit radiation, a topic that has received little attention in the literature.

Global retrieval algorithms typically use modelled temperature to estimate soil T_{eff}, which is then applied to vegetation as well (e.g., Kerr et al., 2016; Chaubell et al., 2022). However, few land models separately estimate vegetation temperature, making it difficult to incorporate an informed value. Model errors further complicate the issue; a potential solution—combining air and soil temperatures—remains untested. However, it has been shown for boreal forest that air temperature is a good proxy for vegetation temperature, which could be retrieved from common climate models or reanalysis (Roy et al., 2020).

3.2. Forest emission modelling using statistical forest representation

The most common method for simulating thermal microwave emission from vegetated landscapes is RT theory, which accounts for single and multiple scattering. In RT, the forest canopy is modelled as an ensemble of tree components with known statistical properties. Because of the independent scattering assumption, RT is inherently incoherent, ignoring phase information. However, in microwave remote sensing, considering coherent effects is often not necessary as they average out over large radiometer footprints, especially at low frequencies like L-band. The RT approach remains widely utilised in microwave radiometry of vegetation for its simplicity and intuitiveness. Numerous methods for interpreting measurements solve the inverse problem of RT equations, though the multi-scale heterogeneity of forests challenges the inherent assumption of statistical homogeneity.

The "discrete scatterers" model represents the forest canopy with a unique configuration for each scatterer and a permittivity distinct from the background (air) (Lang, 1981; Tsang et al., 1985). These scatterers are typically modelled as dielectric disks (for leaves) and finite-length dielectric cylinders (for trunks, branches, and needles). Analytical scattering models for these shapes have been developed (LeVine et al., 1983, 1985; Seker and Schneider, 1988; Karam et al., 1988). The averaged single-scattering characteristics of these elements determine the canopy's total extinction (attenuation plus scattering). This model directly links to tree biophysical properties, including water content, orientation, and size distribution.

Solving RT equations becomes complex when scattering is significant, as it couples equations for polarised intensities and upward and downward radiation. Depending on the medium's effective scattering properties, the phase function is ignored (Mo et al., 1982), simplified (Schwank et al., 2018), considered small (Kurum et al., 2011; Salim et al., 2021; Chen and Tan, 2023), or combined with other terms (Karam, 1997) for analytical approximations. Methods for handling strong scattering in forest canopies with high scattering albedo include iterative techniques (Mo et al., 1982; Karam, 1997; Kurum et al., 2011; Salim et al., 2021; Chen and Tan, 2023), the two-stream microwave emission model (2S-MEM) (Schwank et al., 2018), and combined active/passive methods (Ferrazzoli and Guerriero, 1996; Chauhan et al., 1999; Martinez-Vazquez et al., 2002). These vary in complexity based on assumptions regarding absorption, scattering, and canopy structure. We will first outline forward models and their assumptions, then summarise efforts to parameterise them effectively.

3.2.1. Iterative solutions

Iterative methods are commonly used in the RT calculations to handle multiple orders of scattering (Ishimaru, 1978; Tsang et al., 1985; Ulaby et al., 1986; Fung, 1994). A scattering-related parameter (e.g., volume scattering, phase function) is chosen as a perturbation parameter, and the RT equation is cast solved iteratively, generating successive approximations (zeroth order, first order, etc.). In each iteration, the previous order's TB serves as the excitation source. This process continues until the solution converges to a desired level of accuracy. The iterative approach allows for physically interpretable and separable scattering paths but increases computational cost, making it less appealing for use in inversion-based retrieval methods.

3.2.1.1. Successive orders of scattering. The most common perturbation parameter is the phase function, representing collective scattering from a unit volume in the vegetation. This technique, known as "successive orders of scattering" (SoS) (Lenoble, 1985), expands emission into a series of scattering mechanisms, which are added iteratively to the overall emission. In formal terms, the N$^{\text{th}}$-order RT solution of *p*-polarised emission can be written as:

$$e_{sp}^{(N)}(\theta) = e_{sp}^{(0)}(\theta) + \sum_{n=1}^{N} \Omega_p^{(n)}(\theta) \tag{1}$$

where $\Omega_p^{(n)}(\theta)$ represents the n^{th}-order multiple-scattering contribution to the zero-order solution (i.e., $e_{sp}^{(0)}(\theta)$), resulting from ground and vegetation layer emissions scattered *n*-times by the vegetation constituents representing the forest canopy layer. The zero-order solution neglects scattering, with the phase function set to zero (Mo et al., 1982), meaning that the vegetation layer is considered as an effective medium with no volume scattering but a given attenuation (denoted as VOD or τ_p). Scattering is introduced through the single-scattering albedo (denoted by ω_p), forming the $\tau - \omega$ model. For forest canopies, the single-scattering albedo caused by large scatterers with dimensions of the order of the wavelength, such as branches and trunks, is around 0.5 to 0.6 (see Ferrazzoli et al. (2002); Kurum et al. (2011)), requiring higher-order solutions for better vegetation emission estimates.

Kurum et al. (2011) derived the first-order scattering solution (i.e., $e_{sp}^{(1)}(\theta)$) explicitly and validated it with truck-based TB measurements at L-band over small deciduous trees. This new formulation adds a new scattering term (i.e., $\Omega_p^{(1)}$) to the $\tau - \omega$ model (the zero-order RT solution), accounting for single scattered radiation from vegetation constituents in the layer caused by ground and vegetation layer emissions. This enhanced model improves upon the tau-omega model by considering scattered vegetation and ground radiation, which significantly influences observed emissions. Additionally, Feldman et al. (2018) extended this work by implementing a ray tracing method to include simplified first-order scattering terms, aiming to resemble theoretical terms from the previous study. This simplified model is designed for use in spaceborne retrieval algorithms and represents the first attempt to explicitly address higher-order scattering terms in a retrieval algorithm at a satellite scale, particularly for quantifying multiple-scattering effects from grasslands to forests.

Salim et al. (2021) conducted numerical iterations up to the fourth order to examine the effects of multiple scattering in a vegetation layer with a high scattering albedo and optical thickness. At an observation angle of 40 degrees, their calculations revealed that contributions to the RT from the zeroth to the second order were 79 %, 15.6 %, and 3.8 % for vertical polarisation, and 82.9 %, 12.84 %, and 3.2 % for horizontal polarisation, within a forest composed of aspen trees with a VWC of 15 kg/m^2 associated with 0.24 trees/m^2. Chen and Tan (2023) introduced

an efficient numerical iterative procedure for computing multiple scattering to RT equations, particularly in situations with strong forward scattering, as observed in forests comprising tree trunks with electrical dimensions comparable with the observation wavelength. Their approach involves dividing the phase matrix into forward scattering and non-forward scattering directions, redefining scattering parameters by excluding forward scattering within a specific angular range around the forward scattering direction. This reformulation resulted in new RT equations that lead to faster convergence, reducing the number of orders required for convergence.

3.2.1.2. Albedo expansion. Karam (1997) rearranged the RT equations with respect to the scattering coefficients (i.e., single scattering albedo defined as the ratio between scattering and extinction (= sum of scattering and absorption)). He performed an iterative process on these modified RT equations, treating the albedo as a small perturbation parameter. This iterative approach led to explicit expressions for the zero and first-order solutions of the albedo expansion. Notably, the first-order solution in albedo was shown to be equivalent to Peake's emissivity formula (Peake, 1959) for canopies with uniform physical temperature. The solution led to the definition of specular and diffuse albedos, which are scene albedos and different from the single-scattering albedos of vegetation components. In active microwave remote sensing terms, the specular albedo can be interpreted as the power scattered by the ground in the specular direction with a two-way loss in the vegetation layer, while the diffuse albedo represents the portion of incident power scattered from the layer into a hemisphere above the layer.

Karam (1997) established equations for the first-order diffuse albedo, and it is theoretically feasible to derive higher-order diffuse albedo through additional iterations. The influence of multiple scattering is integrated into the diffuse albedo. It is worth emphasising that the diffuse albedo is subtracted from the zero-order solution, contrasting with adding solutions related to multiple-scattering orders to the zero-order solution in the SoS method. Furthermore, the single scattering albedo, characterising the proportion of the incident radiation that undergoes scattering as opposed to absorption and is related to vegetation constituent properties, can be combined with both specular and diffuse albedo to account for the directional distribution of scattered radiation throughout the medium.

3.2.2. Two-stream emission model

Schwank et al. (2018) adopted the two-stream microwave emission model (2S-MEM) originally used in the Microwave Emission Model of Layered Snowpacks (MEMLS) (Wiesmann and Mätzler, 1999) for its use in the simulation of TB above vegetated landscapes. The simplest version of the 2S-MEM adopted to vegetation involves the assumption that vegetation can be represented by a single "soft-layer" (diffuse layer) that assumes neither reflection nor refraction at its upper interface. Thereby, the single "soft-layer" incorporates a few key parameters such as single-scattering albedo and optical depth, making the single-layer version of the 2S-MEM well-suited for implementation in inversion-based retrieval algorithms (as it is demonstrated in, e.g., Li et al., 2020 and Kumawat et al., 2022). From a forward modelling perspective, the 2S-MEM can be configured with multiple layers, allowing for the consideration of vertical variations in forest structure. However, the 2S-MEM accounts for multiple scattering and multiple reflections among the vegetation layers and between the vegetation and the ground.

In MEMLS, the scattering layer is conceptualized as a series of horizontal planar layers with flat boundaries. Each layer is characterized by its interface reflectivity, its internal (volume) reflectivity, emissivity, and transmissivity, along with its associated temperature. The interaction between up- and downwelling TB at the layer boundaries is governed by energy conservation principles. To determine the radiative properties of each layer, the RT equations are established. Under the assumption of local homogeneity and isotropy in the layers, these RT equations are then simplified to a second-order differential equation, facilitating the calculation of the propagation of upwelling and downwelling radiations.

3.2.3. Compound model "MEMLV" using discrete scatter model and 2S-MEM

To implement the 2S-MEM in modelling forested-land emission, the compound model, named "Microwave Emission Model for Layered Vegetation" (MEMLV), was developed (Zhou et al., 2023; Zhou et al., 2024). It is based on a hybrid approach that combines the Single-Layer Discrete Scatter Model (SL-DSM) (Lang and Sighu, 1983; Zhou et al., 2020), the Multi-Layer 2S-MEM (Schwank et al., 2018), and a Tree Structure Model (TSM) describing the vegetation structure by statistical means to simulate TB of forested land.

The SL-DSM represents a vegetation layer as an effective mean medium with embedded dielectric scatterers to calculate the single scattering albedo (ω) and VOD (τ) of this layer. The embedded scatterers represent tree constituents such as leaves/needles, branches and trunks. Their scattering amplitudes, which are dependent on the scatterers' size, orientation and permittivity, are computed based on the approximate analytic approach developed in (Seker and Schneider, 1988). An example of the scattering pattern of a vertically oriented dielectric cylinder having radius of $r = 1$ cm and length of $l = 26$ cm is shown in Fig. 5 (c).

A single layer, however, is not enough to adequately represent the complex structure of forest canopies. To characterize tree macro-structures as well as the statistical distributions of their constituents, the TSM was developed. The TSM represents the canopy as multiple stratified layers, with each layer described by certain probability density functions (PDFs) expressing the statistical distributions of canopy constituents' dimensions, orientation, and occurrences. The primary goal in developing the TSM was to describe the structure of a forest canopy using a minimal set of parameters most relevant to microwave RT. An example of a three-layer ($N = 3$) conical tree model is shown in Fig. 5 (Zhou et al., 2024), which shows that the TSM can be parameterized according to the tree crown dimensional parameters, the shape parameter α, and the canopy-gap parameter β. In addition, the size- and orientation distribution (represented by PDFs) of tree constituents (e.g. branches of different sizes and orientations) in each layer can also be adjusted in order to represent realistic tree physiological characteristics. Finally, the upwelling TB of the multi-layer structure, is obtained by the sum of the TB emitted from each layer of the stack (red wide arrows in Fig. 5(b)) weighted by their corresponding surface area S_j (Fig. 5(a)). To have a realistic parameterization of the TSM, the ground-truth for a fir tree collected from the "JRC experiment" (Zhao, 2013) has been used.

Finally, the simulated TB is used in a cost function to find the effective VOD (τ_{eff}) and albedo (ω_{eff}) of the TB emitted from an equivalent single-layer canopy to bridge the gaps between sophisticated multi-layer forward modelling and retrieval practice. This has been further described in section 3.4.2.

3.3. Forest emission modelling using real forest geometry

For the forest emission modelling, the scatterer (a tree) has trunks, branches, and leaves attached together in a structured manner with an architectural pattern. As.

Table 2 shows, the RTE phase matrix and Foldy-Lax T-matrix are essentially the same. However, while the RTE phase matrices are additive sums of the bistatic cross sections of trunks, branches, and leaves

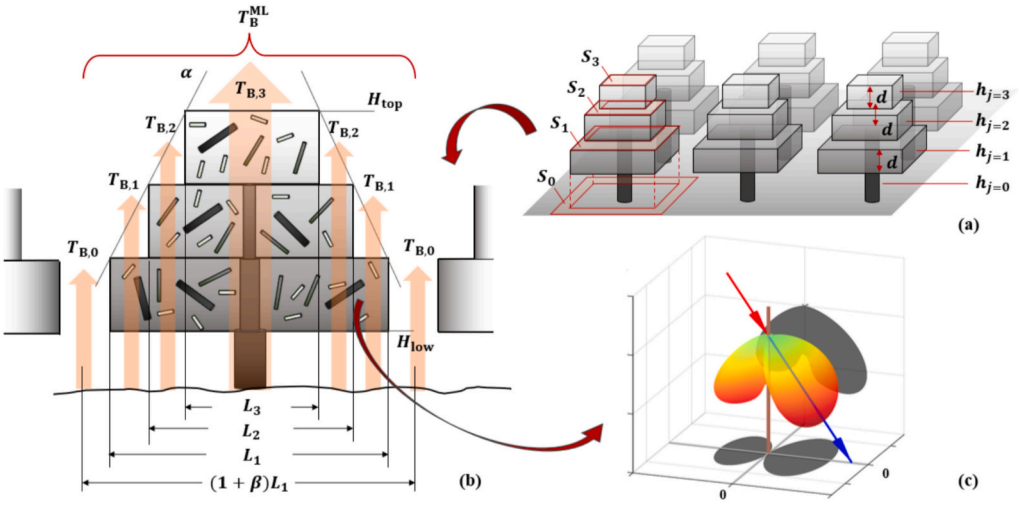

Fig. 5. Illustration of the TSM. (a) Panoramic forest structure with marked layer height h_j, thickness d, and surface area S_j. (b) Side view of a tree with marked macro parameters H_{low}, H_{top}, α, β, and L_1, together with $T_{B,j}$ emitted from stacks of j layers and the total upwelling T_B^{ML} (c) Three-dimensional spatial patterns of scattering amplitudes F (*H*,*H*) simulated for vertically oriented cylinders illuminated by a wave incident at a nadir angle of 40°. This figure is reproduced from Zhou et al. (2024).

uniformly positioned with a uniform number of density n_0, the MST-FL can retain the impact of the realistic forest structure in emission modelling, as discussed in Section 3.

In the past, exact solutions of 3D Maxwell equations for vegetation volume scattering and rough surface scattering were deemed formidable and not practical. However, the fast methods were started in 2022 and have been developing at a rapid pace making exact solutions of Maxwell equations possible and lookup tables assembled quickly. The results of fast method have accuracies validated by commercial electromagnetic software such as FEKO for small sample size such as 8 trees. On the other hand, the fast hybrid methods are much more efficient than commercial software in both memory and CPU. Fast Hybrid methods have been used to solve a large sample forest with 300 trees which is not possible with commercial software such as HFSS or FEKO.

3.3.1. *Fast hybrid method of numerical solutions of MST-FL*

The work of full-wave simulations of forests began with initial work on uniformly positioned cylinders (Huang et al., 2017, 2019). Later work modelled realistic trees with trunks and primary and secondary branches attached to the trunk (Gu et al., 2022; Jeong et al., 2023a; 2023b). The computation efficiency of the initial Hybrid Method (Gu et al., 2022) was significantly improved with the development of the Fast Hybrid Method (FHM) (Jeong et al., 2023a; Jeong et al., 2023b).

FHM consists of three steps (Jeong et al., 2023b): i) Extraction of the T-matrix (Gu et al., 2022; Jeong et al., 2023a; 2023b) of a tree by utilising the method of moments (e.g., Altair, 2023). The tree is enclosed by a cylinder, and the T-matrix elements relate incident waves to scattered waves outside the cylinder (Fig. 6). ii) The MST-FL (Jeong et al., 2023b; Tsang and Kong, 2001) is used to obtain the multiple scattering among trees, and the various orders of the multiple scattering solutions are then solved iteratively. iii) The Triple FFT is applied to compute each order of the multiple scattering solutions, reducing the CPU time and memory requirements significantly (Jeong et al., 2023a).

To ensure that the FHM gives accurate solutions of 3D Maxwell equations, the simulated solutions for a smaller number of trees were compared with method of moments solutions (Jeong et al., 2023a). However, the method of moments can give results only for a small number of trees and requires an overwhelming amount of memory for a large number of trees. For example, using FEKO (Altair, 2023) problems with a tree height of 17 m have been limited to 8 trees. The comparisons to these cases have demonstrated agreement with the scattered field solutions of Maxwell equations and the electric field spatial distributions

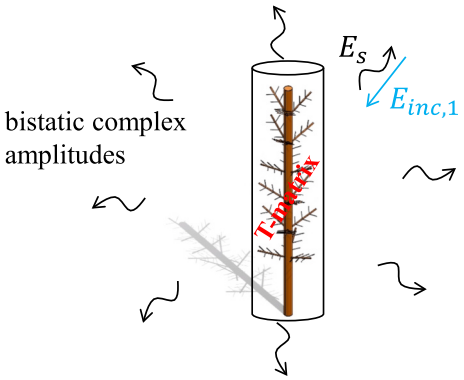

Fig. 6. In MST-FL numerical solutions, an entire tree is treated as a single scatterer to obtain the T-matrix of a tree.

at the bottom plane of the trees. Large-scale simulations with 91 trees that are 17 m tall were carried out to compute the transmissivity through the trees demonstrating its applicability for use in remote sensing problems (Jeong et al., 2023b). The spatial distribution of electric fields also shows the effects of gaps and shadows; the amplitude of the electric field can be as high as twice that of the incident wave because of constructive interference. These effects cannot be simulated with radiative transfer approaches.

3.4. *Bridging the gap between forward model complexity and retrieval requirements*

While the TB forward modelling aims to capture fundamental physical mechanisms and represent the natural complexity of scattering and absorption over forested land, the retrieval of SM and VOD has typically relied on simplified MEM implementation. The reduced number of parameters and minimal a priori information make them more convenient for operational applications. The challenge is finding the balance between the complexity, accuracy, and feasibility. In general, there are three ways to bridge the forward modelling with retrieval applications: simplified MEM, effective parameterisation, and look-up tables.

3.4.1. Simplified MEM in the retrieval processes

The tau-omega model underpins nearly all SM retrieval algorithms due to its simplicity, ease of inversion, and implementation, along with extensive validation in areas with light to moderate vegetation (Jackson and Schmugge, 1991; Wigneron et al., 2007). However, theoretically, its applicability diminishes in large, heterogeneous vegetation with electrically large scatterers, such as branches and trunks, at the L-band.

The single-layer 2S-MEM model (Schwank et al., 2018), which accounts for multiple reflections and scattering, relies on a few key parameters, including scattering albedo and VOD, making it suitable for inversion algorithms (Gao et al., 2020; Li et al., 2020; Holmberg et al., 2024). In addition, a simplified first-order RT model (Feldman et al., 2018) is implemented for parameter inversion, as its first-order scattering terms are expressed in terms of key vegetation parameters like VOD and scattering albedo.

Vegetation emission can also be modelled using the bulk parameters for the total transmission and scattering (Colliander et al., 2018), making it compatible with inversion algorithms (Colliander et al., 2020; Ambadan et al., 2022). However, comparisons between these parameters and those of the tau-omega or the 2S-MEM (and their derivatives) require caution, as they are fundamentally defined differently.

3.4.2. Effective parameters for simplified retrieval implementation

Ferrazzoli et al. (2002) first suggested that the tau-omega model can implicitly account for multiple scattering through effective parameters. Vegetation parameters VOD and scattering albedo are calibrated using a multiple-scattering model (Ferrazzoli and Guerriero, 1996) and measured canopy data. Subsequent studies refined and validated this approach against radiometric measurements (Saleh et al., 2005; Della Vecchia et al., 2007; Della Vecchia et al., 2010; Grant et al., 2008). Kurum (2013) later established a direct physical link between effective vegetation scattering parameterisation and the tau-omega model, incorporating multiple scattering and single-scattering effects into an effective scattering albedo while preserving the model's form. Unlike single-scattering albedo, which depends solely on vegetation properties, the effective albedo is shown to be dynamic, influenced by factors like SM. It also exhibits lower sensitivity to observation angle and polarisation, aligning more closely with the empirical values used in SM retrieval algorithms.

Chen and Tan (2023) introduced a method to parameterise the RT model using an effective tau-omega formulation that accounts for multiple scattering. By equating higher-order and zero-order RT solutions in two sequential steps, they determined the effective optical depth and effective scattering albedo. Their results showed that the vegetation layer transmissivity derived from the equivalent parameter is considerably higher than theoretical VOD values from RT solutions and closely matches full-wave simulations (Huang et al., 2017). This underscores the importance of considering multiple scattering and heterogeneity effects to extend RT theory's applicability.

The MEMLV (Section 3.2.3) further optimises the retrieval of effective VOD (τ_{eff}) and scattering albedo (ω_{eff}) using simulated TB from realistic tree structures. This two-parameter retrieval depends on forest physiological parameters such as tree height, canopy gap, and dry-matter fraction of constituents (Zhou et al., 2024). By parameterising retrieval algorithms with simulated (ω_{eff}) based on external sensor data–e.g., tree height from Lidar or forest-hole fraction from optical sensors–VOD retrievals could become more dynamic and accurate.

3.4.3. Reducing the number of unknown retrieval parameters with other data sources

Beyond simplifying forward MEMs, the number of free parameters in retrieval algorithms can also be reduced by incorporating auxiliary data. For example, VOD retrieved from multi-angle SMOS TB can support SM retrieval from single-angle SMAP TB, thereby reducing the risk of underdetermined inversions. Lidar-derived vegetation structure can help constrain parameters such as the single-scattering albedo. Likewise, active and passive microwave observations at other frequencies (e.g., C- and X-band) provide complementary information in regions with dense vegetation, where shorter-wavelength TBs are dominated by vegetation emission. In all these cases, auxiliary data facilitate the separation of soil and vegetation contributions, thereby improving the robustness of L-band two-parameter retrievals. Nevertheless, auxiliary datasets themselves introduce uncertainties that may propagate into the retrieved parameters, underscoring the need for careful error propagation analysis when integrating such data into retrieval algorithms.

3.4.4. Look-up tables

Retrievals can also be performed using pre-computed multi-dimensional look-up tables (or data cubes), allowing complex forward models to be applied with a limited number of available parameters. This approach has been used for SM retrieval with L-band radar (Kim et al., 2017) and for retrieving meltwater amounts in ice sheets using L-band radiometry (Mousavi et al., 2022).

The results of the forward MEM can be structured based on available ancillary data, such as tree height, forest fraction, tree density, clumping, and phenology. For unavailable parameters—such as exact tree location and branch geometry—ensemble averages from simulations are used. Since multi-dimensional look-up tables can be large, computational methods like coarser discretisation and multi-dimensional interpolation help manage their size while maintaining retrieval accuracy.

4. SM and VOD retrieval approaches and products

4.1. Retrieval approaches

This Section summarizes the main approaches for retrieving SM and L-VOD in forests. For soil covered by vegetation, retrieval typically involves inverting an appropriate MEM. While an accurate MEM should account for various processes affecting emission from soil and vegetation, simpler models are generally preferred for manageability, despite reduced representation of specific properties, see Section 3.4. For forests, the procedure requires specific attention due to the limited availability of experimental data and the complexity of the scattering and emission processes within the canopy.

Before the launch of SMOS in 2009, passive L-band observations over forests were limited but prompted key empirical studies that informed early retrieval algorithm development. Airborne ESTAR radiometer measurements over coniferous forests in Virginia showed a strong correlation between H-polarised TB and AGB, and also detected poorly drained soils (Lang et al., 2000). Subsequent experiments in Germany's Jülich Forest (Guglielmetti et al., 2007, 2008) and over an Italian poplar plantation (Santi et al., 2009) used multifrequency and bidirectional measurements to estimate forest albedo and L-VOD under foliated and defoliated conditions. These early studies, though empirical, provided initial estimates of RT model parameters for forests (Wigneron et al., 2007). They confirmed that L-band optical depth was lower than at C- and X-band—especially in leaf-off conditions—and that forest albedo typically ranged from 0 to 0.12. Litter also played a notable role in L-band signal behaviour, particularly in higher latitudes.

Advanced models, such as the two-stream microwave emission model (2S-MEM) and first-order radiative transfer approaches, enhance the physical realism of canopy scattering and emission by accounting for multiple scattering effects and vertical heterogeneity in vegetation structure (Section 3). In parallel, dual-channel and multi-angular inversion algorithms have been developed to improve the simultaneous retrieval of SM and VOD, with spatially constrained and regularised approaches increasing retrieval robustness and reducing noise. Despite these advancements, simplifying assumptions—such as uniform canopy layers or fixed scattering albedo—can limit the ability to capture the full complexity of forest heterogeneity and temporal dynamics, warranting further investigation. In particular, parameter uncertainties in scattering albedo and transmissivity remain a significant source of

retrieval errors and represent a key area for future improvement (e.g., Ambadan et al., 2022; Li et al., 2015).

4.1.1. Approaches using SMOS

4.1.1.1. SMOS level 2 and level 3 algorithms. The average ground resolution of SMOS is about 43 km. The Level 1 (L1) data product provides multi-angular and multi-polarisation L-band TB on the ISEA-4H9 grid (DGG), with a 15 km internode distance for each overpass and grid point (Suess et al., 2004). Over land, Level 2 (L2) products include SM and L-VOD (Kerr et al., 2012, 2020). The retrieval minimises a cost function based on the squared weighted differences between measured and modelled TB data for various observation angles and polarisations. The tau-omega MEM (Wigneron et al., 2007) is used with inputs from land cover, soil texture, topography, and leaf area index (LAI); TB is derived from the modelled emissivity and surface temperature data from European Centre For Medium-Range Weather Forecasts (ECMWF). Each grid node covers an area subdivided by land categories, with the retrieval done for the dominant fraction, while the other fractions contribute fixed TB values. After the initial formulation, the algorithm evolved; in particular, changes were applied to the soil dielectric model and the land cover database. In the latest version (V700), low vegetation and forest areas were merged into a single fraction, smoothing retrievals and reducing retrieval failures. The SMOS L1 and L2 science data can be downloaded from the ESA SMOS Online Dissemination Service after registration (https://smos-diss.eo.esa.int/oads/access/). The Level 3 (L3) algorithm is similar to the L2 algorithm but uses a "slowly varying optical depth" concept over a 7-day period with a 25 km internode distance (Al Bitar et al., 2017). SMOS L3 data are available from both the ESA Dissemination Service and from the web application of the Centre Aval de Traitement des Données SMOS (CATDS) at the following link: https://www.catds.fr/sipad/.

When forests are the dominant fraction, the algorithm retrieves SM and L-VOD using fixed values for albedo (ω) and soil roughness parameters (HR, NRV, and NRH) as defined by Wigneron et al. (2007). This approach required developing a forward model providing accurate estimates of ω, HR, NRV, NRH, and a realistic prior value for L-VOD τ, for initialising the retrieval process. ω and the prior value of τ were obtained using the method of Ferrazzoli et al. (2002), but the fitting process was extended to all forests using only LAI. The Tor Vergata model (Ferrazzoli and Guerriero, 1996) was used to generate lookup tables relating simulated multi-angular emissivities (for the SMOS configuration) to SM, for three aggregated forest types: needle-leaf, broad-leaf, and mixed. Geometrical and biophysical values required by the MEM were related to the maximum yearly LAI value (LAI_{max}) using allometric equations. Seasonal changes, such as defoliation and understory vegetation, were accounted for by variations in LAI. Rahmoune et al. (2013) detailed this process, and a constant ω of 0.08 was determined.

In the latest V700 version, the parameters were refined using multiyear SMOS data. The maximum yearly τ is now linearly related to LAI_{max}, with coefficients of 0.18 for broadleaf and 0.14 for needleleaf forests. Multiyear data suggested a slight reduction in albedo, with both a three-parameter algorithm (retrieving SM, τ, and ω) and TB measurements from tropical forests of Amazonia and Congo confirming ω of 0.06 for tropical forests (Vittucci et al., 2017; Parrens et al., 2017). This value was extended globally, though boreal forests showed slightly higher ω. HR was set at 0.3, and NRV and NRH were fixed at 0 and 2, respectively.

4.1.1.2. SMOS-IC algorithm. An alternative SMOS product, developed by INRA (Institut National de la Recherche Agronomique) and CESBIO (Centre d'Etudes Spatiales de la BIOsphère) called SMOS-INRA-CESBIO (SMOS-IC) aimed to create a simpler algorithm with less reliance on auxiliary data compared to the SMOS L2 and L3 algorithms. The SMOS-IC data are disseminated by the CTADS at the following link: https://data.catds.fr/cecsm/Land_products/L3_SMOS_IC_Soil_Moisture/. The L2 and L3 algorithms faced issues due to uncertainties in land cover and other auxiliary data, especially with mixed pixels. SMOS-IC uses the same grid as SMOS L3, with the retrieval based on minimising the difference between the SMOS-measured multi-angular TB and those generated by a zeroth-order MEM. Unlike the L2 and L3 algorithms, SMOS-IC retrieves SM and L-VOD over wholly homogeneous pixels (Fernandez-Moran et al., 2017). A constant initial value of 0.2 m^3/m^3 was set for SM, and L-VOD was initialised with a yearly average computed from previous runs. Weighted averages were used for fixed parameters like vegetation albedo and soil roughness, with land cover fractions as weights. For forests, albedo and HR were set to 0.06 and 0.30 for the L2 and L3 algorithms, and NRV and NRH were − 1 and 1, respectively. Version 2 introduced several improvements (Wigneron et al., 2021). Particularly, an improved multi-temporal L-VOD retrieval was introduced, assuming slow temporal changes of L-VOD.

4.1.1.3. Other approaches using SMOS. Li et al. (2020) included the 2S-MEM (section 3.2.2) in the SMOS-IC algorithm as an alternative for the originally implemented tau-omega MEM. SM and L-VOD retrievals were compared against the ones obtained using the standard SMOS-IC. Details about this comparison are discussed in 4.2.1.

Bai et al. (2022) attempted a different retrieval approach. The multi-angular and multitemporal TB measured by SMOS was used to simultaneously retrieve SM, L-VOD, the albedo, and the roughness parameters using only single polarisation (vertical or horizontal).

Another alternative approach was based on the use of neural networks (Rodríguez-Fernández et al., 2015). The objective was to produce near-real-time retrievals with accuracy comparable to the L2 and L3 products. The network was trained using the SM global data set of ECMWF in addition to measured TB data at both polarisations and in an angle range of 25° - 60°. Improvements achieved by adding ASCAT backscattering coefficients and/or MODIS NDVI data were assessed. Rodriguez-Fernandez et al. (2017) trained the network using the SMOS L2 SM, besides dual polarisation measurements in the 30° - 45° range.

Thanks to the multiangle capabilities of SMOS, a new approach to estimate biomass directly from multi-angular L-band TB a neural network retrieval approach was proposed in Salazar-Neira et al. (2023), thus eliminating the use of L-VOD.

4.1.2. Approaches using SMAP

The SMAP TB measurements are obtained using a single feedhorn and parabolic mesh reflector. The footprint is about 40 km, and the average incidence angle is 40° (Piepmeier et al., 2017). A Backus-Gilbert optimal interpolation scheme, taking advantage of the SMAP radiometer oversampling is used to generate an optimally interpolated TB record on a 9-km grid, maintaining the native 40-km resolution.

4.1.2.1. SMAP single and dual channel algorithms. The SMAP Single Channel Algorithm (SCA) uses one polarisation (vertical or horizontal). TB is converted to emissivity using GMAO GEOS-5 temperature data, which is then corrected for vegetation and surface roughness to obtain soil emissivity. The Fresnel equation calculates the soil permittivity, and a dielectric mixing model retrieves SM. Only SM is retrieved, while L-VOD is treated as a known parameter based on the linear relation with VWC (Jackson and Schmugge, 1991), though non-linear improvements have been considered (O'Neill et al., 2021). VWC is computed from NDVI measured by MODIS, using foliage and stem water content estimates, the latter depending on the vegetation type. The stem water content could refer to the water content residing in the herbaceous stems of crops (e.g., corn stalks) or the woody stems of trees (Chan et al., 2013). For forests, fixed parameters include albedo (= 0.05), HR (= 0.16), NRV (= 2) and NRH (= 2). The *b* coefficient used in the L-VOD to VWC (kg/m^2) relation is 0.10 for evergreen and 0.12 for deciduous forests. The stem factor varies widely, from 7.98 for deciduous

needleleaf to 19.15 for evergreen broadleaf forests.

The Dual Channel Algorithm (DCA) uses both H-polarised and V-polarised TB observations to simultaneously retrieve SM and L-VOD by minimising the differences between modelled and measured TB. Similar to the SCA, some estimates of model parameters (e.g., surface temperature, surface roughness, and ω) are provided via ancillary data, but soil roughness and ω are parameterised differently. The original DCA was modified by optimising the roughness and ω and named MDCA (Chaubell et al., 2020), with ω of 0.07 for all forest types. A further refinement introduced a regularised minimisation cost function; the algorithm was named RDCA (Chaubell et al., 2022).

The SMAP SM products are mapped onto the Equal-Area Scalable Earth (EASE) grid, available at nominal (36 km) and enhanced (9 km) spatial resolutions. A near-real-time L2 product is also available at nominal resolution (O'Neill et al., 2022). L3 products provide gap-free, near-global daily coverage by aggregating L2 data, and are available at both nominal (O'Neill et al., 2023a,c) and enhanced (O'Neill et al., 2023b,d) resolutions. Additionally, Level 4 products offer model-assimilated outputs, including root-zone soil moisture (Reichle et al., 2019) and net ecosystem exchange of carbon (Kimball et al., 2025), providing valuable information for land surface and carbon cycle studies.

The SMAP SM L2 and L3 products are primarily distributed through the National Snow and Ice Data Center (NSIDC) Distributed Active Archive Center (DAAC) at the following main access link: https://nsidc.org/data/smap/data.

Further dual polarisation retrieval options, such as the Land Parameter Retrieval Model (Owe et al., 2002) and the Extended Dual Channel Algorithm, are described in O'Neill et al. (2021).

4.1.2.2. Other approaches using SMAP. Konings et al. (2016, 2017) proposed a multitemporal algorithm, using dual polarisation TB measured by SMAP in at least two subsequent dates (MTDCA). Similar to previously illustrated algorithms, the retrieval is based on minimising the differences between measured data and the ones simulated by the tau-omega MEM. The algorithm uses a moving window to combine retrievals from two consecutive overpasses, assuming L-VOD to be constant over those overpasses. This regularisation approach contrasts with the Tikhonov regularisation used by Chaubell et al. (2022) to regulate the change of the retrieved VOD, especially under dense vegetation and low-sensitivity conditions. The algorithm also retrieves the albedo, again using a multitemporal approach. The albedo was assumed to be constant over a one-year time interval. Retrievals of SM and L-VOD will be illustrated in the following subsections. On average, the retrieved albedo over pixels dominated by forests was in the 0.07–0.10 range, slightly higher than the default values adopted in other SMOS and SMAP algorithms. Variations related to forest classes were moderate.

The SMAP-IB algorithm illustrated in Li et al. (2022a) retrieves SM and L-VOD using SMAP dual polarisation TB, utilising an approach similar to the V2 version of SMOS-IC. In particular, the same parametrisation is used, as well as the multitemporal technique, which is extended to SM. Zeng et al. (2020) proposed a soil moisture index (SMI) that differentiates the impacts of SM and core disturbance factors (i.e., vegetation and surface roughness) on emissivity and polarisation difference ratio, which can track SM variations independently of the tau-omega MEM. The SMI retrieval approach was also applied to higher frequencies by Meng et al. (2024).

4.1.3. Machine learning approaches using SMOS and SMAP for SM retrieval

Conceptually, SM estimation integrates remote sensing observations, ground measurements, and environmental variables through predictive modelling frameworks (Batchu et al., 2023). This integration links data fusion, model architecture, and environmental heterogeneity to improved SM prediction accuracy (Wang et al., 2023). Deep learning techniques using 's SMAP TBs have become central to advancing understanding of land–atmosphere interactions, hydrological processes, and climate change impacts (Klingmüller and Lelieveld, 2021).

Since the launch of SMOS, SM retrieval has evolved from the inversion of physically based MEMs to data-driven approaches, advancing from early neural network implementations (Rodríguez-Fernández et al., 2015; Srivastava et al., 2013) to modern deep learning architectures (Wang et al., 2023; Zhang et al., 2023). Traditional approaches, such as random forests and shallow neural networks, improved retrieval accuracy but struggled with missing data and spatial heterogeneity (Srivastava et al., 2021). In contrast, deep architectures—particularly convolutional neural networks (CNNs), long short-term memory (LSTM) models, and hybrid combinations—offer enhanced feature extraction and temporal modelling capabilities (Ge et al., 2018; Li et al., 2022b; Alemohammad et al., 2018), despite limited interpretability (Klingmüller and Lelieveld, 2021; Huang et al., 2023). Numerous studies have shown that these models can outperform traditional methods (Ge et al., 2018; Rodríguez-Fernández et al., 2015), with hybrid and physics-informed variants further improving accuracy and reducing bias (Orth, 2021; Wang and Xu, 2021; Han et al., 2023). Models trained on in situ and simulated datasets using MEMs effectively capture spatial and temporal variability, achieving RMSE reductions of 10–20 % relative to standard methods (Wang et al., 2021; Lee et al., 2024e).

Beyond forests, deep learning has enabled substantial gains in spatial and temporal resolution, including downscaling from SMOS and SMAP footprints (~25–36 km) to ≤1 km (Ning et al., 2023; Zhang et al., 2024b; Wen et al., 2021; Senanayake et al., 2024), and producing daily or near-real-time estimates via recurrent architectures such as LSTM and ConvLSTM (Zhang et al., 2023). Computationally, random forests and shallow networks remain efficient and scalable for operational use (Ning et al., 2023), whereas complex models with attention mechanisms or physics-informed designs demand higher resources but yield superior accuracy (Zhang et al., 2024b; Xu et al., 2023). Consequently, practical deployment requires balancing model complexity and efficiency (Alemohammad et al., 2018).

Interpretability remains a key consideration. Explainable AI (XAI) methods—such as SHAP values, permutation importance, and attention visualisation—are increasingly used to elucidate deep learning behaviour (Wang et al., 2023; Huang et al., 2023). Meanwhile, physics-informed and hybrid frameworks enhance both interpretability and physical consistency by embedding domain-specific constraints and principles (Singh and Gaurav, 2024; Xu et al., 2023).

4.1.4. Effect of forest type

Key differences arise when applying retrieval algorithms to temperate and boreal forests compared with tropical regions. Tropical forests generally exhibit stable SM climatology but complex and highly variable canopy water content dynamics (Ma et al., 2023; Monsivais-Huertero et al., 2020). Tropical broadleaf forests, characterized by low albedo and intricate VOD seasonality, require tailored parameterisations (Rahmoune et al., 2013; Vittucci et al., 2016). Incorporating structural information from lidar missions can help address this complexity, for example, by initialising VOD in retrieval schemes such as the ESA SMOS algorithm (Vittucci et al., 2023).

In contrast, boreal and temperate forests pose challenges related to snow cover, freeze–thaw cycles, and thick litter layers (surface covers) that affect microwave emission (e.g., Kumawat et al., 2024; Holmberg et al., 2024). Owing to the frost hardiness of boreal tree species, the dielectric properties of tree tissues change markedly as the temperature drops below freezing. This results from complex processes involving tissue shrinkage and water redistribution among different cellular

compartments. Moreover, these dielectric properties continue to vary with further decreases in temperature (e.g., Lin, 1967a, b; El-rayes and Ulaby, 1987; Repo, 1992; Beck et al., 2004). Coniferous forests, in particular, display substantial seasonal and temperature-dependent variations driven by canopy interception and freeze–thaw dynamics (Salim et al., 2021; Zheng et al., 2017; Kurum et al., 2012a; Li et al., 2019). Accounting for seasonal and phenological processes—especially rapid canopy water fluctuations in tropical regions and freeze–thaw transitions in boreal zones—is therefore critical for next-generation retrieval schemes (Monsiváis-Huertero et al., 2019; Mavrovic et al., 2018).

Advanced parameterisation approaches that integrate improved initialisation within the tau–omega MEM, along with multiple scattering, vertical heterogeneity, and radiative inertia, are highlighted as key to improving retrieval accuracy and robustness (Chen and Tan, 2024; Wang et al., 2024a; Gao et al., 2020). Including dynamic vegetation parameters further enhances ecosystem representation (Monsiváis-Huertero, 2019). Moreover, recent advances in machine learning (ML) (Section 4.1.3)—particularly deep neural networks trained on combined radiometric, in situ, and assimilated datasets—show promise in capturing nonlinear relationships and mitigating scale mismatches, thereby improving SM retrieval performance and inversion stability in complex forest environments (Lee et al., 2024; Ayres et al., 2024).

4.2. Forest SM retrieval results

SMOS, SMAP, and much of the community initially focused on low-vegetation areas with VWC less than 5 kg/m^2, excluding most forests. After SMOS launched, strong Radio Frequency Interference (RFI) and irregular angular TB trends complicated the SM retrieval, including some forested areas (e.g., Oliva et al., 2012). SMAP incorporated RFI filtering capabilities in its instrument design to reduce the impact, but some areas are still affected (Piepmeier et al., 2014; Mohammed et al., 2016). Although the RFI problem is a serious one, we will not address it further here, as it is not specifically related to forests. In any case, the remedies that are urgently needed to fix this problem will also benefit the forest retrievals. Issues also arose from uncertainties in the forward operator, especially for mixed pixels and surface temperature characterisation. A lack of test sites and insufficient in situ measurement density hindered full SMOS pixel characterisation. SMAP also faced challenges with accurately characterising forest L-VOD, which is crucial for SM retrieval. Despite these difficulties, important advances were achieved, refining algorithms and improving retrieval results.

4.2.1. Global and regional investigations with measurement networks and models

A number of systematic global investigations on SMOS and SMAP SM retrievals have been carried out using various networks considered forests only marginally (Rodríguez-Fernández et al., 2017; Al-Yaari et al., 2019; Ma et al., 2019; Dong et al., 2020; Bai et al., 2022; Chaubell et al., 2022; Colliander et al., 2022, 2023); here we review studies that did focus on forested areas.

4.2.1.1. Results with traditional retrieval algorithms. The SMOS L2 SM retrievals over forested areas were initially tested against Soil Climate Analysis Network (SCAN) in the US, focusing on pixels with 70 % - 100 % forest fraction. Rahmoune et al. (2014) and Vittucci et al. (2016) reported a wide range of Pearson correlation coefficient (R) and root mean square difference (RMSD) values, with poor results in some pixels, especially in northern US forests. These early tests faced challenges, including short comparison period, algorithm (V620) limitations, particularly for mixed pixels, and inadequate spatial representativeness of in situ measurements, with a single measurement site available for most pixels that were not located inside forests. Significant improvements came with the V700 algorithm (Kerr et al., 2021), with further evaluation ongoing. In subtropical African woodlands, SM trends from SMOS L2 (V650) showed seasonal correspondence with the rainfall data from the climate research unit dataset (Vittucci et al., 2019a).

The SMOS-IC SM retrieval quality, including forested areas, was investigated by Fernandez-Moran et al. (2017), Li et al. (2020), and Wigneron et al. (2021). Fernandez-Moran et al. (2017) compared the performances of SMOS-IC (V105) and SMOS L3 (V300) with the ECMWF model SM (Albergel et al., 2012) for 2010–2015 and found that SMOS-IC performed better than SMOS L3 globally, except in parts of northern Europe and Asia. Li et al. (2020) compared two options of SMOS-IC version 105: one using the basic algorithm using the tau-omega MEM (Section 4.1.1.2) and the other using the 2S-MEM (Section 3.2.2) as a forward model. Comparisons involved SM from ECMWF and sparse SM networks distributed through the International Soil Moisture Network (ISMN) for 2011–2017. The retrievals achieved with the 2S-MEM exhibited some local improvements in unbiased RSMD (ubRMSD) but worsened the mean difference (MD), though the differences were minimal. Wigneron et al. (2021) compared SMOS-IC V2 with V105, using ERA-5 Land modelled SM (Hersbach et al., 2020) and the data from ISMN, finding V2 performed better in nearly all comparisons.

Since SMOS-IC V2 performed best in the comparisons, looking into its performance over forests is relevant for this review paper. Wigneron et al. (2021) reported median R and the average statistical metrics after comparing SMOS-IC with ERA-5 Land and ISMN (Tables 4 and 5 in Wigneron et al., 2021). Forest classes showed appreciably lower R with ERA-5 Land than the non-forest classes, with median R values of 0.37 for evergreen needleleaf and 0.34 for evergreen broadleaf forests, compared to the global average of 0.66. Forest ubRMSD ranged 0.06–0.07 m^3/m^3, and dry bias exceeded 0.12 m^3/m^3. Differences between forest and non-forest sites were reduced when using the data from ISMN, with median R values higher than 0.6 and metrics similar to those of non-forest sites. Increasing L-VOD or LAI did not significantly degrade retrieval performance (Fig. 2 and Supplemental Fig. S7 of Wigneron et al. (2021)). Furthermore, ERA-5 Land includes tropical and boreal forests, while ISMN does not include data for these areas (see Fig. 1 of Li et al., 2020), potentially impacting the relative performances.

Recent investigations into the ability of SMAP's SM products to retrieve SM under forests, led by Ayres et al. (2021), compared SMAP retrievals with National Ecological Observatory Network (NEON) measurements across the US. The study used the SMAP L2 enhanced radiometer-based SM product for 19 forest and 21 non-forest sites. Over the forested sites, the SCA-V algorithm yielded an average ubRMSD of 0.06 m^3/m^3, R of 0.42, and MD of 0.050 m^3/m^3. Performance varied widely and worsened with increasing forest growth metrics, such as height, AGB, and normalised difference infrared index (NDII). Poorer results occurred in northern US forests. SCA-H and DCA performed similarly (though SCA-H showed an MD of −0.005 m^3/m^3), underlying the sensitivity of the retrievals to the algorithm parameterisation. Non-forested sites performed better, as expected, and results were comparable to previous sparse network validation studies (e.g., Colliander et al., 2022).

Gorrab et al. (2025) compared L-band SM retrievals from both SMAP (L3/V5) and SMOS (L3/V330) over 16 boreal forested in situ monitoring sites located within North America. The results compared TB, soil reflectivity, and SM. Mixed results were found in sites with a seasonal drying trend. Higher correlation values (> -0.5) were found between SMAP and SMOS TB and the in situ SM measurements. However, in soils with limited seasonality due to consistency and relatively high SM, very low correlations were found. In comparison, the individual site correlations between in situ measurements and TB and soil reflectivity were higher (negative correlations) than those for the L3 SM products. Correlations between the L3 and in situ SM rarely exceeded 0.5 at any of the study sites for either the SMAP or SMOS soil products.

A recent investigation based on comparisons with ERA5 climatology covered tropical latitudes (Ma et al., 2023). The study considered four SMAP algorithms (SCA-V, DCA, MTDCA and SMAP-IB) and one SMOS

algorithm (SMOS-IC). In areas covered by rainforests, significant time lags between the SM from all the considered L-band algorithms and the SM from ERA5 were found, with maximum correlation coefficients in a 0.5–0.7 range for all algorithms. In forest sites of the Fluxnet network, significant correlation coefficients with ERA5 climatology were obtained (mean values in a 0.66–0.75 range). Wang et al. (2024b) compared multiple products as well, finding that the L-band SMAP and SMOS products performed better than C/X-band AMSR2 and FY-3 SM products in forest regions; all products were influenced by surface heterogeneity in vegetation coverage, land cover, and terrain.

Another recent study enhanced SMAP spatial resolution to finer scales, showing correlation improved from 0.46 to 0.55 over boreal forests, with RMSE reduced from 0.103 to 0.092 m^3/m^3, while retaining the temporal and large-scale spatial variability of the original SMAP product (Jääskeläinen et al., 2025).

4.2.1.2. Results with machine learning methods. Advancements in ML improved the spatial resolution and accuracy of satellite-derived SM products. Specifically, Random Forest (RF) models have been widely implemented for downscaling satellite SM. For example, Wen et al. (2021) found that RF downscaled SMAP and SMOS data, achieving a lower RMSE of 0.0255 m^3/m^3 compared to 0.0317 m^3/m^3 for SMOS, with better point and watershed-scale correlation and improved spatial detail in the Alpine Mountains scenario. Similarly, Ning et al. (2023) used an RF algorithm to achieve high-resolution 30-m SM mapping with a high Kling-Gupta Efficiency (KGE) of 0.69 and a low RMSE of 0.063 m^3/m^3, demonstrating the algorithm's potential over other ML methods like Extra-Trees, Gradient Boosting Regression Trees (GBRT), and XGBoost for field-scale drought monitoring. Beyond RF, deep learning models like Long Short-Term Memory (LSTM) have also proven effective in different observation scenarios, including forests. Hybrid ML approaches have also been successful, as Shangguan et al. (2023) combined multiple ML techniques in their MATCH method to downscale SM to 1 km, yielding an ubRMSE of 0.047 m^3/m^3, which was lower than SMAP's 0.056 m^3/m^3, accurately reflecting both temporal variations and spatial patterns.

Ma et al. (2024) demonstrated the success of fusing SMAP and ASCAT data globally using an RF model, achieving an R of ~0.756 and a low ubRMSE of ~ 0.042 m^3/m^3. This integrated approach proved superior to single-sensor ML estimates, significantly improving the temporal resolution by over 60 % in most areas, with RF outperforming Long Short-Term Memory, SVM, and CNN in fusion accuracy. For downscaling, Nadeem et al. (2023) successfully downscaled SMAP from 9 km to 1 km with gap-filling using an RF-based method combined with Terra data. This method achieved an R ~ 0.54 and an ubRMSE as low as 0.034 m^3/m^3 for the best combination, also noting that RF was superior to Artificial Neural Networks for this task, though accuracy was affected by vegetation attenuation, with lower correlation observed in woodland areas.

4.2.2. Tests over specific sites

SM retrieved by SMOS L2 V620 (two pixels) and SMOS-IC (one pixel) were compared to ground measurements in Kang et al. (2019) for 2014–2015. The pixels, located in the Malaysian peninsula under oil palm cover, showed that SMOS L2 and SMOS-IC underestimated SM in ascending and descending passes, with an ubRMSD over 0.06 m^3/m^3. After optimising soil roughness and vegetation parameters using local information, the statistical metrics improved substantially.

Abdelkader et al. (2022) compared SMAP L2 enhanced SM to in situ SM observations from a dense network in Millbrook, New York, between 2019 and 2021. The network comprised 25 stations across a 33-km SMAP pixel with a 70 % broadleaf deciduous forest cover and a maximum LAI of 4–5. Excluding December to February, the ubRMSD ranged from 0.03 m^3/m^3 in September to 0.06 m^3/m^3 in March, with a wet bias and MD over 0.08 m^3/m^3 in all months, exceeding 0.15 m^3/m^3 from July to November. The retrieval error was attributed mainly to the uncertainty in the effective temperature used by the SMAP algorithm.

Measurements from the Millbrook and Massachusetts sites in 2019 were used to test L-band TB sensitivity to SM in Colliander et al. (2020). Both sites, covered mainly by broadleaf deciduous forests, had dense measuring networks. SM was retrieved using the SMAP TB, and ground data provided soil and vegetation temperatures. After fitting model parameters using detailed ground measurements, good statistical metrics were achieved (ubRMSD of 0.042–0.052 m^3/m^3, R of 0.75–0.85, and low MD). The fitted vegetation optical depth was much lower, and the fitted roughness parameter was higher than the SMAP algorithm values.

The performance of the SMAP retrieval algorithm was tested over a northern Boreal site by Ambadan et al. (2022), near Candle Lake, Saskatchewan, part of the Boreal Ecosystem Research and Monitoring Sites (BERMS) in Canada. The study, conducted from June to September in 2018 and 2019, used 17 SM stations within a single SMAP 33-km pixel. The standard SMAP product significantly overestimated SM compared to in situ measurements, with a retrieved SM range of 0.2–0.45 m^3/m^3 versus a measured SM range of 0.07–0.16 m^3/m^3. It was found that by increasing VOD and the roughness parameter the results improved, suggesting an issue with the product parameter values when applied to boreal forest.

Andreadis et al. (2022) tested the performance of the SMAP algorithm over seven New Zealand sites covered by commercial "Pinus radiate" forests, aged 5 to 20 years, with forest fractions of 35 % to 64 %. Three SMAP SM products at 33 km, 3 km, and 1 km resolutions were evaluated, with the latter two combining SMAP and Sentinel-1 data. The number of in situ sensors per site ranged from 1 (four sites) to 23. The study covered the 2017–2020 period, but data availability varied by site and product. The enhanced SMAP L2 product had a mean ubRMSD of 0.08 m^3/m^3 and an R of 0.58, while the 3- and 1-km products had ubRMSD of 0.03 m^3/m^3 and 0.04 m^3/m^3, and R of 0.75 and 0.66, respectively. Results must be interpreted with caution, because they varied widely by site, and the higher-resolution products had limited samples.

The performances of SMOS and SMAP algorithms were tested in the Biosphere Reserve of Calakmul (BRC), Mexico's largest tropical forest area with 20–40 m tall trees from January to June 2015 (Monsiváis-Huertero et al., 2019). SMOS algorithms (L2, L3, and IC) significantly underestimated measured SM, with high ubRMSD. SMAP, at 33 km and 9 km resolutions, provided SM values closer to measurements but showed a large difference between morning and afternoon overpasses (over 0.2 m^3/m^3), not seen in ground data. After optimising model parameters, the retrieval results improved. The authors noted significant differences between on-site vegetation temperatures and those used in the algorithms.

4.3. Forest L-VOD retrieval results

Experimental and theoretical studies have shown that forest emissivity at L-band increases with forest biomass more smoothly than at higher frequencies (Lang et al., 2000; Macelloni et al., 2001), with branches being the main contributors (Ferrazzoli and Guerriero, 1996). Spaceborne radiometric data and retrieval algorithms have confirmed these properties globally, highlighting L-VOD's sensitivity to forest characteristics. Frappart et al. (2020) provided an exhaustive review on multifrequency VOD and its use in vegetation studies. This Section focuses on recent L-band results, testing L-VOD's potential for monitoring forest properties by estimating its spatial correlation with forest state variables such as canopy height and biomass, using Pearson correlation coefficient R for comparisons.

4.3.1. Tests against reference data sets

Early studies using SMOS L2 L-VOD (V620) demonstrated its sensitivity to forest structural properties. Rahmoune et al. (2014) showed a

clear, monotonic increase of L-VOD with canopy height across all major forest types, with minimal seasonal variability. Vittucci et al. (2016) extended this analysis to South America, reporting strong correlations with forest height ($R = 0.83$) and airborne lidar biomass ($R = 0.86$) using data from the Carnegie Airborne Observatory. Chaparro et al. (2019) confirmed L-VOD's superior performance in capturing biomass variations compared to higher-frequency VODs and optical indices using SMAP MTDCA retrievals and generalized additive models.

Several studies compared SMOS and SMAP L-VOD products to vegetation structure and biomass datasets. Konings et al. (2017) reported strong correlations ($R = 0.91$) between MTDCA L-VOD and global canopy height, with reduced seasonal variation relative to SMOS L2. Rodriguez-Fernandez et al. (2018) benchmarked SMOS-IC (V103), L2 (V620), and L3 (V300) L-VOD products across Africa, finding that SMOS-IC achieved the highest correlations with biomass ($R = 0.85$–0.94) and canopy height ($R = 0.87$), while also exhibiting delayed saturation at high biomass levels.

Further validation of L-VOD's utility in biomass estimation came from Vittucci et al. (2019b), who used Random Forest models to integrate L-VOD (V650) with climatic drivers over tropical Africa and South America. Using only L-VOD, biomass predictions achieved $R = 0.76$–0.85, which improved to ~0.89 when combined with potential evapotranspiration. Mialon et al. (2020) found SMOS-IC L-VOD strongly correlated with biomass from Saatchi et al. (2011) (R = 0.91) and GlobBiomass ($R = 0.94$), though performance declined in high northern latitudes and for low-vegetation classes. As later shown in Schwank et al. (2021, 2024), the lower performance can be attributed to the freezing of the forest vegetation.

Wigneron et al. (2021) compared spatial and temporal patterns of SMOS-IC L-VOD (V105 and V2) with various biomass and vegetation indices. Spatial correlations remained high ($R = 0.86$–0.88), while temporal correlations with NDVI were largely limited to low-biomass areas, supporting the interpretation that L-VOD primarily reflects woody biomass, as is demonstrated by tower-based measurements presented in Guglielmetti et al. (2008). Li et al. (2021a) expanded the intercomparison across nine VOD products, reaffirming L-VOD's superior correlation with biomass and canopy height globally, particularly in tropical regions.

Recent comparisons with spaceborne lidar datasets further support L-VOD's relevance to such structural parameters as tree height and plant area index. Vittucci et al. (2021, 2023) correlated SMOS L2 L-VOD (V700) with (GEDI) (Tang and Armston, 2019) and ICESat-2 (Neuenschwander and Pitts, 2019) observations (2019–2021), finding strong agreement in tropical regions ($R > 0.88$ for canopy height and plant area index). In temperate and boreal latitudes, correlation strength declined seasonally, with boreal summer values reaching $R = 0.62$. Chaubell et al. (2022) reported similar spatial agreement ($R = 0.83$) between SMAP RDCA and SMOS L3 L-VOD, though correlations with biomass ($R = 0.53$) were lower.

4.3.2. Specific investigations

Schwank et al. (2021) provided key insights into the influence of low temperatures on L-VOD in boreal forests by using an upward-looking L-band radiometer (ELBARA II; Schwank et al., 2010b) beneath a Scots Pine forest in Sodankylä, Finland (67.3° latitude) to derive L-VOD using Mätzler's (1994) model. A decrease from 0 °C to −15 °C reduced ELBARA II L-VOD from ~0.25 to ~0.07, while synchronous SMOS measurements from February 1 to May 31 showed L-VOD decreasing from 0.35 to 0.40 (at 0 °C) to about 0.15 (at −35 °C). This was explained by the L-VOD model, originally developed in Schwank et al. (2021) and refined in Schwank et al. (2024), which expresses L-VOD as a function of vegetation temperature and other forest parameters. Schwank et al. (2021) focused on the Sodankylä area, while Schwank et al. (2024) demonstrated the temperature effects across the entire boreal forest zone.

Olivares-Cabello et al. (2022) analysed VOD sensitivity at L-, C- and X-bands across various vegetation types using a global unsupervised classification. The results confirmed L-VOD's suitability for monitoring dense canopies, while X- and C-VOD exhibited higher sensitivity to vegetation in savannahs, shrublands and grasslands.

Baur et al. (2021) conducted a theoretical study on noise effects in retrieving ω and L-VOD. They found that vegetation attenuation greatly impacts sensitivity to noise. The ω retrieval is weakly constrained in low vegetation but nearly time-invariant for dense canopies, while L-VOD becomes more susceptible to noise. These findings were confirmed through global retrievals using SMAP TB over drylands and dense forests.

Roy et al. (2020) compared L-VOD retrievals from 2 tower-based radiometers and dielectric measurements in a boreal forest site over cold and warm seasons. The results showed a good correlation between L-VOD and tree dielectric constant, confirming that tree hydraulic characteristics influence L-VOD. Similarly, Holtzman et al. (2021) showed in a temperate forest (red oak) that L-VOD exhibited a diurnal cycle similar to that of leaf and stem water potential. L-VOD was also positively correlated with both the measured dielectric constant and water potentials of the stem xylem over the growing season.

Bousquet et al. (2021) examined how seasonal inundations affect L-VOD retrieval. Using a MEM for mixed scenes including standing water, they found that the partially inundated scenes cause SM overestimation and L-VOD underestimation. While the problem is significant for grasslands, it can lead to a 10 % underestimation of L-VOD in flooded forests. Thus, retrieval algorithms should consider surface water seasonality.

4.3.3. Applications

Previously cited studies found a good correlation between all L-VOD products and forest variables from different databases, though with some differences. These results encouraged the use of SMOS L-VOD for forestry applications, some of which are summarised below. Carbon losses in African drylands from 2010 to 2016 were estimated using SMOS-IC L-VOD (Brandt et al., 2018a). Conversely, biomass increased in Southern China from 1999 to 2017, as monitored using SMOS-IC L-VOD and higher-frequency VOD from SSMI, Windsat, and AMSR-E (Brandt et al., 2018b). L-VOD retrievals helped investigate seasonal variations in ecosystem-scale plant water storage and their relationship with leaf phenology (Tian et al., 2018). For boreal and temperate forests, plant water storage variations were synchronous with leaf phenology, in tropical woodlands, storage development lagged leaf area by up to 180 days. Scholze et al. (2019) estimated the mean European carbon sink over 2010–2015 using SMOS-IC L-VOD and SM combined with other data sources. Fan et al. (2019) used SMOS-IC L-VOD signatures to quantify annual aboveground carbon (AGC) fluxes, finding the tropical net AGC budget was balanced during 2010–2017. Wigneron et al. (2020) showed that after the severe drought and extreme heat of 2015–2016, tropical AGC recovery was slow in 2017, with AGC levels by year-end still below pre-drought levels of 2014.

The reliability of using VOD from different microwave frequencies and temporal aggregation methods for estimating decadal biomass carbon dynamics was investigated by Dou et al. (2023). The magnitude of VOD diurnal variations was used to evaluate its ability to reflect decadal dry biomass carbon changes. SMOS-IC L-VOD and LPDR X-VOD (retrieved by AMSR2 and AMSR-E) were found reliable for estimating decadal carbon dynamics for about 77 % and 70 % of the global vegetated land, with caution in areas like the eastern Amazon rainforest. Vaglio et al. (2020) explored the ability of SMOS L-VOD (V650 of L2) to provide forest functional information for tropical forests in Africa and South America in 2011–2014 using the FLUXNET ecosystem functional properties (EFPs) as the reference dataset. L-VOD combined with water deficit information explained 93 % (Africa) and 87 % (South America) of the yearly variability in both flux upscaled maximum gross primary productivity and light use efficiency functional properties. Bousquet et al. (2022) examined post-fire recovery during 2012–2020, comparing

performance of several remote sensing parameters, including EVI and VOD at different frequencies (X-, C-, and L-band). C- and X-VOD were more sensitive to fire impact on low-vegetation areas (grass and shrublands) or on tree leaves, while L-VOD (SMOS L2 V720) depicted fire impact on tree trunks and branches better, making it a more reliable tool for assessing biomass fire damage. Parrens et al. (2025) showed that SMOS root zone SM anomalies provide good prefire conditions information in the Canadian Boreal Forest, while VOD provided no additional information.

5. Forest ground truth availability for satellite retrievals

Generally, the challenge of validating remotely sensed geophysical retrievals is the availability of reference measurements representing the variability of land surface conditions (e.g., Colliander, 2014). Validation requires reference measurements corresponding to the area-averaged observable at the scale corresponding to the effective footprint of the remote sensing measurement. The implementation design of the reference defines the representativeness error between the retrieval and the in situ references; the type and magnitude of the representativeness error dictate the applicability of the reference in the validation process (e.g., Cosh et al., 2004; Famiglietti et al., 2008; Montzka et al., 2021; Peng et al., 2025). For example, a single SM measurement within a SMAP or SMOS footprint has very little skill to represent the actual value of the area-averaged SM at the footprint scale, but it still has skill to predict the temporal trends of the area-averaged SM (e.g., Crow et al., 2012; 2022); multiple measurements within the footprint, on the other hand, can have the skill to also represent the actual area-averaged SM (e.g., Chen et al., 2019). In this Section, we discuss the availability of such in situ reference measurements and their applicability for validating SMAP and SMOS forest SM and L-VOD retrievals.

5.1. Soil moisture reference data

The SM reference measurements need to correspond to the L-band sensing depth, which depends on the SM and soil composition (e.g., Escorihuela et al., 2010; Zheng et al., 2019; Montzka et al., 2020). As discussed above, the characterisation of the forest SM is particularly challenging because of the complexity of the O-horizon and the typically overlaying cover layer of leaf litter, moss, or lichen (Section 1.2). The microwave emission is affected by the full layer from the surface down to a depth that can be deeper than the normally expected 5 cm for the mineral soils (Fig. 1), and not capturing the moisture conditions in the full layer may lead to misrepresenting what is expected based on L-band radiometry.

Operational in situ SM measurements are relatively scarce, especially for forested areas; the vast majority of SM in situ networks are deployed in non-forested regions (e.g., Colliander et al., 2022). In some cases, the in situ measurements are installed in landscapes dominated by forests but at locations where SM and soil conditions do not represent that of the surrounding forest, such as openings or road-side areas, because of easy access, operability (e.g., solar panel illumination), the network's measurement protocol, or some other reasons; the data availability diminishes even further when looking for the depth representation of the SM measurements inside forests.

The in-forest SM measurements can be divided into sparse and dense networks following the SMAP approach (Colliander et al., 2022): Sparse networks have one or a few measurement stations in a small area within the SMAP footprints, and dense networks have multiple stations distributed over an area corresponding to the footprint's size. Table 3 lists dense and sparse observation networks that provide surface SM data in forests. The sparse networks can be used for determining the bias-insensitive metrics (ubRMSD and R), and the dense networks can also be used for determining the bias-sensitive metrics (RMSD and MD) (Chen et al., 2019).

Field experiments supporting the use of the networks are extremely valuable as they can characterize the soil and calibrate the sensors (e.g., Cosh et al., 2005; Colliander et al., 2012; Rowlandson et al., 2013), determine the surface roughness parameters (e.g., Peischl et al., 2012b; McNairn et al., 2015), establish the spatial representativeness errors (e.g., Cosh et al., 2004; Coopersmith et al., 2016), and characterize the vegetation (e.g., Peischl et al., 2012a; Colliander et al., 2019), increasing the reliability of the validation and enabling further studies into the retrieval performance, which is particularly important for forests having still considerable uncertainties.

5.2. L-VOD reference data

As discussed earlier, L-VOD is relative to the energy transmitted through and emitted by the forest canopy at the L-band. Its primary validation challenge is the lack of local in situ references. To circumvent the problem, several studies have used various remote sensing parameters to assess the credibility of the retrieved L-VOD (Section 4.3). However, these proxies cannot serve as quantified validation references

Table 3
Soil moisture in situ networks in forests.

Dense/ Sparse	Location	Site Name(s)	No. sensors (short-term)	Climate Regime[a]	Forest Type	References
D	Austria	HOAL	37	Temperate	Crop-grass-forest mix	Blöschl et al. (2016)
S	Brazil	Caxiuana, Jaru	2	Tropical	Tropical	
D	Brazil	BIONTE	7	Tropical	Tropical	Negrón-Juárez et al. (2020)
S	Brazil	K34-Valley	2	Tropical	Tropical	
D	Canada	Alberta	30	Cold	Mixed forest	Bourgeau-Chavez et al. (2025)
D	Canada	BERMS	17(20)	Cold	Evergreen needleleaf	Berg et al. (2025)
D	Finland	Sodankylä	25	Cold	Evergreen needleleaf	Ikonen et al. (2015)
S	Malaysia	NG	2	Tropical	Tropical	
S	Panama	Panama	3	Tropical	Tropical	
S	Peru	Tampobata, Los Amigos, Panguana	3	Tropical	Tropical	
D	USA (Mass.)	Harvard Forest	(23)	Cold	Deciduous broadleaf	Colliander et al. (2025)
D	USA (New York)	Millbrook	7(25)	Cold	Deciduous broadleaf	Coopersmith et al. (2016)
D	USA (*N. Carolina*)	Coweeta	34	Subtropical	Deciduous broadleaf	Miniat et al. (2021)
S	USA	NEON	19 (47 total)	Cold to Subtropical	Evergreen needleleaf; deciduous and evergreen broadleaf	Ayres et al. (2021, 2024)

[a] Koeppen-Geiger climate classification (Peel et al., 2007).

for L-VOD. Ground-based radiometers, including upward-looking ones under the canopy, can measure L-VOD by leveraging the high contrast with downwelling sky TB at L-band (approx. 5 K). However, a single-location radiometer only captures L-VOD at that specific spot, and small-scale spatial variability (as discussed previously) can significantly influence the measurement. Measurements would need to be conducted at multiple locations to obtain a locally representative L-VOD value, and capturing L-VOD at the spatial scale of the current L-band satellites requires repeating the measurements at several sites within the tens-of-km footprint to obtain a representative L-VOD estimate (analogous to a dense SM network).

The temporal variability of L-VOD adds another layer of complexity. Studies have shown that L-VOD varies over time at daily and seasonal scales, so the measurements must be conducted simultaneously at multiple sites, requiring numerous L-band radiometers (e.g., Schwank et al., 2021, 2024; Colliander et al., 2025). While the cost of the L-band radiometer technology has reduced dramatically over the past few years (e.g., Houtz et al., 2020, 2023; Zhang et al., 2024a), the cost and complexity of carrying out such a campaign, together with other supporting measurements, pose real practical challenges, let alone replicating it globally to capture different forest types.

There are also examples utilising a single L-VOD observation point for comparisons with SMOS-based L-VOD retrievals (Kontu, 2022; Holmberg et al., 2024, 2025). While there are no studies experimentally verifying the autocorrelation of L-VOD temporal changes over large distances, considering the spatial variability of environmental factors (e.g., temperature, SM, land cover) driving vegetation changes and L-VOD, it can be hypothesized, as in Holmberg et al. (2024, 2025), that the single location can represent the temporal changes within the footprint (analogous to the SM case), especially the large freezing driven changes (Schwank et al., 2021, 2024). These changes observable during freezing and thawing cycles are also illustrated in a study by Roy et al. (2020), which utilised tower-mounted L-band radiometers at a boreal forest site to understand the L-VOD during boreal freezing and thawing cycles. In the Roy et al. (2020) study, measurements of the real dielectric permittivity of trees showed the highest correlations with the L-VOD measurements.

Global Navigation Satellite System Transmissometry (GNSS-T) is a recently introduced approach to determine the attenuation of the L-band signal by forest canopy by computing the difference of the GNSS signal measured under the canopy and above or outside of the canopy (e.g., Camps et al., 2020; Guerriero et al., 2020; Humphrey and Frankenberg, 2023; Ghosh et al., 2024; Ghosh, 2025). The method does not directly measure the radiometric L-VOD because the receiver under the canopy does not capture all transmitted coherent radiation after the scattering processes in the canopy, thereby not corresponding to the total energy transmission represented by L-VOD.

Few studies have attempted to translate proxy measurements into L-VOD using EM modelling due to its complexity, and the uncertainty of the modelled L-VOD would not likely meet the requirements of a validation reference. The state-of-the-art models discussed in Section 3 rely on vegetation physical parameters to accurately characterize EM propagation within the canopy. Whether using a statistical RTE approach or solving Maxwell's equations for ensembles, these models require detailed parameterisation of vegetation structure. Ongoing research explores the level of detail needed and whether alternative data sources—such as remote sensing measurements of water content, height, basal area, and density—could provide a basis for such simulations. Alternatively, only highly detailed, on-ground measurements of three-dimensional structures using portable terrestrial laser scanners or manual methods may offer sufficiently accurate input for these computations. Different tree hydraulic measurement methods, such as dielectric probes (Matheny et al., 2015; Mavrovic et al., 2018), dendrometers (Pappas et al., 2018), and sap flow (Granier, 1987), can also provide valuable information to link VOD with tree water status. The deployment of such instrumentation could facilitate the evaluation of satellite L-VOD; however, further investigations are needed to clarify the link between VOD and tree hydraulic.

6. Discussion and future directions

Retrieving SM under forests has proven challenging, with statistical metrics often worse than for low vegetation and poor in some cases. Better results were achieved in US forests with temperate climates and moderate density, where mixed pixels are managed well by the SMAP, SMOS-IC, and SMOS-L2 v700 algorithms, and dense in situ networks are available. Overall, the statistical metrics suggest that there is potential for SM monitoring under forests, although it is more problematic in tropical and boreal forests. In tropical forests, high canopy attenuation hinders SM retrieval, even with small calibration uncertainties, although some studies, like Kang et al. (2019) and Monsiváis-Huertero et al. (2019), reported lower L-VOD (1.2 and SM over 0.2–0.3 m^3/m^3), contrasting other investigations (Vittucci et al., 2019a; Wigneron et al., 2021; Vittucci et al., 2023). Further testing is needed, especially regarding physical temperature uncertainty and the differences between V- and H-polarisation canopy emissivity, which is assumed to be equal to 0 in most adopted MEMs. In high-latitude forests (mostly Canada and Siberia), canopy attenuation is lower than at lower latitudes, but seasonal variations in wood permittivity associated with the freeze-thaw state of sap water affect L-VOD and ω (e.g., Mavrovic et al., 2018; Gorrab et al., 2025). Surface temperature characterisation is also critical in these regions, requiring algorithm refinements and new experiments. While local optimisations of MEM parameters improve results in specific studies, they cannot replace existing algorithms but can guide their further improvement.

Retrieved L-VOD over forests showed a good spatial correlation with biomass and canopy height, with improvements with respect to higher frequency VOD products and optical products. Therefore, retrieved L-VOD is a valid tool for mapping forest biomass (or height) and monitoring slowly varying processes, such as deforestation or afforestation. For monitoring short-term or seasonal phenology-related effects, a synergic use of L-VOD and higher frequency VOD is convenient because of the frequency-dependent sensing depth. However, at temperatures below the freezing point of water, the interpretation of VOD retrieved from TB at any microwave frequency requires caution, as the freezing of sap water can markedly reduce VOD. Consequently, VOD at <0 °C should not be interpreted as physiological forest properties. The influence of water bodies within radiometric footprints is a critical issue, too.

Forests vary widely and can be classified in numerous ways, commonly by leaf type (broadleaf or needleleaf) and whether trees are deciduous or evergreen. However, for L-band radiometry, classification should focus on factors that influence emission rather than traditional forestry categories. Retrievals benefit from spatially continuous, quantified data such as tree height, stem density, canopy thickness (e.g., lidar-based), cover layer type and thickness, and O-horizon depth. Species maps can help inform parameters like dominant branch orientation, even though specific species knowledge is less critical. However, using global species maps would require categorising species by traits, a process fraught with uncertainties. More advanced MEMs and retrieval approaches can better leverage these data sources in any case, reducing artefacts introduced by traditional land cover classifications in retrievals. Studies have also shown that the scattering albedo can vary over time (both forests and non-forests, e.g., Park et al. 2024), prompting the need to model or retrieve ω. Time-dependent vegetation biases can cause interpretation issues for SM (e.g., Zwieback et al., 2018). Similarly, surface roughness parameters have the potential to vary over time, although this variation is less pronounced in forests than in cultivated agricultural lands (e.g., Walker et al., 2019). Some studies have shown the potential for retrieving them along with SM and VOD with certain assumptions (e.g., Park et al. 2024; Lee et al., 2024; Holmberg et al., 2025; Schwank et al., 2024).

A non-negligible portion of forests lies in complex terrains, such as

mountainous regions or areas with a high fraction of water bodies, where retrieval performance often degrades (e.g., Kouki and Colliander, 2025). These conditions challenge SM and VOD retrievals regardless of forest cover, implying that similar mitigation approaches may be applied in both forested and non-forested areas. Correcting for water body effects requires accurate modelling of their TB (e.g., Chaubell et al., 2019) and reliable estimates of fractional water coverage within the sensor footprint (e.g., Du et al., 2023). In mountainous regions, characteristically strong spatial variability in topography, soil type, and land cover further increases the heterogeneity of SM and VOD within coarse radiometer footprints. Consequently, few studies have attempted retrievals in such environments, though some have begun addressing these challenges (e.g., Wen et al., 2021; An et al., 2025).

Forest SM validation requires a broader network of sites, particularly those equipped to monitor surface water dynamics through the cover and organic soil layers. Sites should include multiple near-surface sensors per location and sufficient spatial replication to capture the radiometer's footprint-scale average. Sparse networks suffer from representativeness error, degrading the performance metrics (e.g., Ayres et al., 2021), which is especially problematic in forests where SM retrieval performance is inherently worse than for areas covered with low vegetation. High-fidelity reference measurements are therefore essential for accurately assessing retrieval accuracy and potential improvements, which might otherwise be obscured by background variability introduced by the representativeness error. The ideal validation site would include both SM and L-VOD reference measurements at the radiometer footprint scale, although the L-VOD validation approaches are still being developed in the community.

There are several opportunities envisioned for new and emerging technologies to assist in the validation of SM and L-VOD products. As discussed, the coarse spatial resolution of spaceborne radiometers and the substantial sub-footprint variability present major challenges for linking in situ field observations to the satellite scale. Airborne campaigns, where L-band radiometers are flown over forested regions, such as those described by Colliander et al. (2015, 2019, 2025), Berg et al. (2025), can be used to improve modelling as TB emissions can be isolated to unique features on the ground. This type of modelling has previously been completed using radiometers operated on towers (Roy et al., 2020) or on trucks (e.g. O'Neill et al., 2009); however, these studies are often limited in the spatial variability that can be captured. Emerging technologies such as UAS-mounted L-band radiometers (Houtz et al., 2020; Kim et al., 2024) may address this spatial resolution challenge, providing much higher-resolution footprints. It is also envisioned that improved characterisation of structures and permittivities of forest canopies will advance our understanding of L-VOD. As discussed, L-VOD has been statically associated with biomass estimates derived from spaceborne LIDARs such as IceSAT2 (Neuenschwander and Pitts, 2019), however new opportunities for canopy characterisation using tools such terrestrial LiDAR scanning completed during the SMAPVEX-2019-2022 field campaigns (Colliander et al., 2025; Berg et al., 2025), may offer new insights into how the canopy can be represented particularly when paired with higher resolution L-band TB data.

7. Conclusion

Over the past several decades, the development of L-band radiometry has revealed a unique and robust sensitivity to both soil moisture (SM) and vegetation optical depth (VOD), enabling the retrieval of key forest properties such as biomass and vegetation water column. This review highlights the significant progress made in L-band-based retrievals over forested regions, while also identifying key limitations that remain.

Current operational retrieval algorithms and products—such as those from SMOS and SMAP—have demonstrated meaningful capabilities, but their performance over forests is often suboptimal. This is largely due to the fact that many retrieval algorithms were originally designed and calibrated for low-vegetation or open landscapes. Forested environments, by contrast, present a more complex radiative transfer scenario due to dense canopies, heterogeneous structure, and layered organic soils.

Nevertheless, a growing body of experimental studies, including airborne campaigns and empirical analyses, has shown that L-band radiometry holds untapped potential for forest applications. These studies underscore the need for new retrieval approaches specifically designed for forested ecosystems that more accurately represent canopy structure, permittivities of vegetation constituents, litter layers, and seasonal dynamics.

A major barrier to further progress is the limited availability of high-quality validation data. The validation of L-VOD products, in particular, is hindered by a lack of ground-based observations of L-VOD and measurements designed to quantify forest canopy water content and biomass in a way that is compatible with the spatial scale and signal characteristics of satellite radiometers. Similarly, forest SM validation is constrained by sparse site networks and representativeness challenges. To overcome this, there is a critical need for expanded ground validation infrastructure, including sites equipped to monitor both SM and L-VOD with sufficient spatial replication and temporal resolution. Ideally, these sites would include multiple sensors within radiometer footprints and focus on capturing soil–vegetation interactions.

In sum, while current L-band products provide valuable information over forests, the full potential of L-band radiometry for forest applications remains only partially realised. Continued algorithm development, expanded field validation, and better integration with ancillary datasets (e.g., lidar, optical, and meteorological data) will be essential to advance the state of the science and support improved monitoring of forest hydrology, structure, and carbon dynamics.

CRediT authorship contribution statement

Andreas Colliander: Writing – review & editing, Writing – original draft, Visualization, Methodology, Investigation, Conceptualization. **Mike Schwank:** Writing – review & editing, Writing – original draft, Methodology, Investigation, Conceptualization. **Yiwen Zhou:** Writing – review & editing, Writing – original draft, Visualization, Methodology, Investigation, Conceptualization. **Mehmet Kurum:** Writing – review & editing, Writing – original draft, Methodology, Investigation, Conceptualization. **Cristina Vittucci:** Writing – review & editing, Writing – original draft, Methodology, Investigation, Conceptualization. **Leung Tsang:** Writing – review & editing, Writing – original draft, Methodology, Investigation, Conceptualization. **Alex Roy:** Writing – review & editing, Methodology. **Aaron Berg:** Writing – review & editing, Methodology.

Declaration of competing interest

The authors declare that they have no known competing financial interests or personal relationships that could have appeared to influence the work reported in this paper.

Acknowledgements

A contribution to this work was made at the Jet Propulsion Laboratory, California Institute of Technology, under a contract with the National Aeronautics and Space Administration. Funding support is acknowledged from the SMAP Science Team, Global Navigation Satellite System Research (80NSSC25K7954), and Remote Sensing Theory programs by NASA and from ESA ESTEC (4000137990/22/NL/IA). During

the preparation of this work the authors used Grammarly and ChatGPT to improve the language and readability. After using the tools, the authors reviewed and edited the content as needed and take full responsibility for the content of the publication.

Data availability

No data was used for the research described in the article.

References

Abdelkader, M., et al., 2022. Assessing the spatiotemporal variability of SMAP soil moisture accuracy in a deciduous forest region. Remote Sens. 14 (Art. no. 3329).

Al Bitar, A., et al., 2017. The global SMOS level 3 daily soil moisture and brightness temperature maps. Earth Syst. Sci. Data 9, 293–315. https://doi.org/10.5194/essd-9-293-2017.

Albergel, C., et al., 2012. Evaluation of remotely sensed and modelled soil moisture products using global ground-based in situ observations. Remote Sens. Environ. 118, 215–226.

Alemohammad, S.H., Kolassa, J., Prigent, C., Aires, F., Gentine, P., 2018. Global downscaling of remotely sensed soil moisture using neural networks. Hydrol. Earth Syst. Sci. 22 (10), 5341–5356.

Altair Feko, 2023. Altair Enc, Inc.. www.altairhyperworks.com/feko.

Al-Yaari, A., et al., 2019. Assessment and inter-comparison of recently developed/reprocessed microwave satellite soil moisture products using ISMN ground-based measurements. Remote Sens. Environ. 224, 289–303.

Ambadan, J.T., MacRae, H.C., Colliander, A., Tetlock, E., Helgason, W., Gedalof, Z., Berg, A.A., 2022. Evaluation of SMAP soil moisture retrieval accuracy over a boreal Forest region. IEEE Trans. Geosci. Remote Sens. 60 (Art. no. 44414611).

An, H., Ouyang, C., Chen, X., 2025. Real-time estimation of SMAP soil moisture in mountainous areas and its impact on rainfall-runoff simulation. J. Hydrol. 660, 133487. https://doi.org/10.1016/j.jhydrol.2025.133487.

Anderegg, W.R.L., Konings, A.G., Trugman, A.T., et al., 2018. Hydraulic diversity of forests regulates ecosystem resilience during drought. Nature 561, 538–541. https://doi.org/10.1038/s41586-018-0539-7.

Andreadis, K.M., Meason, D.F., Höck, B., Lad, P., Das, N., 2022. Evaluation of multiscale SMAP soil moisture products in forested environments. IEEE Geosci. Remote Sens. Lett. 19 (Art. no. 2505805).

Ayres, E., Colliander, A., Cosh, M.H., Roberti, J.A., Simkin, S., Genazzio, M.A., 2021. Validation of SMAP soil moisture at terrestrial National Ecological Observatory Network (NEON) sites show potential for soil moisture retrieval in forested areas. IEEE J. Select. Topics Appl. Earth Observ. Remote Sens. 14, 10903–10918. https://doi.org/10.1109/jstars.2021.3121206.

Ayres, E., Reichle, R.H., Colliander, A., Cosh, M.H., Smith, L., 2024. Validation of remotely sensed and modeled soil moisture at forested and Unforested NEON sites. IEEE J. Select. Topics Appl. Earth Observ. Remote Sens. 17, 14248–14264. https://doi.org/10.1109/jstars.2024.3430928.

Babaeian, E., Sadeghi, M., Jones, S.B., Montzka, C., Vereecken, H., Tuller, M., 2019. Ground, proximal, and satellite remote sensing of soil moisture. Rev. Geophys. 57 (2), 530–616. https://doi.org/10.1029/2018rg000618.

Bai, Y., et al., 2022. A multi-temporal and multi-angular approach for systematically retrieving soil moisture and vegetation optical depth from SMOS data. Remote Sens. Environ. 280 (Art. no. 113190).

Optical properties of films and coatings, part 11. In: Bass, M., Van Stryland, E.W., Williams, D.R., Wolfe, W.L. (Eds.), 1995. Handbook of Optics. McGraw-Hill, New York, pp. 42.9–42.14.

Batchu, V., Nearing, G., Gulshan, V., 2023. A deep learning data fusion model using sentinel-1/2, SoilGrids, SMAP, and GLDAS for soil moisture retrieval. J. Hydrometeorol. 24 (10), 1789–1823.

Baur, M.J., Jagdhuber, T., Feldman, A.F., Chaparro, D., Piles, M., Entekhabi, D., 2021. Time-variations of zeroth-order vegetation absorption and scattering at L-band. Remote Sens. Environ. 267 (Art. no. 112726).

Beck, E.H., Heim, R., Hansen, J., 2004. Plant resistance to cold stress: mechanisms and environmental signals triggering frost hardening and dehardening. J. Biosci. 29 (4), 449–459. https://doi.org/10.1007/bf02712118.

Berg, B., McClaugherty, C., 2008. Plant Litter. Springer Berlin Heidelberg. https://doi.org/10.1007/978-3-540-74923-3.

Berg, A., Wicks, K., Thomas Ambadan, J., Roy, A., Magagi, R., Helgason, W., Colliander, A., Cosh, M.H., Tetlock, E., Gorrab, A., Roy, C., Salmabadi, H., Amini, Y., Alijani, Z., MacRae, H., Muhuri, A., Wang, H., Lee, J., Xu, X., Riis, N., David, C., Creen, J., McDonald, K., Steiner, N., Misra, S., Yueh, S., 2025. Soil Moisture Active Passive Soil Moisture Validation Experiment 2022 (SMAPVEX22-Boreal) over Canadian Boreal Forest. IEEE J. Sel. Topics Appl. Earth Observ. Remote Sens. Under Review.

Bircher, S., Demontoux, F., Razafindratsima, S., Zakharova, E., Drusch, M., Wigneron, J.-P., Kerr, Y.H., 2016. L-band relative permittivity of organic soil surface layers—A new dataset of resonant cavity measurements and model evaluation. Remote Sens. 8, 1024.

Blöschl, G., Blaschke, A.P., Broer, M., Bucher, C., Carr, G., Chen, X., Eder, A., et al., 2016. The hydrological open air laboratory (HOAL) in Petzenkirchen: a hypothesis-driven observatory. Hydrol. Earth Syst. Sci. 20 (1), 227–255.

Bohrer, G., Mourad, H., Laursen, T.A., Drewry, D., Avissar, R., Poggi, D., Oren, R., Katul, G.G., 2005. Finite element tree crown hydrodynamics model (FETCH) using porous media flow within branching elements: A new representation of tree hydrodynamics. Water Resour. Res. 41, W11404. https://doi.org/10.1029/2005WR004181.

Bonan, G.B., 2008. Forests and climate change: forcings, feedbacks, and the climate benefits of forests. Science 320, 1444–1449. https://doi.org/10.1126/science.1155121.

Bourgeau-Chavez, L., Hanes, C., Billmire, M., Bosse, K., Battaglia, M., Colliander, A., 2025. Assessing SMAP for Enhanced Wildfire Danger Prediction in Boreal-Arctic Ecosystems. Under Review.

Bousquet, E., Mialon, A., Rodriguez-Fernandez, N., Prigent, C., Wagner, F.H., Kerr, Y.H., 2021. Influence of surface water variations on VOD and biomass estimates from passive microwave sensors. Remote Sens. Environ. 257 (Art. no. 112345).

Bousquet, E., Mialon, A., Rodriguez-Fernandez, N., Mermoz, S., Kerr, Y.H., 2022. Monitoring post-fire recovery of various vegetation biomes using multi-wavelength satellite remote sensing. Biogeosci 19, 3317–3336.

Brandt, M., et al., 2018b. Satellite-observed major greening and biomass increase in South China karst during recent decade. Earth's Future 6, 1017–1028. https://doi.org/10.1029/2018EF000890.

Brandt, M., et al., 2018a. Satellite passive microwaves reveal recent climate-induced carbon losses in African drylands. Nature Ecol. Evol. 2, 827–835.

Bunker, D.E., DeClerck, F., Bradford, J.C., Colwell, R.K., Perfecto, I., 2005. Species loss and aboveground carbon storage in a tropical forest. Science 310 (5750), 1029–1031. CCI AGB D4.3, 2020. http://cci.esa.int/sites/default/files/biomass_D4.3_Product_User_Guide_V1.0.pdf.

Camps, A., Alonso-Arroyo, A., Park, H., Onrubia, R., Pascual, D., Querol, J., 2020. L-band vegetation optical depth estimation using transmitted GNSS signals: application to GNSS-reflectometry and positioning. Remote Sens. 12 (15), 2352. https://doi.org/10.3390/rs12152352.

CEOS (Committee on Earth Observation Satellites), Working Group on Calibration and Validation, Land Product Validation Sub-Group (LPV), Focus Area on Aboveground Biomass Product Validation. https://lpvs.gsfc.nasa.gov/AGB/AGB_home.html, 2025.

Chan, S., R. Bindlish, R. Hunt, T. Jackson, and J. Kimball, "Ancillary Data Report for Vegetation Water Content," SMAP Project Document # D-53061, JPL, January, 2013.

Chan, S.K., et al., 2016. Assessment of the SMAP passive soil moisture product. IEEE Trans. Geosci. Remote Sens. 54 (8), 4994–5007. https://doi.org/10.1109/TGRS.2016.2561938.

Chandrasekhar, S., 1960. Radiative Transfer. Dover, New York.

Chang, W., Tan, S., Lemmetyinen, J., Tsang, L., Xu, X., Li, X., Yueh, S., 2014. Dense media radiative transfer applied to SnowScat and SnowSAR. IEEE J. Sel. Top. Appl. Earth Observ. Remote. Sens. 7 (9), 3811–3825.

Chanzy, A., Kerr, Y., Wigneron, J.-P., Calvet, J.-C., 1997. Soil moisture estimation under sparse vegetation using microwave radiometry at C-band. In: In, IGARSS'97. 1997 IEEE International Geoscience and Remote Sensing Symposium Proceedings. IEEE, pp. 1090–1092.

Chaparro, D., et al., 2019. Sensitivity of L-band vegetation optical depth to carbon stocks in tropical forests: a comparison to higher frequencies and optical indices. Remote Sens. Environ. 232, 111303.

Chaubell, J., Yueh, S.H., Peng, J., Dunbar, R.S., Chan, S.K., Chen, F., Piepmeier, J.R., Bindlish, R., Entekhabi, D., O'Neill, P.E., 2019. Improving brightness temperature measurements near coastal areas for SMAP. IEEE J. Select. Topics Appl. Earth Observ. Remote Sens. 12 (11), 4578–4588. https://doi.org/10.1109/jstars.2019.2951323.

Chaubell, J., et al., 2020. Improved SMAP dual-channel algorithm for the retrieval of soil moisture. IEEE Trans. Geosci. Remote Sens. 58, 3894–3905.

Chaubell, J., et al., 2022. Regularized Dual-Channel algorithm for the retrieval of soil moisture and vegetation optical depth from SMAP measurements. IEEE J. Sel. Topics Appl. Earth Observ. Remote Sens. 15, 102–114.

Chauhan, N., Le Vine, D., and Lang, R. 1999. Passive and active microwave remote sensing of soil moisture under a forest canopy. In Proceedings of the International Geoscience and Remote Sensing Symposium, IGARSS '99, 28 June – 2 July 1999, Hamburg, Germany. IEEE, Piscataway, N.J. pp. 1914–1916.

Chen, K., Tan, S., 2023. Efficient Multiple Scattering Solutions to Radiative Transfer Equations in Strong Forward Scattering Environments for Vegetated Land Emission and its Parameterization through the Albedo-Tau Formalism, Techrxiv.

Chen, K., Tan, S., 2024. A multiple-scattering microwave radiative transfer model for land emission with vertically heterogeneous vegetation coverage. IEEE Trans. Geosci. Remote Sens. 62, 1–14.

Chen, K. S., Tzong-Dar Wu, Leung Tsang, Qin Li, Jiancheng Shi, & Fung, A. K. (2003). Emission of rough surfaces calculated by the integral equation method with comparison to three-dimensional moment method simulations. IEEE Trans. Geosci. Remote Sens. (Vol. 41, Issue 1, pp. 90–101). doi: https://doi.org/10.1109/tgrs.2002.807587.

Chen, F., Crow, W.T., Cosh, M.H., Colliander, A., Asanuma, J., Berg, A., Bosch, D.D., Caldwell, T.G., Collins, C.H., Jensen, K.H., Martínez-Fernández, J., McNairn, H., Starks, P.J., Su, Z., Walker, J.P., 2019. Uncertainty of reference pixel soil moisture averages sampled at SMAP Core validation sites. In: Journal of Hydrometeorology, vol. 20(8). American Meteorological Society, pp. 1553–1569. https://doi.org/10.1175/jhm-d-19-0049.1.

Choudhury, B., Schmugge, T., Mo, T., 1982. A parameterization of effective soil temperature for microwave emission. J. Geophys. Res. 87, 1301–1304.

Colliander, A., 2014. In: Njoku, E.G. (Ed.), Calibration and Validation: Encyclopedia of Remote Sensing, 2014. Springer, Berlin, Germany.

Colliander, A., Chan, S., Kim, S., Das, N., Yueh, S., Cosh, M., Bindlish, R., Jackson, T., Njoku, E., 2012. Long term analysis of PALS soil moisture campaign measurements

for global soil moisture algorithm development. Remote Sens. Environ. 121, 309–322. https://doi.org/10.1016/j.rse.2012.02.002.
Colliander, A., Jackson, T., McNairn, H., Chazanoff, S., Dinardo, S., Latham, B., O'Dwyer, I., Chun, W., Yueh, S., Njoku, E., 2015. Comparison of airborne passive and active L-band system (PALS) brightness temperature measurements to SMOS observations during the SMAP validation experiment 2012 (SMAPVEX12). IEEE Geosci. Remote Sens. Lett. 12 (4), 801–805. https://doi.org/10.1109/lgrs.2014.2362889.
Colliander, A., Cosh, M.H., Misra, S., Jackson, T.J., Crow, W.T., Chan, S., Bindlish, R., Chae, C., Holifield Collins, C., Yueh, S.H., 2017. Validation and scaling of soil moisture in a semi-arid environment: SMAP validation experiment 2015 (SMAPVEX15). Remote. Sens. Environ. 196, 101–112. https://doi.org/10.1016/j.rse.2017.04.022.
Colliander, A., Njoku, E.G., Huang, H., Tsang, L., 2018. Soil moisture retrieval using full wave simulations of 3-D Maxwell equations for compensating vegetation effects. Proc. IEEE Int. Geosci. Remote Sens. Symp. 2018, 1418–1421. https://doi.org/10.1109/IGARSS.2018.8517453.
Colliander, A., Cosh, M.H., Misra, S., Jackson, T.J., Crow, W.T., Powers, J., McNairn, H., Bullock, P., Berg, A., Magagi, R., Gao, Y., Bindlish, R., Williamson, R., Ramos, I., Latham, B., O'Neill, P., Yueh, S., 2019. Comparison of high-resolution airborne soil moisture retrievals to SMAP soil moisture during the SMAP validation experiment 2016 (SMAPVEX16). Remote Sens. Environ. 227, 137–150. https://doi.org/10.1016/j.rse.2019.04.004.
Colliander, A., *et al.* (2020). SMAP detects soil moisture under temperate forest canopies. Geophysical Research Letters. vol. 47, e2020GL089697, 2020. doi: https://doi.org/10.1029/2020GL089697.
Colliander, A., *et al.* (2022). Validation of soil moisture data products from the NASA SMAP Mission. *IEEE J. Sel. Topics Appl. Earth Observ. Remote Sens.*, vol. 15, pp. 364-392, 2022.
Colliander, A., et al., 2023. Performance of SMOS soil moisture products over Core validation sites. IEEE Geosci. Remote Sens. Lett. 20, 2502805.
Colliander, A., Cosh, M.H., Bourgeau-Chavez, L., Kelly, V.R., Kraatz, S., Siqueira, P., Walker, V.A., Chen, X., Roy, A., Lakhankar, T., McDonald, K.C., Steiner, N., Kurum, M., Kim, S., Berg, A., Xu, X., Misra, S., Ogut, M., Vittucci, C., Yueh, S.H., 2025. SMAP validation experiment 2019–2022 (SMAPVEX19–22): field campaign to improve soil moisture and vegetation optical depth retrievals in temperate forests. IEEE J. Select. Topics Appl. Earth Observ. Remote Sens. 18, 10749–10771. https://doi.org/10.1109/jstars.2025.3553085.
Coopersmith, E.J., Cosh, M.H., Bell, J.E., Kelly, V., Hall, M., Palecki, M.A., Temimi, M., 2016. Deploying temporary networks for upscaling of sparse network stations. Int. J. Appl. Earth Obs. Geoinf. 52. https://doi.org/10.1016/j.jag.2016.07.013.
Cosh, N.H., Jackson, T.J., Bindlish, R., Prueger, J.H., 2004. Watershed scale temporal and spatial stability of soil moisture and its role in validating satellite estimates. Remote Sens. Environ. 92 (4), 427–435. https://doi.org/10.1016/j.rse.2004.02.016.
Cosh, M. H., Jackson, T. J., Bindlish, R., Famiglietti, J. S., & Ryu, D. (2005). Calibration of an impedance probe for estimation of surface soil water content over large regions. J. Hydrol. (Vol. 311, Issues 1–4, pp. 49–58). doi: https://doi.org/10.1016/j.jhydrol.2005.01.003.
Crow, W.T., Chen, F., Colliander, A., 2022. Benchmarking downscaled satellite-based soil moisture products using sparse, point-scale ground observations. In: Remote Sensing of Environment, vol. 283. Elsevier BV, p. 113300. https://doi.org/10.1016/j.rse.2022.113300.
Crow, W. T., Berg, A. A., Cosh, M. H., Loew, A., Mohanty, B. P., Panciera, R., de Rosnay, P., Ryu, D., & Walker, J. P. (2012). Upscaling sparse ground-based soil moisture observations for the validation of coarse-resolution satellite soil moisture products. Rev. Geophys. (Vol. 50, issue 2). American Geophysical Union (AGU). doi: https://doi.org/10.1029/2011rg000372.
de Loor, G.P. 1983. The dielectric properties of wet materials. IEEE Trans. Geosci. Remote Sens. GE-21:364–369.
de Rosnay, P., Calvet, J.-C., Kerr, Y., Wigneron, J.-P., Lemaître, F., Escorihuela, M.-J., M., S.J., Saleh, K., Barrié, J., Bouhours, G., Coret, L., Cherel, G., Dedieu, G., Durbe, R., Dine, F.N.E., Froissard, F., Hoedjes, J., Kruszewski, A., Lavenu, F., Suquia, D., & Waldteufel, P., 2006. SMOSREX: A long term field campaign experiment for soil moisture and land surface processes remote sensing. Remote Sens. Environ. 102, 377–389.
Della Vecchia, A., Ferrazzoli, P., Wigneron, J.-P., Grant, J.P., 2007. Modeling forest emissivity at L band and a comparison with multitemporal measurements. IEEE Geosci. Remote Sens. Lett. 4, 508–512.
Della Vecchia, A., et al., 2010. Modeling the multi-frequency emission of broadleaf forests and their components. IEEE Trans. Geosci. Remote Sens. 48, 260–272.
Dobson, M., Ulaby, F., Hallikainen, M., El-rayes, M., 1985. Microwave dielectric behavior of wet soil-part II: dielectric mixing models. IEEE Trans. Geosci. Remote Sens. GE-23 (Issue 1, 35–46. https://doi.org/10.1109/tgrs.1985.289498.
Dong, J., et al., 2020. Comparison of microwave remote sensing and land surface modeling for surface soil moisture climatology estimation. Remote Sens. Environ. 242, 111756.
Dou, Y., et al., 2023. Reliability of using vegetation optical depth for estimating decadal and interannual carbon dynamics. Remote Sens. Environ. 285, 113390.
Du, J., Kimball, J.S., Chan, S.K., Chaubell, M.J., Bindlish, R., Dunbar, R.S., Colliander, A., 2023. Assessment of surface fractional water impacts on SMAP soil moisture retrieval. IEEE J. Select. Topics Appl. Earth Observ. Remote Sens. 16, 4871–4881. https://doi.org/10.1109/jstars.2023.3278686.
El-rayes, M., Ulaby, F., 1987. Microwave dielectric Spectrum of vegetation-part I: experimental observations. IEEE Trans. Geosci. Remote Sens. GE-25 (Issue 5, 541–549. https://doi.org/10.1109/tgrs.1987.289832.
Entekhabi, D., Yueh, S., O'Neill, P., Kellogg, K., 2014. SMAP Handbook— Soil Moisture Active Passive: Mapping Soil Moisture and Freeze/Thaw From Space. SMAP Project, Jet Propulsion Lab, Pasadena, CA, USA.
Escorihuela, M.-J., Chanzy, A., Wigneron, J.-P., Kerr, Y.H., 2010. Effective soil moisture sampling depth of L-band radiometry: A case study. Remote Sens. Environ. 114, 995–1001.
Famiglietti, J.S., Ryu, D., Berg, A.A., Rodell, M., Jackson, T.J., 2008. Field observations of soil moisture variability across scales. Water Resour. Res. 44 (1). https://doi.org/10.1029/2006wr005804.
Fan, L., et al., 2019. Satellite observed pantropical carbon dynamics. Nat. Plants 5, 944–951.
Feldman, A.F., Akbar, R., Entekhabi, D., 2018. Characterization of higher-order scattering from vegetation with SMAP measurements. Remote Sens. Environ. 219, 324–338.
Fernandez-Moran, R., et al., 2017. SMOS-IC: an alternative SMOS soil moisture and vegetation optical depth product. Remote Sens. 9, 457.
Ferrazzoli, P., Guerriero, L., 1996. Passive microwave remote sensing of forests: a model investigation. IEEE Trans. Geosci. Remote Sens. 34, 433–443.
Ferrazzoli, P., Guerriero, L., Wigneron, J.P., 2002. Simulating L-band emission of forests in view of future satellite applications. IEEE Trans. Geosci. Remote Sens. 40, 2700–2708.
Foldy, L.L., 1945. The multiple scattering of waves. I. General theory of isotropic scattering by randomly distributed scatterers. Phys. Rev. 67, 107–119.
Food and Agriculture Organization of the United Nations (FAO), 2020. The state of theWorld's Forests 2020 – Forests, biodiversity and people, p. 214 [Online]. Available: https://www.fao.org/3/ca8642en/ca8642en.pdf.
Frappart, F., et al., 2020. Global monitoring of the vegetation dynamics from the vegetation optical depth (VOD): a review. Remote Sens. 12, 2915.
Frisch, U., "Wave propagation in random medium," in *Probabilistic Methods in Applied Mathematics*. New York: Academic Press Inc., 1968.
Fung, A.K., 1994. Microwave Scattering and Emission Models and their Applications. Artech House, Norwood, MA (ch. 3).
Furutsu, K., 1975. Multiple Scattering of Waves in a Medium of Randomly Distributed Particles and Derivation of the Transport Equation. Radi Science.
Gao, L., Sadeghi, M., Ebtehaj, A., 2020. Microwave retrievals of soil moisture and vegetation optical depth with improved resolution using a combined constrained inversion algorithm: Application for SMAP satellite. Remote. Sens. Environ. 239, 111662. https://doi.org/10.1016/j.rse.2020.111662.
Gao, Y., Colliander, A., Burgin, M.S., Walker, J.P., Dinnat, E., Chae, C., Cosh, M.H., Caldwell, T.G., Berg, A., Martinez-Fernandez, J., Seyfried, M., Starks, P.J., Bosch, D. D., McNairn, H., Su, Z., van der Velde, R., 2022. Multi-frequency radiometer-based soil moisture retrieval and algorithm parameterization using in situ sites. Remote Sensing of Environment 279, 113113. https://doi.org/10.1016/j.rse.2022.113113.
Ge, L., Hang, R., Liu, Y., Liu, Q., 2018. Comparing the performance of neural network and deep convolutional neural network in estimating soil moisture from satellite observations. Remote Sens. 10 (9), 1327.
Ghosh, A., Farhad, M.M., Boyd, D., Kurum, M., 2024. A UGV-based Forest vegetation optical depth mapping using GNSS signals. IEEE J. Select. Topics Appl. Earth Observ. Remote Sens. 17, 5093–5105. https://doi.org/10.1109/jstars.2024.3365798.
Gorrab, A., Sonnentag, O., Mialon, A., Hanes, C.C., Ortet, J., Berg, A.A., Umair, M., Roy, A., 2025. Assessment of L-band passive microwave soil moisture retrievals against in situ measurements in the north American boreal biome. IEEE J. Select. Topics Appl. Earth Observ. Remote Sens. 18, 12713–12727. https://doi.org/10.1109/jstars.2025.3569063.
Granier, A., 1987. Evaluation of transpiration in a Douglas-fir stand by means of sap flow measurements. Tree Physiol. 3, 309–320.
Grant, J.P., et al., 2008. Calibration of the L-MEB model over a coniferous and a deciduous forest. IEEE Trans. Geosci. Remote Sens. 46, 808–818.
Gu, W., Tsang, L., Colliander, A., Yueh, S., 2022. Hybrid method for full-wave simulations of forests at L-band. IEEE Access 10, 105898–105909. https://doi.org/10.1109/ACCESS.2022. 3211323.
Guerriero, L., Martin, F., Mollfulleda, A., Paloscia, S., Pierdicca, N., Santi, E., Floury, N., 2020. Ground-based remote sensing of forests exploiting GNSS signals. IEEE Trans. Geosci. Remote Sens. 58 (10), 6844–6860.
Guglielmetti, M., Schwank, M., Mätzler, C., Oberdörster, C., Vanderborght, J., Flühler, H., 2007. Measured microwave radiative transfer properties of a deciduous forest canopy. Remote Sens. Environ. 109, 523–532.
Guglielmetti, M., Schwank, M., Mätzler, C., Oberdörster, C., Vanderborght, J., Flühler, H., 2008. FOSMEX: Forest soil moisture experiments with microwave radiometry. IEEE Trans. Geosci. Remote Sens. 46, 727–735.
Hallikainen, M., Ulaby, F., Dobson, M., El-rayes, M., Wu, L., 1985. Microwave dielectric behavior of wet soil-part 1: empirical models and experimental observations. IEEE Trans. Geosci. Remote Sens. GE-23 (Issue 1, 25–34. https://doi.org/10.1109/tgrs.1985.289497.
Han, Q., Zeng, Y., Zhang, L., Wang, C., Prikaziuk, E., Niu, Z., Su, B., 2023. Global long term daily 1 km surface soil moisture dataset with physics informed machine learning. Sci. Data 10 (1), 101.
Hersbach, H., et al., 2020. The ERA5 global reanalysis. Q. J. R. Meteorol. Soc. 146, 1999–2049.
Hillel, D., 1998. Environmental Soil Physics: Fundamentals, Applications, and Environmental Considerations. Academic Press.
Holmberg, M., Lemmetyinen, J., Schwank, M., Kontu, A., Rautiainen, K., Merkouriadi, I., Tamminen, J., 2024. Retrieval of ground, snow, and forest parameters from space borne passive L band observations. A case study over Sodankylä, Finland. Remote Sens. Environ. 306, 114143. https://doi.org/10.1016/j.rse.2024.114143.

Ghosh, A., Farhad, M.M., Hoque, M.E., Boyd, D.R., Bourgeau-Chavez, L., Cosh, M.H., Colliander, A., Kurum, M., 2025. Estimating Vegetation Optical Depth With Mobile GNSS Transmissiometry in Temperate Forests During SMAPVEX22. IEEE Journal of Selected Topics in Applied Earth Observations and Remote Sensing 18, 6451–6463. https://doi.org/10.1109/jstars.2025.3541182.

Holmberg, M., J. Lemmetyinen, P. Richaume, A. Colliander, A. Kontu, J. Tamminen. (2025). Bayesian time series approach applied to retrieval of ground and vegetation variables from L-band passive microwave remote sensing Under Review.

Holmes, T., de Rosnay, P., De Jeu, R., Wigneron, R.P., Kerr, Y., Calvet, J.C., Escorihuela, M.-J., Saleh, K., Lemaitre, F., 2006. A new parameterization of the effective temperature for L band radiometry. Geophys. Res. Lett. 33.

Holtzman, N.M., Anderegg, L.D.L., Kraatz, S., Mavrovic, A., Sonnentag, O., Pappas, C., Cosh, M.H., Langlois, A., Lakhankar, T., Tesser, D., Steiner, N., Colliander, A., Roy, A., Konings, A.G., 2021. L-band vegetation optical depth as an indicator of plant water potential in a temperate deciduous forest stand. Biogeosciences 18 (2), 739–753. https://doi.org/10.5194/bg-18-739-2021.

Houtz, D., Naderpour, R., Schwank, M., 2020. Portable L-band radiometer (PoLRa): design and characterization. Remote Sens. 12, Issue 17, 2780. https://doi.org/10.3390/rs12172780.

Houtz, D., Horvath, L., & Schwank, M. (2023). Vehicle Mounted L-Band Radiometer for Remote Sensing of Turfgrass Soil Moisture. IGARSS 2023–2023 IEEE International Geoscience and Remote Sensing Symposium (pp. 4824–4827). doi: https://doi.org/10.1109/igarss52108.2023.10281943.

Huang, H., Tsang, L., Njoku, E.G., Colliander, A., Liao, T.-H., Ding, K.-H., 2017. "Propagation and scattering by a layer of randomly distributed dielectric cylinders using Monte Carlo simulations of 3D Maxwell equations with applications in microwave interactions with vegetation", IEEE. Access 5 (1).

Huang, H., Tsang, L., Colliander, A., Yueh, S.H., 2019. Propagation of waves in randomly distributed cylinders using three-dimensional vector cylindrical wave expansions in foldy-lax equations. IEEE J. Multisc. Multiphys. Comput. Tech. 4, 214–226.

Huang, F., Zhang, Y., Zhang, Y., Shangguan, W., Li, Q., Li, L., Jiang, S., 2023. Interpreting conv-LSTM for spatio-temporal soil moisture prediction in China. Agriculture 13 (5), 971.

Humphrey, V., & Frankenberg, C. (2023). Continuous ground monitoring of vegetation optical depth and water content with GPS signals. Biogeosciences (Vol. 20, Issue 9, pp. 1789–1811). doi: https://doi.org/10.5194/bg-20-1789-2023.

Ikonen, J., J. Vehvilainen, K. Rautiainen, T. Smolander, J. Lemmetyinen, S. Bircher, J. Pulliainen. (2015). The Sodankyla in-situ Soil Moisture Observation Network: An Example Application to Earth Observation Data Product Evaluation," Geoscient. Instrument. Meth. Data Syst. Disc., Vol. 5, pp. 599–629.

Ishimaru, A., 1978. Wave Propagation and Scattering in Random Media. Academic, New York, p. ch. 7/8.

Jääskeläinen, E., Luoto, M., Putkiranta, P., Aurela, M., Virtanen, T., 2025. High-resolution soil moisture mapping in northern boreal forests using SMAP data and downscaling techniques. Hydrol. Earth Syst. Sci. Discuss. 2025, 1–33.

Jackson, T.J., Schmugge, T.J., 1991. Vegetation effects on the microwave emission of soils. Remote Sens. Environ. 36, 203–212.

Jackson, T. J., Le Vine, D. M., Swift, C. T., Schmugge, T. J., & Schiebe, F. R. (1995). Large area mapping of soil moisture using the ESTAR passive microwave radiometer in Washita'92. Remote Sens. Environ. (Vol. 54, Issue 1, pp. 27–37). doi: https://doi.org/10.1016/0034-4257(95)00084-e.

Jackson, T.J., Schmugge, J., Engman, E., 1996. Remote sensing applications to hydrology: soil moisture. Hydrol. Sci. J. 41, 517–530.

Jeong, J., Tsang, L., Colliander, A., Yueh, S., 2023b. Full-wave electromagnetic simulations of forests at L-band by using fast hybrid method. Prog. Electromagn. Res. 178, 111–127.

Jeong, J., L. Tsang, W. Gu, A. Colliander and S. H. Yueh (2023a). Wave propagation in vegetation field by combining fast multiple scattering theory and numerical electromagnetics in a hybrid method. *IEEE Transactions on Antennas and Propagation*, vol. 71, no. 4, pp. 3598–3610, April 2023, doi: https://doi.org/10.1109/TAP.2023.3242418.

Kang, C.S., Kanniah, K.D., Kerr, Y.H., 2019. Calibration of SMOS soil moisture retrieval algorithm: A case of tropical site in Malaysia. IEEE Trans. Geosci. Remote Sens. 57, 3827–3839.

Karam, M.A., 1997. A physical model for microwave radiometry of vegetation. IEEE Trans. Geosci. Remote Sens. 35 (4), 1045–1058.

Karam, M.A., Fung, A., Antar, Y., 1988. Electromagnetic wave scattering from some vegetation samples. IEEE Trans. Geosci. Remote Sens. 26 (6), 799–808.

Kellner, E., Lundin, L.-C., 2001. Calibration of time domain reflectometry for water content in peat soil. Hydrol. Res. 32, 315–332.

Kerr, Y.H., Waldteufel, P., Wigneron, J.-P., Delwart, S., Cabot, F., Boutin, J., Escorihuela, M.-J., Font, J., Reul, N., Gruhier, C., Juglea, S.E., Drinkwater, M.R., Hahne, A., Martín-Neira, M., Mecklenburg, S., 2010. The SMOS Mission: New Tool for Monitoring Key Elements ofthe Global Water Cycle. Proceedings of the IEEE 98 (5), 666–687. https://doi.org/10.1109/jproc.2010.2043032.

Kerr, Y.H., et al., 2012. The SMOS soil moisture retrieval algorithm. IEEE Trans. Geosci. Remote Sens. 50, 1384–1403.

Kerr, Y.H., Al-Yaari, A., Rodriguez-Fernandez, N., Parrens, M., Molero, B., Leroux, D., Bircher, S., Mahmoodi, A., Mialon, A., Richaume, P., Delwart, S., Al Bitar, A., Pellarin, T., Bindlish, R., Jackson, T.J., Rüdiger, C., Waldteufel, P., Mecklenburg, S., Wigneron, J.-P., 2016. Overview of SMOS performance in terms of global soil moisture monitoring after six years in operation. Remote. Sens. Environ. 180, 40–63. https://doi.org/10.1016/j.rse.2016.02.042.

Kerr, Y.H., et al., 2020. SMOS level 2 processor for soil moisture algorithm theoretical basis document (ATBD). Euro. Space Agency Tech. Note N. SO-TN-ESL-SM-GS-0001, Issue 4.b.

Kerr, Y.H. et al., "Read-me-first note for the release of the SMOS Level 2 Soil Moisture data products," [Online]. 2021. Available: https://earth.esa.int/eogateway/documents/20142/37627/SMOS-Level-2-Soil-Moisture-v650-release-note.pdf.

Kim, S.-B., van Zyl, J. J., Johnson, J. T., Moghaddam, M., Tsang, L., Colliander, A., Dunbar, R. S., Jackson, T. J., Jaruwatanadilok, S., West, R., Berg, A., Caldwell, T., Cosh, M. H., Goodrich, D. C., Livingston, S., Lopez-Baeza, E., Rowlandson, T., Thibeault, M., Walker, J. P., … Yueh, S. H. (2017). Surface Soil Moisture Retrieval Using the L-Band Synthetic Aperture Radar Onboard the Soil Moisture Active–Passive Satellite and Evaluation at Core Validation Sites. IEEE Trans. Geosci. Remote Sens. (Vol. 55, Issue 4, pp. 1897–1914). doi: https://doi.org/10.1109/tgrs.2016.2631126.

Kim, K.Y., Zhu, Z., Zhang, R., Fang, B., Cosh, M.H., Russ, A.L., Dai, E., Elston, J., Stachura, M., Gasiewski, A.J., Lakshmi, V., 2024. Precision soil moisture monitoring with passive microwave L-band UAS mapping. IEEE J. Select. Topics Appl. Earth Observ. Remote Sens. 17, 7684–7694.

Kimball, J.S., Endsley, A., Jones, L.A., Kundig, T., Reichle, R., 2025. SMAP L4 global daily 9 km EASE-grid carbon net ecosystem exchange. (SPL4CMDL, version 8). [data set]. NASA National Snow and Ice Data Center Distributed Active Archive Center, Boulder, Colorado USA. https://doi.org/10.5067/U7SN8JDZL0UC. Date Accessed 07-20-2025.

Klingmüller, K., Lelieveld, J., 2021. Climate model-informed deep learning of global soil moisture distribution. Geosci. Model Dev. Discuss. 2021, 1–17.

Konings, A.G., Piles, M., Rötzer, K., McColl, K.A., Chan, S.K., Entekhabi, D., 2016. Vegetation optical depth and scattering albedo retrieval using time series of dual-polarized L-band radiometer observations. Remote Sens. Environ. 172, 178–189.

Konings, A.G., Piles, M., Das, N., Entekhabi, D., 2017. L-band vegetation optical depth and effective scattering albedo estimation from SMAP. Remote Sens. Environ. 198, 460–470.

Konings, A.G., Holtzman, N.M., Rao, K., Xu, L., Saatchi, S.S., 2021. Interannual variations of vegetation optical depth are due to both water stress and biomass changes. Geophys. Res. Lett. 48 (16). https://doi.org/10.1029/2021gl095267.

Kontu, A., 2022. L-Band Observations of Soil and Trees in Freezing/Thawing Conditions, Final Report. Technical report, European Space Agency, November, p. 2022.

Kouki, K., Colliander, A., 2025. Characterizing precipitation and soil moisture drydowns in Finland using SMAP satellite data. Hydrol. Earth Syst. Sci. 29 (19), 4791–4810. https://doi.org/10.5194/hess-29-4791-2025.

Kumawat, D., Olyaei, M., Gao, L., Ebtehaj, A., 2022. Passive microwave retrieval of soil moisture below snowpack at L-band using SMAP observations. IEEE Trans. Geosci. Remote Sens. 60, 1–16. https://doi.org/10.1109/tgrs.2022.3216324.

Kumawat, D., Ebtehaj, A., Schwank, M., Li, X., Wigneron, J.P., 2024. Global estimates of L-band vegetation optical depth and soil permittivity of snow-covered boreal forests and permafrost landscape using SMAP satellite data. Remote Sens. Environ. 306, 114145.

Kurum, M., 2013. Quantifying scattering albedo in microwave emission of vegetated terrain. Remote Sens. Environ. 129, 66–74.

Kurum, M., Lang, R.H., O'Neill, P., Joseph, A., Jackson, T., Cosh, M., 2011. A first-order radiative transfer model for microwave radiometry of forest canopies at L-band. IEEE Trans. Geosci. Remote Sens. 49 (9), 3167–3179.

Kurum, M., O'Neill, P.E., Lang, R.H., Joseph, A.T., Cosh, M.H., Jackson, Thomas J., 2012a. Effective tree scattering and opacity at L-band. Remote Sens. Environ. 118, 1–9.

Kurum, M., O'Neill, P.E., Lang, R.H., Cosh, M.H., Joseph, A.T., Jackson, T.J., 2012b. Impact of conifer Forest litter on microwave emission at L-band. IEEE Trans. Geosci. Remote Sens. 50, 1071–1084.

Lang, R.H., 1981. Electromagnetic backscattering from a random distribution of lossy dielectric scatterers. Radio Sci. 16 (1), 15–30.

Lang, R.H., Sighu, J.S., 1983. Electromagnetic backscattering from a layer of vegetation: A discrete approach. IEEE Trans. Geosci. Remote Sens. 1, 62–71.

Lang, R.H., de Matthaeis, P., Le Vine, D.M., Bidwell, S., Haken, M., Chauhan, N., 2000. L-band radiometer measurements of conifer forests. In: Proc. 2000 IEEE International Geoscience and Remote Sensing Symposium, Honolulu, US, pp. 1930–1932.

Lax, M., 1951. Multiple scattering of waves. Rev. Mod. Phys. 23 (4), 287–310.

Leduc-Leballeur, M., Picard, G., Milaon, A., Arnaud, L., Lefebvre, E., Possenti, P., Kerr, Y. H., 2015. Modeling L-band brightness temperature at dome C in Antarctica and comparison with SMOS observations. IEEE Trans. Geosci. Remote Sens. 53, 4022–4032.

Lee, J., Im, J., Son, B., Cosio, E.G., Salinas, N., 2024. Improved SMAP soil moisture retrieval using a deep neural network-based replacement of radiative transfer and roughness model. IEEE Trans. Geosci. Remote Sens. 62, 1–19. https://doi.org/10.1109/tgrs.2024.3489974.

Lemmetyinen, J., Pulliainen, J., Rees, A., Kontu, A., Qiu, Y., Derksen, C., 2010. Multiple layer adaptation of the HUT snow emission model: comparison with experimental data. IEEE Trans. Geosci. Remote Sens. 48, 2781–2794.

Lemmetyinen, J., Schwank, M., Rautiainen, K., Kontu, A., Parkkinen, T., Mätzler, C., Wiesmann, A., Wegmüller, U., Derksen, C., Toose, P., Roy, A., Pulliainen, J., 2016. Snow density and ground permittivity retrieved from L-band radiometry: application to experimental data. Remote Sens. Environ. 180, 377–391.

Lenoble, J. (Ed.), 1985. Radiative Transfer in Scattering and Absorbing Atmospheres: Standard Computational Procedures. A. Deepak, Hampton, VA, pp. 46–48.

LeVine, D.M., Meneghini, R., Lang, R.H., Seker, S.S., 1983. Scattering from arbitrarily oriented dielectric disks in the physical optics regime. J. Opt. Soc. Am. A 73 (10), 1255–1262.

LeVine, D.M., Schneider, A., Lang, R.H., Carter, H.G., Dec. 1985. Scattering from thin dielectric disks. IEEE Trans. Antennas Propag. AP-33 (12), 1410–1413.

Le Vine, D.M., Lagerloef, G.S.E., Torrusio, S.E., 2010. Aquarius and Remote Sensing of Sea Surface Salinity from Space. Proceedings of the IEEE 98 (5), 688–703. https://doi.org/10.1109/jproc.2010.2040550.

Li, H., Parent, L.E., Karam, A., Tremblay, C., 2004. Potential of sphagnum peat for improving soil organic matter, water holding capacity, bulk density and potato yield in a sandy soil. Plant Soil 265, 355–365.

Li, D., Jin, R., Zhou, J., Kang, J., 2015. Analysis and reduction of the uncertainties in soil moisture estimation with the L-MEB model using EFAST and ensemble retrieval. IEEE Geosci. Remote Sens. Lett. 12 (6), 1337–1341. https://doi.org/10.1109/LGRS.2015.2399776.

Li, X., Al-Yaari, A., Schwank, M., Fan, L., Frappart, F., Swenson, J., Wigneron, J.P., 2020. Compared performances of SMOS-IC soil moisture and vegetation optical depth retrievals based on tau-omega and two-stream microwave emission models. Remote Sens. Environ. 236, 111502.

Li, X., et al., 2021a. Global-scale assessment and inter-comparison of recently developed/reprocessed microwave satellite vegetation optical depth products. Remote Sens. Environ. 253, 112208.

Li, Z.-L., Leng, P., Zhou, C., Chen, K.-S., Zhou, F.-C., Shang, G.-F., 2021b. Soil moisture retrieval from remote sensing measurements: current knowledge and directions for the future. Earth Sci. Rev. 218, 103673. https://doi.org/10.1016/j.earscirev.2021.103673.

Li, X., et al., 2022a. A new SMAP soil moisture and vegetation optical depth product (SMAP-IB): Algorithm, assessment and inter-comparison. Remote Sens. Environ. 271, 112921.

Li, L., Dai, Y., Shangguan, W., Wei, N., Wei, Z., Gupta, S., 2022b. Multistep forecasting of soil moisture using spatiotemporal deep encoder–decoder networks. J. Hydrometeorol. 23 (3), 337–350.

Lin, R.T., 1967a. Review of the electrical properties of wood and cellulose. For. Prod. J. 17 (7), 54–61.

Lin, R.T., 1967b. Review of the dielectric properties of wood and cellulose. For. Prod. J. 17 (7), 61–66.

Lutz, J.A., et al., 2018. Global importance of large-diameter trees. Glob. Ecol. Biogeogr. 27 (7), 849–864. https://doi.org/10.1111/geb.12747.

Lv, S., Wen, J., Zeng, Y., Tian, H., Su, Z., 2014. An improved two-layer algorithm for estimating effective soil temperature in microwave radiometry using in situ temperature and soil moisture measurements. Remote Sens. Environ. 152, 356–363. https://doi.org/10.1016/j.rse.2014.07.007.

Lv, S., Zeng, Y., Wen, J., Su, Z., 2016. A reappraisal of global soil effective temperature schemes. Remote Sens. Environ. 183, 144–153. https://doi.org/10.1016/j.rse.2016.05.012.

Ma, H., et al., 2023. An assessment of L-band surface soil moisture products from SMOS and SMAP in the tropical areas. Remote Sens. Environ. 284, 113344.

Ma, H., Zeng, J., Zhang, X., Peng, J., Li, X., Fu, P., Cosh, M.H., Letu, H., Wang, S., Chen, N., Wigneron, J.P., 2024. Surface soil moisture from combined active and passive microwave observations: integrating ASCAT and SMAP observations based on machine learning approaches. Remote Sens. Environ. 308, 114197.

Ma, H., Zeng, J., Chen, N., Zhang, X., Cosh, M.H., Wang, W., 2019. Satellite surface soil moisture from SMAP, SMOS, AMSR2 and ESA CCI: A comprehensive assessment using global ground-based observations. Remote Sens. Environ. 231, 111215.

Macelloni, G., Paloscia, S., Pampaloni, P., Ruisi, R., 2001. Airborne multifrequency L- to Ka-band radiometric measurements over forests. IEEE Trans. Geosci. Remote Sens. 39, 2507–2513.

Malhi, Y., & Phillips, O. L. (2004). Tropical forests and global atmospheric change: A synthesis. In Y. Malhi & O. L. Phillips (Eds.), Philosophical Transactions of the Royal Society of London. Series B: Biological Sciences (Vol. 359, Issue 1443, pp. 549–555). The Royal Society. doi: https://doi.org/10.1098/rstb.2003.1449.

Martinez-Vazquez, A., Camps, A., Duffo, N., Vall-Ilossera, M., Lopez-Sanchez, J., 2002. Full polarimetric emissivity of vegetation-covered soils: Vegetation structure effects. In: IGARSS 2002. International Geoscience and Remote Sensing Symposium. Inst. of Electr. and Electr. Eng, New York, pp. 3542–3544. https://doi.org/10.1109/IGARSS.2002.1027242.

Matheny, A., Bohrer, G., Garrity, S., Morin, T., Howard, C., Vogel, C., 2015. Observations of stem water storage in trees of opposing hydraulic strategies. Ecosphere 9, 6, 165.

Mätzler, C., 1994. Microwave transmissivity of a forest canopy: experiments made with a beech. Remote Sens. Environ. 48, 172–180.

Mätzler, C., 1998. Improved born approximation for scattering of radiation in a granular medium. J. Appl. Phys. 83, 6111–6117.

Mätzler, C., 2006. Thermal Microwave Radiation: Applications for Remote Sensing. IEE Electromagnetic Waves Series No, London, UK, p. 52.

Mätzler, C., 2001. Applications of SMOS over terrestrial ice and snow. Prepared for 3rd SMOS Workshop, DLR, Oberpfaffenhofen, Germany [Online]. Available: http://www.cesbio.upstlse.fr/data_all/SMOS_WS/WS3/23%20LBand-ice.pdf.

Mätzler, C., Aebischer, H., Schanda, W., 1984. Microwave dielectric properties of surface snow. IEEE J. Ocean. Eng. OE–9.

Mavrovic, A., Roy, A., Royer, A., Filali, B., Boone, F., Pappas, C., Sonnentag, O., 2018. Dielectric characterization of vegetation at L band using an open-ended coaxial probe. Geoscient. Instrument., Meth. Data Syst. 7 (3), 195–208. https://doi.org/10.5194/gi-7-195-2018.

Mavrovic, A., Pardo Lara, R., Berg, A., Demontoux, F., Royer, A., Roy, A., 2021. Soil dielectric characterization during freeze–thaw transitions using L-band coaxial and soil moisture probes. Hydrol. Earth Syst. Sci. 25 (3), 1117–1131.

Maxwell, J.C., 1865. A dynamical theory of the electromagnetic field. Philos. Trans. R. Soc. Lond. 155, 459–512.

McNairn, H., Jackson, T. J., Wiseman, G., Belair, S., Berg, A., Bullock, P., Colliander, A., Cosh, M. H., Kim, S.-B., Magagi, R., Moghaddam, M., Njoku, E. G., Adams, J. R., Homayouni, S., Ojo, E., Rowlandson, T., Shang, J., Goita, K., & Hosseini, M. (2015). The soil moisture active passive validation experiment 2012 (SMAPVEX12): prelaunch calibration and validation of the SMAP soil moisture algorithms. IEEE Trans. Geosci. Remote Sens. (Vol. 53, Issue 5, pp. 2784–2801). doi: https://doi.org/10.1109/tgrs.2014.2364913.

Meng, X., Peng, J., Hu, J., Li, J., Leng, G., Ferhatoglu, C., Li, X., García-García, A., Yang, Y., 2024. Validation and expansion of the soil moisture index for assessing soil moisture dynamics from AMSR2 brightness temperature. Remote Sens. Environ. 303, 114018. https://doi.org/10.1016/j.rse.2024.114018.

Mialon, A., et al., 2020. Evaluation of the sensitivity of SMOS L-VOD to forest above-ground biomass at global scale. Remote Sens. 12, 1450.

Miniat, C.F., Oishi, A.C., Bolstad, P.V., Jackson, C.R., Liu, N., Love, J.P., Pringle, C.M., Solomon, K.J., Wurzburger, N., 2021. The Coweeta hydrologic laboratory and the Coweeta Long-term ecological research project. In: Hydrological Processes, vol. 35, Issue 7. Wiley. https://doi.org/10.1002/hyp.14302.

Mironov, V., Dobson, M., Kaupp, V., Komarov, S., Kleshchenko, V., 2004. Generalized refractive mixing dielectric model for moist soils. IEEE Trans. Geosci. Rem. Sens 42, 773–785.

Mironov, V.L., Kosolapova, L.G., Fomin, S.V., 2009. Physically and Mineralogically based spectroscopic dielectric model for moist soils. IEEE Trans. Geosci. Remote Sens. 47 (7), 2059–2070. https://doi.org/10.1109/tgrs.2008.2011631.

Mironov, V.L., Roo, R.D.D., Savin, I.V., 2010. Temperature-dependable microwave dielectric model for an Arctic soil. IEEE Trans. Geosci. Remote Sens. 48, 2544–2556.

Mironov, V., Kerr, Y., Wigneron, J.-P., Kosolapova, L., & Demontoux, F. (2013). Temperature- and texture-dependent dielectric model for moist soils at 1.4 GHz. IEEE Geosci. Remote Sens. Lett. (Vol. 10, Issue 3, pp. 419–423). doi: https://doi.org/10.1109/lgrs.2012.2207878.

Mironov, V.L., Kosolapova, L.G., Fomin, S.V., Savin, I.V., 2019. Experimental analysis and empirical model of the complex permittivity of five organic soils at 1.4 GHz in the temperature range from −30 °C to 25 °C. IEEE Trans. Geosci. Remote Sens. 57 (6), 3778–3787. https://doi.org/10.1109/tgrs.2018.2887117.

Mo, T., Schmugge, T.J., 1987. A parameterization of the effect of surface roughness on microwave emission. IEEE Geosci. Remote Sens. GE-25, 481–486.

Mo, T., Choudhury, B., Schmugge, T., Wang, J., Jackson, T.A., 1982. Model for microwave emission from vegetation covered fields. J. Geophys. Res. 87 (C13), 11229–11238.

Mohammed, P.N., Aksoy, M., Piepmeier, J.R., Johnson, J.T., Bringer, A., 2016. SMAP L-band microwave radiometer: RFI mitigation prelaunch analysis and first year on-orbit observations. IEEE Trans. Geosci. Remote Sens. 54 (10), 6035–6047. https://doi.org/10.1109/tgrs.2016.2580459.

Monsiváis-Huertero, A., et al., 2019. Impact of temporal variations in vegetation optical depth and vegetation temperature on L-band passive soil moisture retrievals over a tropical forest using in-situ information. Int. J. Remote Sens. https://doi.org/10.1080/01431161.2019.1685715.

Montzka, C., M. Cosh, B. Bayat, A. Al Bitar, A. Berg, R. Bindlish, H. R. Bogena, et al. (2020). Soil moisture product validation good practices protocol version 1.0. In: C. Montzka, M. Cosh, J. Nickeson, F. Camacho (Eds.): good practices for satellite derived land product validation (p. 123), land product validation subgroup (WGCV/CEOS), doi:https://doi.org/10.5067/doc/ceoswgcv/lpv/sm.001.

Montzka, C., Bogena, H.R., Herbst, M., Cosh, M.H., Jagdhuber, T., Vereecken, H., 2021. Estimating the number of reference sites necessary for the validation of global soil moisture products. IEEE Geosci. Remote Sens. Lett. 18 (9), 1530–1534. https://doi.org/10.1109/lgrs.2020.3005730.

Mousavi, M., Colliander, A., Miller, J., Kimball, J.S., 2022. A novel approach to map the intensity of surface melting on the Antarctica ice sheet using SMAP L-band microwave radiometry. IEEE J. Select. Topics Appl. Earth Observ. Remote Sens. 15, 1724–1743. https://doi.org/10.1109/jstars.2022.3147430.

Nadeem, A.A., Zha, Y., Shi, L., Ali, S., Wang, X., Zafar, Z., Afzal, Z., Tariq, M.A.U.R., 2023. Spatial downscaling and gap-filling of SMAP soil moisture to high resolution using MODIS surface variables and machine learning approaches over ShanDian River basin, China. Remote Sens. 15 (3), 812.

Naderpour, R., Schwank, M., Mätzler, C., Lemmetyinen, J., Steffen, K., 2017. Snow density and ground permittivity retrieved from L-band radiometry: A retrieval sensitivity analysis. IEEE J. Select. Topics Appl. Earth Observ. Remote Sens. 10, 3148–3161.

Neelam, M., Colliander, A., Mohanty, B.P., Cosh, M.H., Misra, S., Jackson, T.J., 2020. Multiscale surface roughness for improved soil moisture estimation. IEEE Trans. Geosci. Remote Sens. 58 (8), 5264–5276. https://doi.org/10.1109/tgrs.2019.2961008.

Negrón-Juárez, R., et al., 2020. Calibration, measurement, and characterization of soil moisture dynamics in a central Amazonian tropical forest. Vadose Zone J. 19 (1) (Art. no. e20070).

Nelson, R.M., 2001. Water relations of forest fuels. In: Johnson, E.A., Miyanishi, K. (Eds.), Forest Fires: Behavior and Ecological Effects. Academic Press, San Diego, Calif, pp. 79–149. https://doi.org/10.1016/B978-012386660-8/50006-4.

Neuenschwander, A., Pitts, K., 2019. The ATL08 land and vegetation product for the ICESat-2 mission. Remote Sens. Environ. 221, 247–259.

Ning, J., Yao, Y., Tang, Q., Li, Y., Fisher, J.B., Zhang, X., Jia, K., Xu, J., Shang, K., Yang, J., Yu, R., 2023. Soil moisture at 30 m from multiple satellite datasets fused by random forest. J. Hydrol. 625, 130010.

Njoku, E.G., Entekhabi, D., 1996. Passive microwave remote sensing of soil moisture. Journal of Hydrology 184 (1–2), 101–129. https://doi.org/10.1016/0022-1694(95)02970-2.

Njoku, E.G., Kong, J.-A., 1977. Theory for passive microwave remote sensing of near-surface soil moisture. J. Geophys. Res. 82 (20), 3108–3118. https://doi.org/10.1029/jb082i020p03108.

Njoku, E.G., Li, L., 1999. Retrieval of land surface parameters using passive microwave measurements at 6-18 GHz. IEEE Trans. Geosci. Remote Sens. 37 (1), 79–93. Jan. 1999. https://doi.org/10.1109/36.739125.

Oliva, R., Daganzo, E., Kerr, Y.H., Mecklenburg, S., Nieto, S., Richaume, P., Gruhier, C., 2012. SMOS radio frequency interference scenario: status and actions taken to improve the RFI environment in the 1400–1427-MHz passive band. IEEE Trans. Geosci. Remote Sens. 50 (5), 1427–1439. https://doi.org/10.1109/tgrs.2012.2182775.

Olivares-Cabello, C., Chaparro, D., Vall-llossera, M., Camps, A., López-Martínez, C., 2022. Global unsupervised assessment of multifrequency vegetation optical depth sensitivity to vegetation cover. IEEE J. Sel. Topics Appl. Earth Observ. Remote Sens. 16, 538–552.

O'neill, P., Lang, R., Kurum, M., Joseph, A., Cosh, M., Jackson, T., 2009. Microwave soil moisture retrieval under trees using a modified tau-omega model. In: 2009 IEEE International Geoscience and Remote Sensing Symposium (p. III-290-III–293). IEEE. https://doi.org/10.1109/igarss.2009.5417757.

O'Neill, P., Bindlish, R., Chan, S., Chaubell, J., Colliander, A., Njoku, E., Jackson, T., 2021. Soil Moisture Active Passive (SMAP) Algorithm Theoretical Basis Document Level 2 & 3 Soil Moisture (Passive) Data Products. Revision G. Available at https://nsidc.org/sites/default/files/l2_sm_p_atbd_rev_g_final_oct2021_0.pdf.

O'Neill, P.E., Chan, S., Njoku, E.G., Jackson, T., Bindlish, R., Chaubell, J., 2022. Near Real-Time SMAP L2 Radiometer Half-Orbit 36 km EASE-Grid Soil Moisture. (SPL2SMP_NRT, version 107). [data set]. NASA National Snow and ice data center distributed active archive center, Boulder, Colorado USA. https://doi.org/10.5067/NCTT8THPWRTL. Date Accessed 07-20-2025.

O'Neill, P.E., Chan, S., Njoku, E.G., Jackson, T., Bindlish, R., Chaubell, J., 2023a. SMAP L2 Radiometer Half-Orbit 36 km EASE-grid Soil Moisture. (SPL2SMP, version 9). [data set]. NASA National Snow and ice data center distributed active archive center, Boulder, Colorado USA. https://doi.org/10.5067/K7Y2D8QQVZ4L. Date Accessed 07-20-2025.

O'Neill, P.E., Chan, S., Njoku, E.G., Jackson, T., Bindlish, R., Chaubell, J., Colliander, A., 2023b. SMAP Enhanced L2 Radiometer Half-Orbit 9 km EASE-Grid soil moisture. (SPL2SMP_E, version 6). [data set]. NASA National Snow and ice data center distributed active archive center, Boulder, Colorado USA. https://doi.org/10.5067/BN36FXOMMC4C. Date Accessed 07-20-2025.

O'Neill, P.E., Chan, S., Njoku, E.G., Jackson, T., Bindlish, R., Chaubell, J., 2023c. SMAP L3 Radiometer Global Daily 36 Km EASE-Grid Soil Moisture. (vol. SPL3SMP, Version 9). [Data Set]. NASA National Snow and Ice Data Center Distributed Active Archive Center, Boulder, Colorado USA. https://doi.org/10.5067/4XXOGX0OOW1S ([describe subset used if applicable]. Date Accessed 07-20-2025).

O'Neill, P.E., Chan, S., Njoku, E.G., Jackson, T., Bindlish, R., Chaubell, J., Colliander, A., 2023d. SMAP Enhanced L3 Radiometer Global and Polar Grid Daily 9 Km EASE-Grid Soil Moisture. (vol. SPL3SMP_E, Version 6). [Data Set]. NASA National Snow and Ice Data Center Distributed Active Archive Center, Boulder, Colorado USA. https://doi.org/10.5067/M20OXIZHY3RJ ([describe subset used if applicable]. Date Accessed 07-20-2025).

Oren, R., et al., 1999. Soil fertility limits carbon sequestration by forest ecosystems in a CO2-enriched atmosphere. Nature 411 (6836), 469–472. https://doi.org/10.1038/35078064.

Orth, R., 2021. Global soil moisture data derived through machine learning trained with in-situ measurements. Sci. Data 8 (1), 1–14.

Owe, M., de Jeu, R., Walker, J., 2002. A methodology for surface soil moisture and vegetation optical depth retrieval using the microwave polarization difference index. IEEE Trans. Geosci. Remote Sens. 39 (8), 1643–1654.

Pappas, C., Matheny, A.M., Baltzer, J.L., Barr, A.G., Black, T.A., Bohrer, G., Detto, M., Maillet, J., Roy, A., Sonnentag, O., Stephens, J., 2018. Boreal tree hydrodynamics: asynchronous, diverging, yet complementary. Tree Physiol. 38 (7), 953–964. https://doi.org/10.1093/treephys/tpy043.

Park, C.-H., Montzka, C., Jagdhuber, T., Jonard, F., De Lannoy, G., Hong, J., Jackson, T. J., Wulfmeyer, V., 2019. A dielectric mixing model accounting for soil organic matter. Vadose Zone J. 18, 190036. https://doi.org/10.2136/vzj2019.04.0036.

Park, C.-H., Jagdhuber, T., Colliander, A., Berg, A., Cosh, M.H., Lee, J., Boo, K.-O., 2024. Retrieving forest soil moisture from SMAP observations considering a microwave polarization difference index (MPDI) to -ω model. Science of Remote Sensing 9, 100131. https://doi.org/10.1016/j.srs.2024.100131.

Parrens, M., et al., 2017. Estimation of the L-Band Effective Scattering Albedo of Tropical Forests Using SMOS Observations. *IEEE Geosci.Remote Sens. Lett.* 14, 1223–1227.

Parrens, M., Cernoch, N., Baud-Fraile, E., Mialon, A., Beaudoin, A., Hanes, C., Boucher, J., Boulanger, Y., Saint-Amant, R., Roy, A., 2025. Evaluation of SMOS data to provide Prefire conditions' information for Forest fire danger rating system in Canada. IEEE Geosci. Remote Sens. Lett. 22, 1–5. https://doi.org/10.1109/lgrs.2025.3570184.

Paul, K.I., Polglase, P.J., Smethurst, P.J., O'Connell, A.M., Carlyle, C.J., Khanna, P.K., 2004. Soil temperature under forests: a simple model for predicting soil temperature under a range of forest types. Agric. For. Meteorol. 121 (3–4), 167–182.

Peake, W., 1959. Interaction of electromagnetic waves with some natural surfaces. IRE Trans. Anten. Propag. 7 (5), 324–329.

Peel, M.C., Finlayson, B.L., McMahon, T.A., 2007. Updated world map of the Koeppen-Geiger climate classification. Hydrol. Earth Syst. Sci. 11, 1633–1644. https://doi.org/10.5194/hess-11-1633-2007.

Peischl, S., Walker, J.P., Rüdiger, C., Ye, N., Kerr, Y.H., Kim, E., Bandara, R., Allahmoradi, M., 2012a. The AACES field experiments: SMOS calibration and validation across the Murrumbidgee River catchment. Hydrol. Earth Syst. Sci. 16 (6), 1697–1708. https://doi.org/10.5194/hess-16-1697-2012.

Peischl, S., Walker, J. P., Ryu, D., Kerr, Y. H., Panciera, R., & Rudiger, C. (2012b). Wheat canopy structure and surface roughness effects on multiangle observations at L-band. IEEE Trans. Geosci. Remote Sens. (Vol. 50, Issue 5, pp. 1498–1506). doi: https://doi.org/10.1109/tgrs.2011.2174644.

Peng, C., Zeng, J., Chen, K.-S., Ma, H., Letu, H., Zhang, X., Shi, P., Bi, H., 2025. Spatial representativeness of soil moisture stations and its influential factors at a global scale. IEEE Trans. Geosci. Remote Sens. 63, 1–15. https://doi.org/10.1109/tgrs.2024.3523484.

Peterson, B., Strom, S., 1973. T matrix for electromagnetic scattering from an arbitrary number of Scatterers and representations of E(3). Phys. Rev. D 3661–3678.

Picard, G., Brucker, L., Roy, A., Dupont, F., Fily,M., Royer, A., Harlow, C., 2013. Simulation of the microwave emission of multi-layered snowpacks using the dense media radiative transfer theory: the DMRT-MLmodel. Geosci.Model Dev. 6: 1061–1078. http://dx.doi.org/https://doi.org/10.5194/gmd-6-1061-2013.

Piepmeier, J.R., Johnson, J.T., Mohammed, P.N., Bradley, D., Ruf, C., Aksoy, M., Garcia, R., Hudson, D., Miles, L., Wong, M., 2014. Radio-frequency interference mitigation for the soil moisture active passive microwave radiometer. IEEE Trans. Geosci. Remote Sens. 52 (1), 761–775. https://doi.org/10.1109/tgrs.2013.2281266.

Piepmeier, J.R., Focardi, P., Horgan, K.A., Knuble, J., Ehsan, N., Lucey, J., Brambora, C., Brown, P.R., Hoffman, P.J., French, R.T., Mikhaylov, R.L., 2017. SMAP L-band microwave radiometer: instrument design and first year on orbit. IEEE Trans. Geosci. Remote Sens. 55 (4), 1954–1966.

Powell, B., et al., 2020. Forest foods and healthy diets: quantifying the contributions. Environ. Conserv. 47 (4), 309–319. https://doi.org/10.1017/S0376892916000151.

Prince, M., Roy, A., Royer, A., Langlois, A., 2019. Timing and spatial variability of fall freezing in boreal forest and its effect on SMAP L-band radiometer measurements. Remote Sens. Environ. 231, 111230.

Rahmoune, R., Ferrazzoli, P., Kerr, Y., Richaume, P., 2013. SMOS level 2 retrieval algorithm over forests: description and generation of global maps. IEEE J. Sel. Topics in Appl. Earth Observ. Remote Sens. 6, 1430–1439.

Rahmoune, R., Ferrazzoli, P., Singh, Y., Kerr, Y., Richaume, P., Al Bitar, A., 2014. SMOS retrieval results over forests: comparisons with independent measurements. IEEE J. Sel. Topics Appl. Earth Observ. Remote Sens. 7, 3858–3866.

Rakhmatulina, E., Stephens, S., Thompson, S., 2021. Soil moisture influences on Sierra Nevada dead fuel moisture content and fire risks. In: Forest Ecology and Management, vol. 496. Elsevier BV, p. 119379. https://doi.org/10.1016/j.foreco.2021.119379.

Reichle, R.H., Liu, Q., Koster, R.D., Crow, W.T., De Lannoy, G.J., Kimball, J.S., Walker, J. P., 2019. Version 4 of the SMAP level-4 soil moisture algorithm and data product. J. Adv. Model. Earth Syst. 11 (10), 3106–3130.

Repo, T., 1992. Seasonal changes of frost hardiness in Piceaabies and Pinussylvestris in Finland. Can. J. For. Res. 22 (12), 1949–1957. https://doi.org/10.1139/x92-254.

Robinson, D.A., Campbell, C.S., Hopmans, J.W., Hornbuckle, B.K., Jones, S.B., Knight, R., Ogden, F., Selker, J., Wendroth, O., 2008. Soil moisture measurement for ecological and hydrological watershed-scale observatories: a review. Vadose Zone J. 7 (1), 358–389. https://doi.org/10.2136/vzj2007.0143.

Rodríguez-Fernández, N.J., et al., 2015. Soil moisture retrieval using neural networks: application to SMOS. IEEE Trans. Geosci. Remote Sens. 53, 5991–6007.

Rodríguez-Fernández, N.J., et al., 2017. SMOS near-real-time soil moisture product: processor overview and first validation results. Hydrol. Earth Syst. Sci. 21, 5201–5216.

Rodríguez-Fernández, N.J., et al., 2018. An evaluation of SMOS L-band vegetation optical depth (L-VOD) data sets: high sensitivity of L-VOD to above-ground biomass in Africa. Biogeosci 15, 4627–4645.

Rowlandson, T.L., Berg, A.A., Bullock, P.R., Ojo, E.R., McNairn, H., Wiseman, G., Cosh, M.H., 2013. Evaluation of several calibration procedures for a portable soil moisture sensor. J. Hydrol. 498, 335–344.

Roy, A., Toose, P., Mavrovic, A., Pappas, C., Royer, A., Derksen, C., Berg, A., Rowlandson, T., El-Amine, M., Helgason, W., Barr, A., Langlois, A., Sonnentag, O., 2020. L-band response to freeze/thaw in a boreal forest stand from ground and tower-based radiometer observations. Remote Sens. Environ. 237, 111542.

Royer, A., Roy, A., Montpetit, B., Saint-Jean-Rondeau, O., Picard, G., Brucker, L., Langlois, A., 2017. Comparison of commonly-used microwave radiative transfer models for snow remote sensing. Remote Sens. Environ. 190, 247–259.

Saatchi, S.S., et al., 2011. Benchmark map of forest carbon stocks in tropical regions across three continents. Proc. Natl. Acad. Sci. USA 108, 9899–9904.

Salazar-Neira, J.C., et al., 2023. Above-ground biomass estimation based on multi-angular l-band measurements of brightness temperatures. IEEE J. Sel. Topics in Appl. Earth Observ. Remote Sens. 16 (Art. no. 5813).

Saleh, K., Portè, A., Guyon, D., Ferrazzoli, P., Wigneron, J.-P., 2005. A geometric description of a maritime pine forest suitable for discrete microwave models. IEEE Trans. Geosci. Remote Sens. 43, 2024–2035.

Salim, M., Tan, S., De Roo, R.D., Colliander, A., Sarabandi, K., 2021. Passive and active multiple scattering of forests using radiative transfer theory with an iterative approach and cyclical corrections. IEEE Trans. Geosci. Remote Sens. 60, 1–16.

Santamarina, J.C., Klein, K.A., Fam, M.A., 2001. In Soils and Wave. John Wiley & Sons, Hoboken, NJ.

Santi, E., Paloscia, S., Pampaloni, P., Pettinato, S., 2009. Ground-based microwave investigations of forest plots in Italy. IEEE Trans. Geosci. Remote Sens. 47, 3016–3025.

Schmugge, T., O'Neill, P., Wang, J., 1986. Passive Microwave Soil Moisture Research. IEEE Transactions on Geoscience and Remote Sensing GE-24 (1), 12–22. https://doi.org/10.1109/tgrs.1986.289584.

Schmugge, T., Gloersen, P., Wilheit, T., Geiger, F., 1974. Remote sensing of soil moisture with microwave radiometers. J. Geophys. Res. 79 (2), 317–323. https://doi.org/10.1029/jb079i002p00317.

Schneeberger, K., Schwank, M., Stamm, C., Rosnay, P.d., Mätzler, C., & Flühler, H., 2004. Topsoil structure influencing soil water retrieval by microwave radiometry. Vadose Zone J. 3, 1169–1179.
Scholze, M., et al., 2019. Mean European carbon sink over 2010-2015 estimated by simultaneous assimilation of atmospheric CO2, soil moisture and vegetation optical depth. Geophys. Res. Lett. https://doi.org/10.1029/2019GL085725.
Schwank, M., Mätzler, C., 2006. Dielectric properties of soil. In: Mätzler, C., Rosenkranz, P.W., Battaglia, A., Wigneron, J.P. (Eds.), Thermal Microwave Radiation - Applications for Remote Sensing: IET Electromagnetic Waves Series 52, London, UK.
Schwank, M., Guglielmetti, M., Mätzler, C., Flühler, H., 2008. Testing a new model for the L-band radiation of moist leaf litter. IEEE Trans. Geosci. Remote Sens. 46 (7), 1982–1994. Jul.
Schwank, M., Völksch, I., Wigneron, J.-P., Kerr, Y.H., Mialon, A., Rosnay, P.D., Mätzler, C., 2010a. Comparison of two bare-soil reflectivity models and validation with L-band radiometer measurements. IEEE Trans. Geosci. Rem. Sens 48, 325–337.
Schwank, M., Wiesmann, A., Werner, C., Mätzler, C., Weber, D., Murk, A., Völksch, I., Wegmüller, U., 2010b. ELBARA II, an L-band radiometer system for soil moisture research. Sensors 10 (1), 584–612. https://doi.org/10.3390/s100100584.
Schwank, M., Rautiainen, K., Mätzler, C., Stähli, M., Lemmetyinen, J., Pulliainen, J., Vehviläinen, J., Kontu, A., Ikonen, J., Ménard, C.B., Drusch, M., Wiesmann, A., Wegmüller, U., 2014. Model for microwave emission of a snow-covered ground with focus on L band. Remote Sens. Environ. 154, 180–191.
Schwank, M., Mätzler, C., Wiesmann, A., Wegmüller, U., Pulliainen, J., Lemmetyinen, J., Rautiainen, K., Derksen, C., Toose, P., Drusch, M., 2015. Snow density and ground permittivity retrieved from L-band radiometry: A synthetic analysis. IEEE J. Select. Topics Appl. Earth Observ. Remote Sens. 8, 3833–3845.
Schwank, M., Naderpour, R., Mätzler, C., 2018. "Tau-Omega"- and two-stream emission models used for passive L-Band retrievals: application to close-range measurements over a forest. Remote Sens. 10. https://doi.org/10.3390/rs10121868. Art. no. 1868.
Schwank, M., et al., 2021. Temperature effects on L-band vegetation optical depth of a boreal forest. Remote Sens. Environ. 263 (Art. no. 112542).
Schwank, M., Zhou, Y., Mialon, A., Richaume, P., Kerr, Y., Mätzler, C., 2024. Temperature dependence of L-band vegetation optical depth over the boreal forest from 2011 to 2022. Remote Sens. Environ. 315, 114470. https://doi.org/10.1016/j.rse.2024.114470.
Seker, S.S., Schneider, A., 1988. Electromagnetic scattering from a dielectric cylinder of finite length. IEEE Trans. Antennas Propag. 36 (2), 303–307. Feb.
Senanayake, I.P., Pathira Arachchilage, K.R., Yeo, I.Y., Khaki, M., Han, S.C., Dahlhaus, P. G., 2024. Spatial downscaling of satellite-based soil moisture products using machine learning techniques: A review. Remote Sens. 16 (12), 2067.
Seppanen, J., Kainulainen, J., Heiskanen, J., Praks, J., Hallikainen, M., 2016. Measurements of Boreal Coniferous Forest Soil and Humus With an Airborne Radiometer. IEEE Journal of Selected Topics in Applied Earth Observations and Remote Sensing 9 (7), 3219–3228. https://doi.org/10.1109/jstars.2016.2532923.
Seyfried, M.S., Murdock, M.D., 2004. Measurement of Soil Water Content with a 50-MHz Soil Dielectric Sensor. Soil Sci. Soc. Am. J. 68 (2), 394–403. https://doi.org/10.2136/sssaj2004.3940.
Shangguan, Y., Min, X., Shi, Z., 2023. Inter-comparison and integration of different soil moisture downscaling methods over the Qinghai-Tibet plateau. J. Hydrol. 617, 129014.
Shellito, P.J., Small, E.E., Colliander, A., Bindlish, R., Cosh, M.H., Berg, A.A., Bosch, D.D., Caldwell, T.G., Goodrich, D.C., McNairn, H., Prueger, J.H., Starks, P.J., van der Velde, R., Walker, J.P., 2016. SMAP soil moisture drying more rapid than observed in situ following rainfall events. Geophys. Res. Lett. 43 (15), 8068–8075. https://doi.org/10.1002/2016gl069946.
Shi, J., Chen, K.S., Li, Q., Jackson, T., O'Neill, P.E., Tsang, L., 2002. A parameterized surface reflectivity model and estimation of bare-surface soil moisture with L-band radiometer. IEEE Trans. Geosci. Remote Sens. 40 (12), 2674–2686.
Sihvola, A., 1999. Electromagnetic Mixing Formulas and Applications. The Institution of Electrical Engineers, London.
Singh, A., Gaurav, K., 2024. PIML-SM: physics-informed machine learning to estimate surface soil moisture from multi-sensor satellite images by leveraging swarm intelligence. IEEE Trans. Geosci. Remote Sens. 62, 1–13. https://doi.org/10.1109/tgrs.2024.3502618.
Srivastava, P.K., Han, D., Rico-Ramirez, M.A., Al-Shrafany, D., Islam, T., 2013. Data fusion techniques for improving soil moisture deficit using SMOS satellite and WRF-NOAH land surface model. Water Resour. Manag. 27 (15), 5069–5087.
Srivastava, P.K., Petropoulos, G.P., Prasad, R., Triantakonstantis, D., 2021. Random forests with bagging and genetic algorithms coupled with least trimmed squares regression for soil moisture deficit using SMOS satellite soil moisture. ISPRS Int. J. Geo Inf. 10 (8), 507.
Suess, M., Matos, P., Gutierrez, A., Zundo, M., Martín-Neira, M., 2004. Processing of SMOS level 1C data onto a discrete global grid. IEEE Int. Geosci. Remote Sens. Symp. 3, 1914–1917. https://doi.org/10.1109/IGARSS.2004.1370716.
Tang, H., Armston, J., 2019. GEDI L2B ATBD for Footprint Canopy Cover and Vertical Profile Metrics. Goddard Space Flight Center, Greenbelt, MD, USA [Online]. Available: https://lpdaac.usgs.gov/documents/588/GEDI_FCCVPM_ATBD_v1.0.pdf.
Tian, F., et al., 2018. Coupling of ecosystem-scale plant water storage and leaf phenology observed by satellite. Nature Ecol. Evol. 2, 1428–1434.
Topp, G.C., Davis, J.L., Annan, A.P., 1980. Electromagnetic determination of soil water content: measurements in coaxial transmission lines. Water Resour. Res. 16, 574–582.
Tsang, L., Kong, J.A., 2001. Scattering of Electromagnetic Waves, Vol. vol. 3, Advanced Topics. Wiley-Interscience.
Tsang, L., Kong, J.A., Shin, R.T., 1985. Theory of Microwave Remote Sensing. Wiley, New York.
Tsang, L., Chan, C.H., Pak, K., Sangani, H., Ishimaru, A., Phu, P., 1994. Monte Carlo simulations of large-scale composite random rough-surface scattering based on the banded-matrix iterative approach. J. Opt. Soc. Am. A 11 (2), 691. https://doi.org/10.1364/josaa.11.000691.
Tsang, L., Kong, J.A., Ding, K.H., 2000. Scattering of Electromagnetic Waves, Vol. 1: Theory and Applications. Wiley Interscience (426 pages).
Tsang, L., Kong, J.A., Ding, K.H., Ao, C.O., 2001. *Scattering of Electromagnetic Waves*, vol. 2: Numerical Simulations, New York, Wiley.
Tsang, L., Liao, T.-H., Gao, R., Xu, H., Gu, W., Zhu, J., 2022. Theory of microwave remote sensing of vegetation effects, SoOp and rough soil surface backscattering. Remote Sens. 14 (15), 3640.
Ulaby, F., El-rayes, M., 1987. Microwave dielectric Spectrum of vegetation - part II: dual-dispersion model. IEEE Trans. Geosci. Remote Sens. GE-25 (5), 550–557. https://doi.org/10.1109/tgrs.1987.289833.
Ulaby, F.T., Long, D.G., 2014. Emission models and land observations. In: Microwave Radar and Radiometric Remote Sensing, Ann Arbor. The University of Michigan Press, US (ch. 12).
Ulaby, F.T., Aslam, A., Dobson, M.C., 1982. Effects of vegetation cover on the radar sensitivity to soil moisture. IEEE Trans. Geosci. Remote Sens. 476–481.
Ulaby, F.T., Moore, R.K., Fung, A.K., 1986. Microwave Remote Sensing: Active, Passive Vol III: From Theory to Applications. Artech House, Dedham, MA (ch. 13).
Vaglio, G., Laurin, C., Vittucci, G., Tramontana, P., Ferrazzoli, L. Guerriero, Papale, D., 2020. Monitoring tropical forests under a functional perspective with satellite-based vegetation optical depth. Glob. Chang. Biol. 22, 3402–3416.
Vittucci, C., et al., 2016. SMOS retrieval over forests: exploitation of optical depth and tests of soil moisture estimates. Remote Sens. Environ. 180, 115–127.
Vittucci, C., Ferrazzoli, P., Richaume, P., Kerr, Y.H., 2017. Effective scattering albedo of forests retrieved by SMOS and a three-parameter algorithm. IEEE Geosci.Remote Sens. Lett. 14, 2260–2264.
Vittucci, C., Ferrazzoli, P., Kerr, Y., Richaume, P., Vaglio Laurin, G., Guerriero, L., 2019a. Analysis of vegetation optical depth and soil moisture retrieved by SMOS over tropical forests. IEEE Geosci. Remote Sens. Lett. 16, 504–508.
Vittucci, C., Vaglio Laurin, G., Tramontana, G., Ferrazzoli, P., Guerriero, L., Papale, D., 2019b. Vegetation optical depth at L band and above ground biomass in tropical range: evaluating their relationships at continental and regional scales. Int. J. Appl. Earth Obs. Geoinf. (JAG) 77, 151–161.
Vittucci, C., Guerriero, L., Ferrazzoli, P., Richaume, P., Kerr, Y., 2021. SMOS L-VOD retrieved by level 2 algorithm and its correlation with GEDI Lidar products. IEEE J. Sel. Topics Appl. Earth Observ. Remote Sens. 14, 11870–11878.
Vittucci, C., Guerriero, L., Ferrazzoli, P., 2023. Influence of vegetation height, plant area index and forest intactness on SMOS L-VOD, for different seasons and latitude ranges. IEEE Trans. Geosci. Remote Sens. 61 (Art. no. 5301911).
Walker, V.A., Hornbuckle, B.K., Cosh, M.H., Prueger, J.H., 2019. Seasonal evaluation of SMAP soil moisture in the U.S. Corn Belt. Remote Sens. 11 (21), 2488. https://doi.org/10.3390/rs11212488.
Wang, J.R., Choudhury, B.J., 1981. Remote sensing of soil moisture content, over bare field at 1.4 GHz frequency. J. Geophys. Res. Oceans 86, 5277–5282.
Wang, J.R., Schmugge, T., 1980. An empirical model for the complex dielectric permittivity of soils as a function of water content. IEEE Trans. Geosci. Rem. Sens GE-18, 288–295.
Wang, J., Xu, D., 2021. Artificial neural network-based microwave satellite soil moisture reconstruction over the Qinghai–Tibet Plateau, China. Remote Sens. 13 (24), 5156.
Wang, X., Lü, H., Crow, W.T., Zhu, Y., Wang, Q., Su, J., Zheng, J., Gou, Q., 2021. Assessment of SMOS and SMAP soil moisture products against new estimates combining physical model, a statistical model, and in-situ observations: A case study over the Huai River basin, China. J. Hydrol. 598, 126468.
Wang, Y., Shi, L., Hu, Y., Hu, X., Song, W., Wang, L., 2023. A comprehensive study of deep learning for soil moisture prediction. Hydrol. Earth Syst. Sci. Discuss. 2023, 1–38.
Wang, J., Cho, K., Negron-Juarez, R.I., Colliander, A., Caravasi, E.C., Revilla, N.S., 2024a. A theory of maximum entropy production and its application to microwave remote sensing—simultaneous retrieval of soil moisture and vegetation water content. Earth Space Sci. 11 (3) (p.e2023EA003119).
Wang, P., Zeng, J., Chen, K.-S., Ma, H., Zhang, X., Shi, P., Peng, C., Bi, H., 2024b. Global-scale assessment of multiple recently developed/reprocessed remotely sensed soil moisture datasets. IEEE Trans. Geosci. Remote Sens. 62, 1–18. https://doi.org/10.1109/tgrs.2024.3361890.
Wegmuller, U., Matzler, C., 1999. Rough bare soil reflectivity model. IEEE Trans. Geosci. Remote Sens. 37 (3), 1391–1395. https://doi.org/10.1109/36.763303.
Wen, Y., Zhao, J., Zhu, G., Xu, R., Yang, J., 2021. Evaluation of the RF-based downscaled SMAP and SMOS products using multi-source data over an Alpine Mountains basin, Northwest China. Water 13 (20), 2875.
Wiesmann, A., Mätzler, C., 1999. Microwave emission model of layered Snowpacks. Remote Sens. Environ. 70, 307–316.
Wigneron, J.-P., Chanzy, A., Calvet, J.-C., Bruguier, N., 1995. A simple algorithm to retrieve soil moisture and vegetation biomass using passive microwave measurements over crop fields. Remote Sens. Environ. 51 (3), 331–341. https://doi.org/10.1016/0034-4257(94)00081-w.
Wigneron, J.-P., Laguerre, L., Kerr, Y., 2001. A simple parameterization of the L-band microwave emission from rough agricultural soils. IEEE Trans. Geosci. Rem. Sens 39, 1697–1707.
Wigneron, J.-P., et al., 2007. L-band microwave emission of the biosphere (L-MEB) model: description and calibration against experimental data sets over crop fields. Remote Sens. Environ. 107, 639–655.

Wigneron, J.P., Chanzy, A., Kerr, Y.H., Lawrence, H., Shi, J., Escorihuela, M.J., Mironov, V., Mialon, A., Demontoux, F., Rosnay, P.D., Saleh-Contell, K., 2011. Evaluating an improved parameterization of the soil emission in L-MEB. IEEE Trans. Geosci. Remote Sens. 49, 1177–1189.

Wigneron, J.-P., et al., 2017. Modelling the passive microwave signature from land surfaces: a review of recent results and application to the SMOS & SMAP soil moisture retrieval algorithms. Remote Sens. Environ. 192, 238–262.

Wigneron, J.-P., et al., 2020. Tropical forests did not recover from the strong 2015–2016 El Niño event. Sci. Adv. 6 (Art no. eaay4603).

Wigneron, J.-P., et al., 2021. SMOS-IC data record of soil moisture and L-VOD: historical development, applications and perspectives. Remote Sens. Environ. 254 (Art. no. 112238).

Wigneron, J.-P., Ciais, P., Li, X., Brandt, M., Canadell, J.G., Tian, F., Wang, H., Bastos, A., Fan, L., Gatica, G., Kashyap, R., Liu, X., Sitch, S., Tao, S., Xiao, X., Yang, H., Espinoza Villar, J.C., Frappart, F., Li, W., Fensholt, R., 2024. Global carbon balance of the forest: Satellite-based L-VOD results over the last decade. In: Frontiers in Remote Sensing, vol. 5. Frontiers Media SA. https://doi.org/10.3389/frsen.2024.1338618.

Wilheit, T.T., 1978. Radiative Transfer in a Plane Stratified Dielectric. IEEE Trans. Geosci. Electron. 16 (2), 138–143. https://doi.org/10.1109/tge.1978.294577.

World Meteorological Organization (WMO), et al., 2022. The GCOS Implementation Plan 2022. WMO, Geneva, Switzerland. GCOS Report, GCOS-244.

Xu, L., Yu, H., Chen, Z., Du, W., Chen, N., Huang, M., 2023. Hybrid deep learning and S2S model for improved sub-seasonal surface and root-zone soil moisture forecasting. Remote Sens. 15 (13), 3410.

Yueh, S., Dinardo, S., Chan, S., Njoku, E., Jackson, T., Bindlish, R., 2008. Passive and Active L-Band System and Observations during the 2007 CLASIC Campaign. IGARSS 2008–2008 IEEE International Geoscience and Remote Sensing Symposium, Boston, MA, USA. pp. II-241-II-244. https://doi.org/10.1109/IGARSS.2008.4778972.

Zeng, J., Chen, K.-S., Cui, C., Bai, X., 2020. A physically based soil moisture index from passive microwave brightness temperatures for soil moisture variation monitoring. IEEE Trans. Geosci. Remote Sens. 58 (4), 2782–2795. https://doi.org/10.1109/tgrs.2019.2955542.

Zhang, Y., Huang, F., Li, L., Li, Q., Zhang, Y., Shangguan, W., 2023. Real-time forecast of SMAP L3 soil moisture using spatial–temporal deep learning model with data integration. Remote Sens. 15 (2), 366.

Zhang, R., Nayak, A., Houtz, D., Watts, A., Soltanaghai, E., Alipour, M., 2024a. Evaluation of soil moisture retrievals from a portable L-band microwave radiometer. Remote Sens. 16 (23), 4596. https://doi.org/10.3390/rs16234596.

Zhang, D., Lu, L., Li, X., Zhang, J., Zhang, S., Yang, S., 2024b. Spatial downscaling of ESA CCI soil moisture data based on deep learning with an attention mechanism. Remote Sens. 16 (8), 1394.

Zhao, Q., 2013. Methodology of Modeling Multiple Scattering Effects in Microwave Remote Sensing of Vegetation. Dissertation at The George Washington University.

Zheng, X., Li, X., Jin, M., Jiang, T., Zhao, K., 2017. Characteristics of L-band transmissivity and effective scattering albedo of boreal forests: a case study in Northeast China. Remote Sens. Lett. 8 (12), 1200–1209.

Zheng, D., Li, X., Wang, X., Wang, Z., Wen, J., Van Der Velde, R., Schwank, M., Su, Z., 2019. Sampling depth of L-band radiometer measurements of soil moisture and freeze-thaw dynamics on the Tibetan plateau. Remote Sens. Environ. 226, 16–25.

Zhou, Y., Sharma, A., Kurum, M., Lang, R.H., O'Neill, P.E., Cosh, M.H., 2020. The backscattering contribution of soybean pods at L-band. Remote Sens. Environ. 248, 111977.

Zhou, Y., Schwank, M., Kurum, M., Mialon, A., 2023. Modelling scattering Albedo of trees from 1 To 37 GHZ and its application to VOD retrieval. In: IGARSS 2023–2023 IEEE International Geoscience and Remote Sensing Symposium, pp. 2735–2738.

Zhou, Y., Schwank, M., Boutin, J., Richaume, P., Mialon, A., Holmberg, M., Kaleschke, L., Zeiger, P., Leduc-Leballeur, M., Ebtehaj, A., Kumawat, D., Rodriguez-Fernandez, N., Olmedo, E., Colliander, A., Dinnat, E., Feldman, A., Kurum, M., Lemmetyinen, J., Rautiainen, K., Picard, G., Reul, N., Hendricks, S., Tian-Kunze, X., Tonboe, R., Vittucci, C., Brogioni, M., Jezek, K., Macelloni, G., Drusch, M., Johnson, J., Lang, R., Le Vine, D., Entekhabi, D., Kerr, Y., 2025. Satellite Microwave Radiometry at L-Band for Monitoring Earth's Essential Climate Variables. IEEE Geoscience and Remote Sensing Magazine. Under Review.

Zwieback, S., Colliander, A., Cosh, M.H., Martínez-Fernández, J., McNairn, H., Starks, P. J., Thibeault, M., Berg, A., 2018. Estimating time-dependent vegetation biases in the SMAP soil moisture product. Hydrology and Earth System Sciences 22 (8), 4473–4489. https://doi.org/10.5194/hess-22-4473-2018.

Zhou, Y., Schwank, M., Kurum, M., Houtz, D., Zhao, Q., Lang, R., Mialon, A., Drusch, M., 2024. A microwave emission model for layered vegetation (MEMLV): A case study for Boreal forests from L- to Ka- band. IEEE Trans. Geo. Remote Sens. (under review).